Theoretical Studies of Hydrocarbon Oxidation Catalyzed by Iridium- and Ruthenium-Oxo Complexes in the Coexistence of Water

池田, 京

Theoretical Studies of Hydrocarbon Oxidation Catalyzed by Iridium– and Ruthenium–Oxo Complexes in the Coexistence of Water

Kei Ikeda

Department of Chemistry and Biochemistry
Graduate School of Engineering
Kyushu University

2021

Table of Contents

Chapter 1

General introduction

1.1 Hydrocarbon hydroxylation in the commercial process

Hydrocarbons including methane and benzene is a major component of natural gas and crude oil. In order to utilize such hydrocarbons for industrial chemistry, their C–H bond have to be activated leading to the C–H bond cleavage, which is one of important catalytic process in modern industrial chemistry.[1] Generally, light alkanes such as methane cannot be activated easily due to the strong C–H bond with a high bond dissociation energy between C and H atoms. Therefore, this reaction must be undergone under high temperature and high pressure. In particularly, the energy of HOMO and LUMO in methane is rather low and high, respectively, indicating that the electron donation and acceptance with respect to C–H bond in methane is rarely occurred.[2] Additionally, benzene and its derivatives have a strong C–H bond with a bond dissociation energy of over 100 kcal/mol, derived from the resonance effect of aromatic ring and the instability of their radical intermediate.[3-5] As a results, it is very difficult to activate C–H bond in benzene and its derivatives under mild conditions similar to methane. From the chemical nature of C–H bond described above, development of a catalyst that can activate the C–H bond of these hydrocarbons under mild conditions have been desired.[6-8]

One of the most significant C–H bond activation for modern industrial chemistry is methane and benzene hydroxylation.[1] This is because methanol and phenol obtained from their hydroxylation are very important chemical row materials for plastic productions and fuels. Chemical process with respect to above two reactions are selected as 10 challenging that typify the present needs of industrial catalyst.[1] The industrial process of conversion of methane to methanol involves a two-step reaction process via the synthesis gas ($CO + H_2$).[9] The first step (Eq. 1–1), namely steam reforming, is the reaction of methane with water to form the carbon monoxide and dihydrogen gasses with the endothermic of 49.3 kcal/mol. In the second step (Eq. 1–2) carbon monoxide is converted to methanol after an appropriate balancing of CO and H_2, in which the excess H_2 is used to generate the steam for first step. The exothermicity of the second step is –21.7 kcal/mol. This reaction, indeed, consists of two step, i. e. water gas shift

reaction (Eq. 1–3) and the reduction carbon dioxide by H_2, (Eq. 1–4).[10] Thus, the reaction to obtain 1 eq methanol from 1 eq methane is endothermic by 24.6 kcal/mol. In particularly, the stem reforming must be undergone under high temperature and high pressure.

$$CH_4 + H_2O \rightarrow CO + 3H_2 \qquad \Delta H = 49.3 \text{ kcal/mol.} \qquad (1-1)$$

$$CO + 2H_2 \rightarrow CH_3OH \qquad \Delta H = -24.7 \text{ kcal/mol.} \qquad (1-2)$$

$$CO + H_2O \rightarrow CO_2 + H_2 \qquad \Delta H = -9.9 \text{ kcal/mol.} \qquad (1-3)$$

$$CO_2 + 3H_2 \rightarrow CH_3OH + H_2O \qquad \Delta H = -14.8 \text{ kcal/mol.} \qquad (1-4)$$

In contrast, the direct conversion of methane to methanol (Eq. 1–5) using O_2 gas is exothermic by 30.7 kcal/mol.[11,12]

$$CH_4 + 1/2O_2 \rightarrow CH_3OH \qquad \Delta H = -30.7 \text{ kcal/mol.} \qquad (1-5)$$

The direct conversion process is energetically favored than modern industrial process involving two-step reaction via synthesis gas, and therefore it is of current interest in pure and applied chemistry.

On the other hand, the conversion of benzene to phenol using O_2 gas is performed under relatively mild conditions (~ 500 K) in the high pH aqueous solution. However, industrial process of conversion of benzene to phenol, namely Cumene process,[13,14] involves multi-step as following, (1) nucleophilic attack of propylene to proton, (2) aromatic electrophilic substitution of benzene to form cumene (2-propylbenzene), (3) the formation of cumene-hydroperoxo by reacting cumene with O_2, and (4) the formation of phenol from cumene-hydroperoxo through hemiacetal (Scheme 1–1). Since acetone is produced as a by-product in this process. The market price of phenol is dependent on the marketability of acetone. Moreover, the catalytic conversion is rather low (~5 %).

Scheme 1-1. Schematic Representation of the Cumene method.

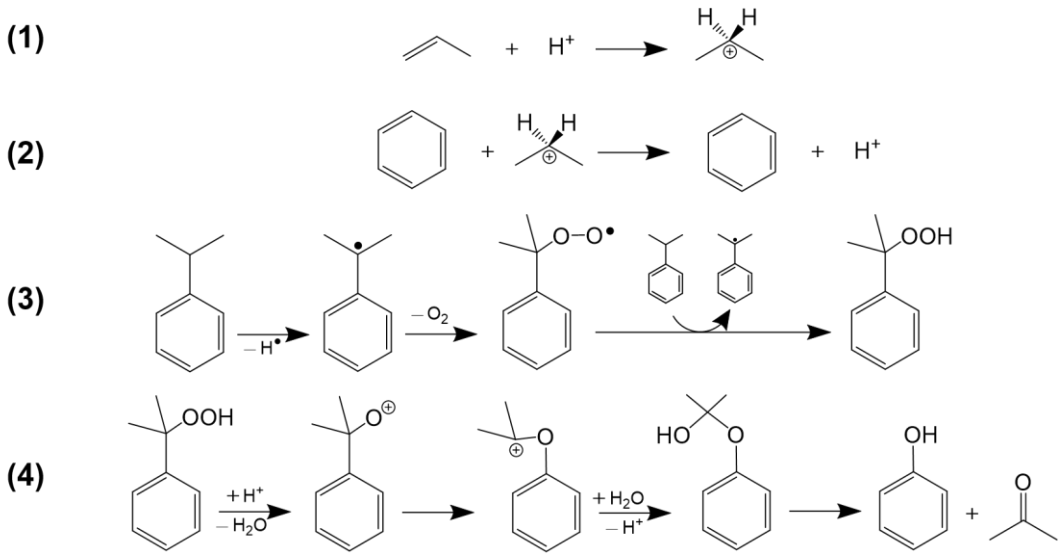

1.2 Methane and benzene hydroxylation by homogeneous catalyst

In contrast to the commercial process of methane and benzene hydroxylation performed involving multi-step and producing by-product, homogeneous catalyst involving transition metal–oxo active site have an advantage of being able to catalyze direct oxidation of methane and benzene to methanol and phenol, respectively. These catalysts have been inspired and developed from inspiring metalloenzymes catalyzing hydrocarbon such as cytochrome P450[15], soluble and particulate methane monooxygenase (sMMO[11,16,17] and pMMO[12,18]), and tyrosinase.[19,20] In the methane hydroxylation reaction there are two reaction mechanism,[2] i.e. radical and non-radical mechanism (Scheme 1-2). In the radical mechanism (A), transition metal–oxo (MO^+) abstract H atom in methane to form metal-hydroxyl (MOH^+) and methyl radicals ($^{\bullet}CH_3$). Subsequent reaction diverges depending on whether the metal center is coordinately saturated or coordinately unsaturated. In the coordinately saturated case (A-1) $^{\bullet}CH_3$ attacks to oxygen atom to form methanol complex, directly, whereas in the coordinately saturated case (A-2) $^{\bullet}CH_3$ is trapped by metal center and then C–O bond formation is occurred to form methanol complex. Both of mechanisms are wildly believed to occur in the hydroxylation of cytochrome P450[19,20] sMMO, and pMMO.[11,12,16-18] In the non-radical

mechanism (B) the C–H bond cleavage and C–O bond formation takes place concertedly, leading to the methanol complex in the one-step without radical intermediate.

Scheme 1-2. Schematic Representation of the Methane Hydroxylation Reaction via (A) Radical and (B) Non-Radical Mechanism.

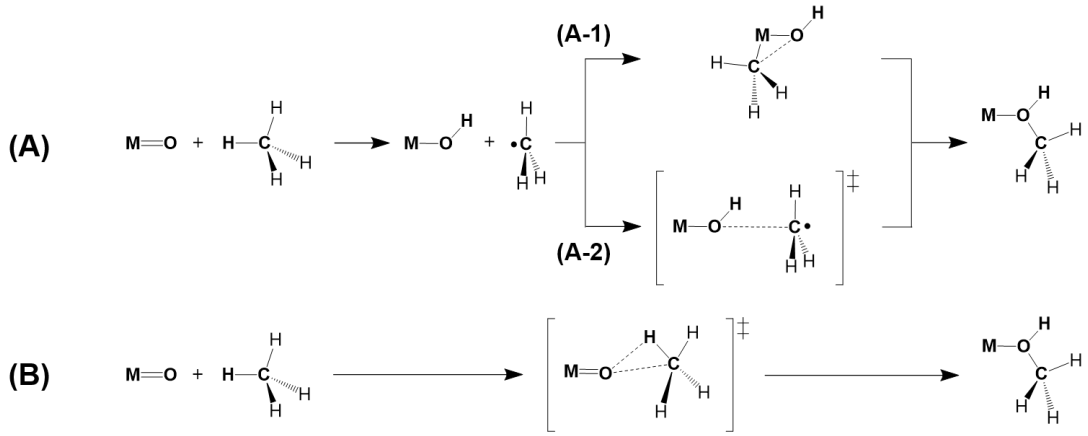

The benzene hydroxylation reaction, on the other hand, can be considered two different reaction mechanisms,[21] i. e. hydrogen abstraction mechanism and oxygen-insertion mechanism (Scheme 1-3). Similar to the methane hydroxylation reaction in the radical, the benzene hydroxylation reaction in the hydrogen abstraction mechanism (C) is initiated by the H atom abstraction by MO^+ to form MOH^+ and radical intermediate ($^{\bullet}C_6H_5$) and then phenol is formed via C–O bond formation. In contrast to hydrogen abstraction mechanism, benzene ring in the oxygen-insertion mechanism (D) is attacked by MO^+ to form arenium intermediate ($MO(H)(C_6H_5)^+$) through the aromatic nucleophilic substitution. After that, the H atom migrate to O atom to form phenol.

Scheme 1-3. Schematic Representation of the Benzene Hydroxylation Reaction via (C) Hydrogen Abstraction and (D) Oxygen-Insertion Mechanism.

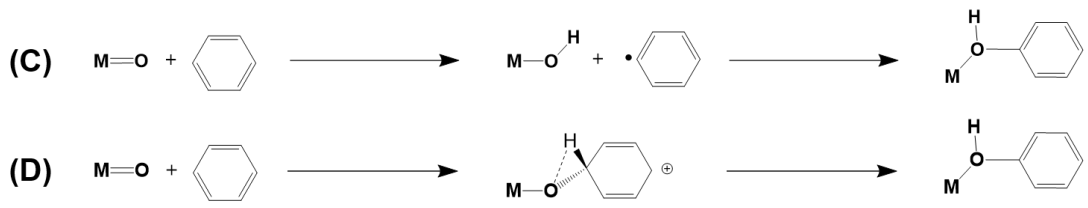

1.3 Formation of transition metal–oxo species in metalloenzyme

The metal-oxo complexes are generally produced by reacting with metal center and oxidizing agents such as H_2O_2 and 3-chlorobenzene-1-carboperoxoic acid (*m*CPBA).[22] In addition, in order to increase the concentrations of agents and substrates, the hydroxylation of methane and benzene catalyzed by these metal-oxo complex are performed in the harmful and high toxic organic solvent. In contrast to these homogeneous catalysts, metalloenzyme produce transition metal–oxo active site in aqueous solution using O_2 as an oxygen source under mild condition. As shown in Scheme 1-4, mononuclear species (M^{n+}) reacts with O_2 to form superoxo complex ($M^{(n+1)+}$–$O_2^{\bullet-}$).[19,20] Subsequent protonation and reduction leads to form metal-oxo active site ($M^{(n+2)+}$=O). Dinuclear species also becomes metal-oxo complex through the bis-μ-oxo complex. [11,12,16-18] The electron source is nicotinamide adenine dinucleotide (NADH), of which price is much expensive.

Scheme 1-4. Schematic Representation of the Formation of Transition Metal–Oxo Species in the (1)Mononuclear and (2) Dinuclear Enzyme Using an O_2 Molecule

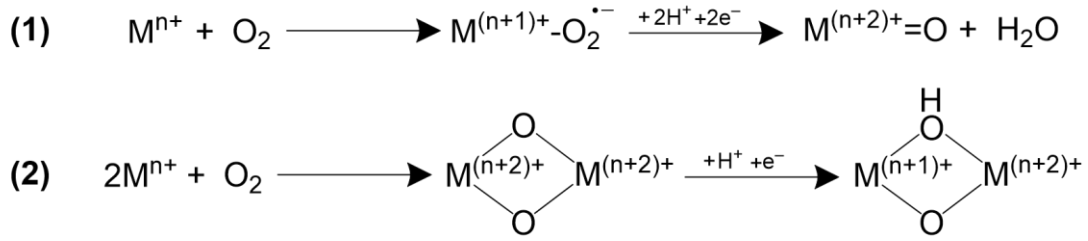

On the other hand, there are some metalloenzyme producing transition metal–oxo complex by using a H_2O molecule as an oxygen source. Mn_4CaO_5 cluster, exist in the photosystem II (PSII),[23-26] catalyze the formation of O_2 from H_2O with the deprotonation and oxidation reactions. The oxidation of this reaction is driven by the visible light irradiation for light-harvesting system, where the electrons is finally used for the synthesis of nicotinamide adenine dinucleotide phosphate (NADPH) from $NADP^+$, and the proton is released from the complex via a water-assisted proton relay. Additionally, some molybdenum-[27] and tungsten-containing[28] enzymes is known to catalyze substrates by using molybdenum- and tungsten-oxo active species, oxygen in both of which are produced from H_2O with the deprotonation and oxidation similar to the mechanism of Mn_4CaO_5 cluster (Scheme 1-5).

Scheme 1-5. Schematic Representation of the Formation of Transition-Metal-Oxo Species Using an O_2 Molecule

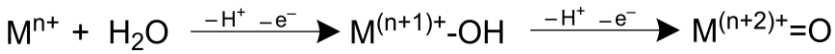

1.4 Survey of this thesis

The transition metal–oxo complex is used for the dioxygen evolution catalyst by electrochemical method and light irradiation, where the oxygen in the transition metal–oxo species is derived from a H_2O molecule. These catalysts have a great potential for the oxidation of substrate without sacrificial agent and harmful solvent. Unfortunately, the oxidation of methane and benzene by using these catalysts in the coexistence of water have rarely been performed.

In this thesis the methane and benzene hydroxylation catalysts are proposed. To investigate the electronic structure of transition metal–oxo species, perform the geometrical optimization, and calculate analytical harmonic vibration frequencies help us understand reaction mechanisms of hydroxylation of substrate. A relationship between reaction mechanism and the molecular orbitals (MO) provides important chemical information that would help understanding of reaction phenomenon and design of new catalyst. The aim of this thesis is the explanation and prediction of the catalyst catalyzing the hydroxylation of methane and benzene on the basis of chemical thinking about the reaction mechanism. Herein the authors proposed two types of catalysts; methane hydroxylation catalyst for light-driven methane fuels cell and benzene hydroxylation catalyst in aqueous solution.

At first, light-driven methane fuels cell is proposed. This is the fuel cell that convert methane into methanol driven by the visible light irradiation for anode consists of iridium–aqua complex $[Ir^{III}(\eta^5\text{-}C_5Me_5)\{bpy(COOH)_2\}(H_2O)]^{2+}$ (bpy($COOH_2$) = 2,2'-bipyridine-4,4'-dicarboxylic acid) over WO_3.This anode electrode was developed by Ogo and coworker for the light-driven fuels cell catalyzing water splitting via iridium–oxo complex $[Ir^{V}(\eta^5\text{-}C_5Me_5)\{bpy(COOH)_2\}(O)]^{2+}$. In Chapter2 (*Inorg. Chem.* **2019**, *58*, 7274–7284.), the catalytic cycle of water splitting by the iridium–aqua complex is investigated by using density functional theory (DFT) calculations. It is revealed that the water existing around the play essential roles for proton acceptor, stabilization of intermediate, and oxygen source of the iridium–oxo

complex. Also, the computational results suggested importance of the understanding on the of the formation mechanism of the iridium–oxo complex. In Chapter 3 (*Inorg. Chem.* **2020**, *59*, 415–422.), by performing DFT and time-dependent DFT calculations, the mechanism of the formation of the iridium–oxo complex from the iridium–aqua complex is revealed using the cluster model that the iridium complex is over a $(WO_3)_{40}$ cluster with the coordination of carboxylate group to W atom. The computation results prove the importance of the deprotonation from H_2O and OH ligand for the light oxidation reaction. In Chapter 4 (*ACS Catal.* **2020**, *10*, 8254–8262.), the reaction mechanism and possibility of methane hydroxylation by the iridium–oxo complex via radial and non-radial paths are discussed. Detailed investigations of geometries and MOs provide the knowledge for the design of methane hydroxylation catalyst.

Next, benzene hydroxylation catalyst in aqueous solution is proposed, in Chapter 5 (*In revision*). Ru-substituted Keggin-type polyoxometalate $[Ru^{V}(O)XW_{11}O_{39}]^{n-}$ ($3 \leq n \leq 6$) (*X* = Al, Ga, Si, Ge, P, As, and S; heteroatoms) is used for a model catalyst. Based on the different reactivity between catalyst-benzene and catalyst-water, the reaction rate ratio between benzene hydroxylation and water oxidation reactions is discussed, leading to high selective benzene hydroxylation catalyst compared to the water oxidation.

In Chapter 6, the conclusions are shown.

Reference

1. Haggin, J. Chemists Seek Greater Recognition for Catalysts. *Chem. Eng. News* **1993**, *71*, 23–27

2. Yoshizawa, K.; Miyanishi, M. Orbital Concept for Methane Activation. In *Direct Hydroxylation of Methane*; Yoshizawa, K., Ed.; Springer: Singapore, 2020; pp 1–22.

3. Weiss, J. M.; Downs, C. R. Catalytic Oxidation of Benezene to Maleic Acid. *J. Chem. Educ*. **1925**, *2*, 1178–1180.

4. Davico, G. E.; Bierbaum, V. M.; DePuy, C. H.; Ellison, G. B.; Squires, R. The C–H bond Energy of Benzene. *J. Am. Chem. Soc.* **1995**, *117*, 2590–2599.

5. He, C.; Li, J.; Cheng, J.; Li, L.; Li, P.; Hao, Z.; Xu, Z. P. Comparative Studies on Porous Material-Supported Pd Catalysts for Catalytic Oxidation of Benzene, Toluene, and Ethyl Acetate. *Ind. Eng. Chem. Res.* **2009**, *48*, 6930–6936.

6. Herrerías, C. Yao, X; Li, Z.; Li, C.-J. Reaction of C–H bonds in Water. *Chem. Rev.* **2007**, *107*. 2546–2562.

7. Gunary, A.; Theopold, K. H. C–H Bond Activation by Metal Oxo Compounds. *Chem. Rev.* **2010**, *110*, 1060–1081.

8. Balcells, D.; Clot, E.; Eisenstein, O. C–H Bond Activation in Transition Metal Species from a Computational Perspective. *Chem. Rev.* **2010**, *110*, 749–823.

9. Chilov, A. E.; Shul´pin, G. B. Activation of C – H bons by Metal Complexes. *Chem. Rev.* **1997**, *97*, 2879–2832.

10. Chinchen, G. C.; Denny, P. J.; Parker, D. G. Spencer, M. S. Whan, D. A. Mechanism of Methanol Synthesis from $CO_2/CO/H_2$ Mixtures over Copper/Zinc Oxide/Alumina Catalysts: Use of ^{14}C-Lablled Reactants. *Appl. Catal.* **1987**, *30*, 333–338.

11. Feig, A. L.; Lippard, S. J. Reactions of Non-Heme Iron(II) Centers with Dioxygen in Biology and Chemistry. *Chem. Rev.* **1994**, *94*, 759–805.

12. Lieberman, R. L., Shrestha, D. B.; Doan, P. E. Hoffman, B. M. Stemmler, T. L. Rosenzweig, A. C. Purified Particulate Methane Monooxygenase from *Methlococcus*

Capsulatus (Basth) is a Dimer with Both Mononuclear Copper and a Copper-Containing Cluster. *Proc. Natl. Aca. Sci.* U. S. A. **2003**, *100*, 3820–3825.

13. Hock, H., Lang, S. Autoxydation von Kohlenwassertoffen, IX, Mitteil.: Über Peroyde von Benzol-Derivaten. *Ber. Dtsch. Chem. Ges.* **1944**, *77*, 257–264.

14. Turton, R.; Bailie, R. C.; Whiting, W. B.; Shaelwitz, J. A. *Analysus, Synthesis and Design of Chemical Processes*, "2nd Ed.; Prentice Hall: Upper Saddle River, NJ, 2003.

15. Sono, M.; Roach, M. P.; Coulter, E. D.; Dawsin, J. H. Heme-Containing Oxygenase. *Chem. Rev.* **1996**, *96*, 2841–2888.

16. Rosenzweig, A. C.; Frederick, C. A.; Lippard, S. J.; Nordlund, P. Crystal Structure of a Bacterial Non-Heme Iron Hydroxylase That Catalyzes the Biological Oxidation of Methane. *Nature* **1993**, *366*, 537–543.

17. Bail. M.-H.; Newcomb, M.; Friesner, R. A.; Lippard, S. J. Mechanistic Studies on the Hydroxylation of Methane by Methane Monooxygenase. *Chem. Rev.* **2003**, *103*. 2385–2420.

18. Lieberman, R. L.; Rosenzweig, A. C. Crystal Structure of a Membrane-Bound Metalloenzyme That Catalyzes the Biological Oxidation of Methane. *Nature* **2005**, *434*, 177–182.

19. Solomon, E. I.; Sundaram, U. M.; Machonkin, T. E. Multicopper Oxidases and Oxygenases. *Chem. Rev.* **1996**, *96*, 2563–2606.

20. Liang, Y.; Wei, J.; Qiu, X.; Jiao, N. Homogeneous Oxygenase Catalysis *Chem. Rev.* **2018**, *118*, 4912–4945.

21. Shiota Y.; Suzuki, K.; Yoshizawa, K. Mechanism for the Direct Oxidation of Benzene to Phenol by FeO^+. *Organometallics* **2005,** *24*, 3532–3538.

22. Gunay, A.; Theopold, K. H. C–H Bond Activations by Metal Oxo Compounds. *Chrm. Rev.* **2010**, *110*, 1060–1081.

23. Umena, Y.; Kawakami, K.; Shen, J.-R.; Kamiya, N. Crystal Structure of Oxygen-Evolving Photosystem II at a Resolution of 1.9 Å. *Nature* **2011**, *473*, 55−60.

24. McEvoy, J. P.; Brudvig, G. W. Water-Splitting Chemistry of Photosystem II. *Chem. Rev.* **2006**, *106*, 4455−4483.

25. Cox, N.; Pantazis, D. A.; Neese, F.; Lubitz, W. Biological Water Oxidation. *Acc. Chem. Res.* **2013**, *46*, 1588−1596.

26. Yano, J.; Yachandra, V. Mn_4Ca Cluster in Photosynthesis: Where and How Water Is Oxidized to Dioxygen. *Chem. Rev.* **2014**, *114*, 4175−4205.

27. Hille, R. The Mononuclear Molybdenum Enzymes. *Chem. Rev.* **1996**, *96*, 2757−2816.

28. Johnson, M. K.; Rees, D. C.; Adams, M. W. W. Tungstoenzymes. *Chem. Rev.* **1996**, *96*, 2817−2840.

Chapter 2

O_2 evolution from H_2O Catalyzed by a Half-Sandwich Iridium Complex

2.1 Introduction

Renewable energies generated from small molecules such as H_2O are important for addressing the environmental and energy-related issues.[1-6] Photosystem II (PSII) enzyme consisting of Mn and Ca active centers, namely Mn_4CaO_5 cluster, converts H_2O into O_2 to obtain electrons from H_2O. This reaction corresponds to H_2O oxidation and requires the oxidation potential of 1.23 V vs SHE (standard hydrogen electrode) (Eq. 2 – 1).

$$2H_2O \rightarrow O_2 + 4H^+ + 4e^- \qquad E^o = 1.23\ V \qquad (2-1)$$

PSII catalyze the H_2O oxidation by absorbing energy as in the solar cell.[7-10] In spite of their high catalytic activity, PSII has some issues with respect to enzyme isolation, industrial applications, and catalytic deactivation. Therefore, researchers have attempted to develop alternative, better catalysts.[11-13]

It has been considered that the transition metal–oxo species is important intermediate as an active species for H_2O oxidation. Blue dimer, *cis,cis*-$[(bpy)_2(H_2O)Ru^{III}ORu^{III}(H_2O)(bpy)_2]^{4+}$ (bpy = 2,2'-bipridine), is the first example for catalytic oxidation of H_2O to form O_2 with Ce(IV) as a oxidant.[14-15] Motivated by an excellent study, many transition metal–oxo complex catalyzing H_2O oxidation have been developed.[11-13] However, these catalysts need to oxidant such as cerium ammonium nitrite (CAN) to form transition metal–oxo active species from H_2O. Additionally, it is generally difficult to increase catalytic performance of these catalyst due to the degradation and low stability and of catalysts.

On the other hand, half-sandwich iridium complexes have a great potential for catalyzing H_2O oxidation. This is because the electron-rich Cp* (pentamethyl cyclopentadienyl anion) ligand stabilize the high-valent iridium–oxo species that reacts with H_2O to form an O–O bond, which is the most important step in the O_2 evolution from H_2O.[16-21] For example, Blakemore et al. reported the formation of an iridium–oxo complex leading to an O–O bond

formation from the reaction of two H_2O molecules with a $Cp^*Ir(O)(ppy)^+$ complex, where ppy is 2-phenylpyridine.[16,17] Moreover, Joya et al. succeeded in synthesizing an oxidant-free iridium–oxo complex that catalyzing H_2O oxidation leading to the O_2 evolution on an Indium Tin Oxide (ITO) electrode at mild conditions.[22]

More recently, Ogo and coworkers reported an interesting iridium–aqua complex $[Ir^{III}(\eta^5\text{-}C_5Me_5)\{bpy(COOH)_2\}(H_2O)]^{2+}$ (**Ir^{III}–OH_2**), where $bpy(COOH)_2$ is 2,2'-bipyridine-4,4'-dicarboxylic acid, catalyzing H_2O oxidation through high-valent iridium–oxo complex $[Ir^{V}(\eta^5\text{-}C_5Me_5)\{bpy(COOH)_2\}(O)]^{2+}$ (**Ir^{V}=O**).[23] This catalyst, together with a tungsten oxide (WO_3) electrode on the anode and a carbon-supported platinum (Pt/C) electrode on the cathode, creates a system capable of functionalities as solar cells, where **Ir^{V}=O** being active species of O–O bond formation by reacting with H_2O is formed by harvesting visible-light. Moreover, this iridium complex has a robustness and a stability in a water solution. Although this system is very interesting methods that a high-valent iridium–oxo being capable of oxidizing substrate is formed without oxidant- and external power-free, it is not yet clear in what fashion H_2O is oxidized to from O_2. In this chapter, the catalytic mechanism of H_2O oxidation by **Ir^{III}–OH_2** is investigated by performing density functional theory (DFT). This present study is important to provide an in-deep mechanistic understanding on the design of catalyst oxidizing not only a H_2O molecule but also other substrate.

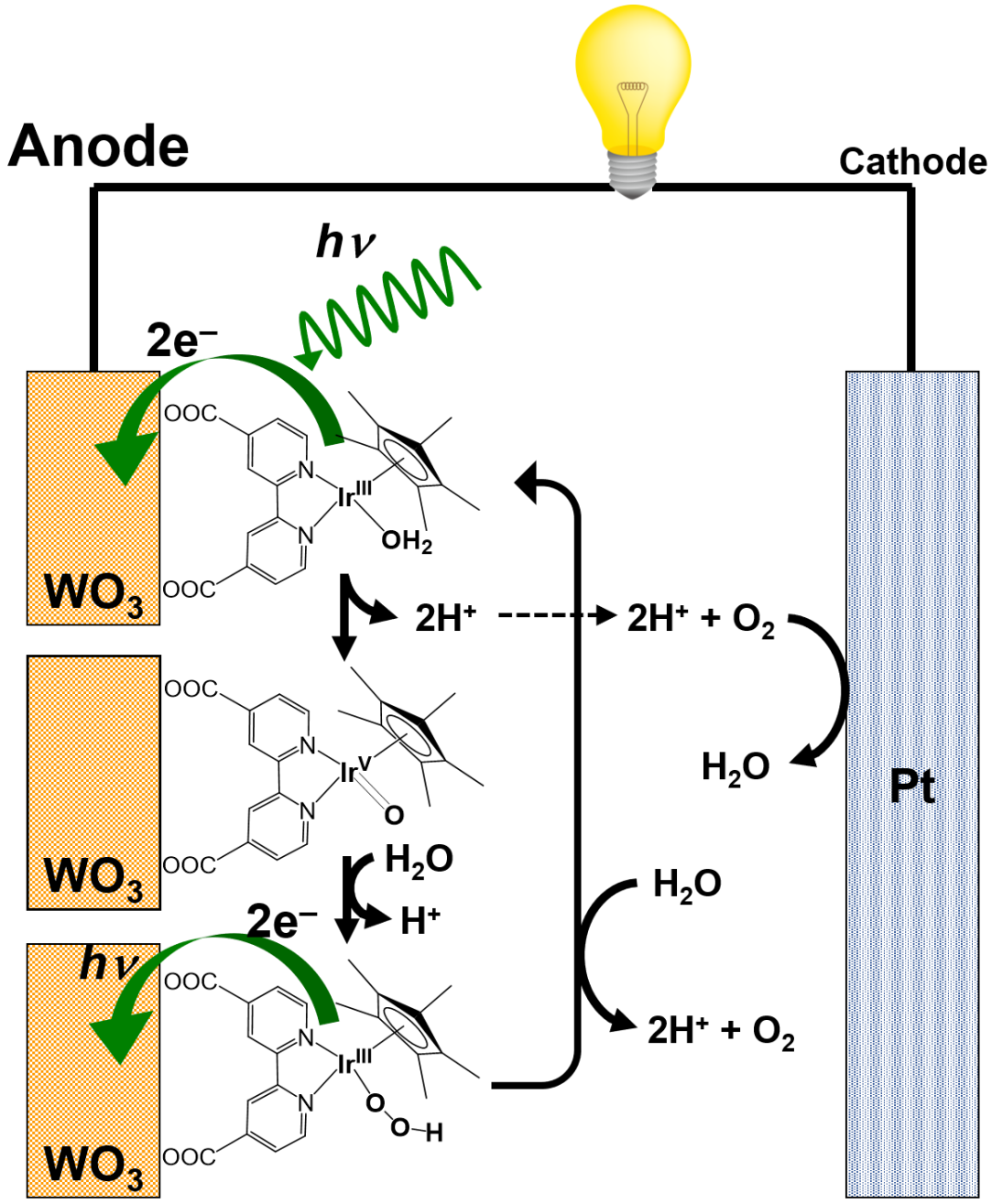

Figure 2-1. Schematic representation of fuel cell capable of catalytic water oxidation by Ir-aqua complex $[Ir^{III}(\eta^5\text{-}C_5Me_5)\{bpy(COOH)_2\}(H_2O)]^{2+}$ in anode by harvesting light, reported by Ogo and coworkers.[23]

2.2 Computational methodology

2.2.1 Computational method

All reaction intermediates and transition states were calculated by using the B3LYP-D3 functional,[24-27] as implemented in the Gaussian 16 program package.[28] TZVP basis set[29] for

the H, C, N, and O atoms and SDD basis set[30] for the Ir atom are used. By calculating the analytical harmonic vibration frequencies, we confirmed that the obtained ground states and transition states have, respectively, no and one imaginary frequency. The obtained energy values include the zero-point energy correction (ZPC) except those in the electrode reactions, where free energies under 333.25 K and 1 atm were considered.[23] Considering that the high humidity in the real operation conditions of fuel cells results in water vapor around the electrode and $\mathbf{Ir^{III}–OH_2}$, implicit solvent effects of H_2O with a dielectric constant of 78.39 were considered and predicted by using the polarized continuum model.[31-34] Because hydronium ion (H_3O^+) as a proton source is highly acidic, we considered a $H^+(H_2O)_3$ cluster as a more reasonable and widely accepted[35-43] model of H^+ in water solution (Figure 2-2). The attachment and detachment of $(H_2O)_3$ and $H^+(H_2O)_3$ clusters considered in this study are required to rationalize the experimental findings and have been widely used by other researchers.[45-44]

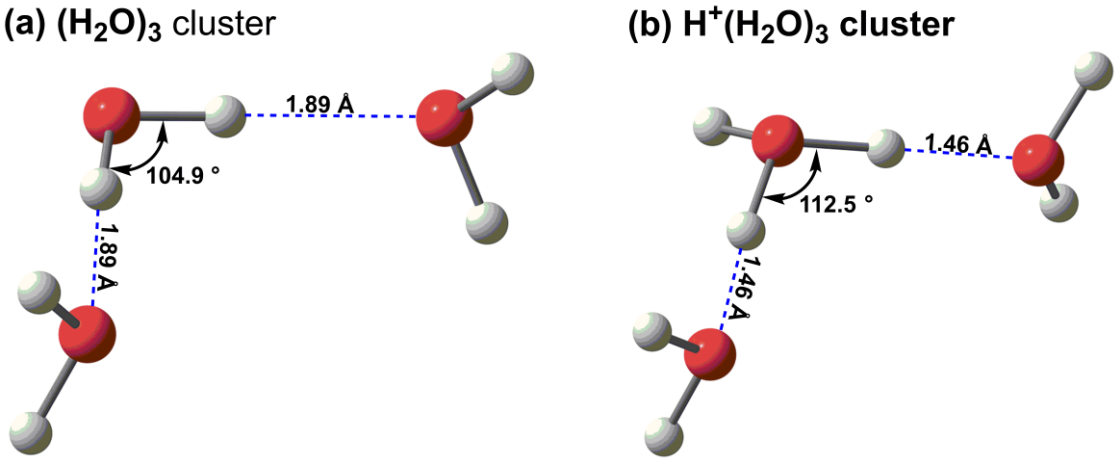

Figure 2-2. The Optimized geometries of (a) $(H_2O)_3$ cluster and (b) $H^+(H_2O)_3$ cluster models. Units are in Å and degree

To evaluate the electrode reactions, we calculated oxidation potentials which involves electron transfer from the iridium complex to out of the system and proton release. Oxidation half potentials ($E_{1/2}$) were calculated using the following equations.

$$\mathrm{AH}_{n_\mathrm{H}}^{(n_\mathrm{H}-n_e)} \rightarrow \mathrm{A} + n_e e^- + n_\mathrm{H}\mathrm{H}^+ \qquad (2-2)$$

where ne and n_H stand for the number of electrons and protons, respectively. The oxidation potential is related to the standard oxidation free energy in the water solution by

$$-n_e F E^\circ = \Delta G^\circ_{\mathrm{EA}} = G^\circ(\mathrm{A}^{-n_e}) - G^\circ(\mathrm{A}) \qquad (2-3)$$

where $\Delta G^\circ_{\mathrm{EA}}$ is free energy change associated with an oxidation in a solvent environment at standard condition and *F* is the Faraday constant. The standard oxidation half potential (assuming $n_H = 0$), i.e. $E^\circ_{1/2}$, is related to $\Delta G^\circ_{\mathrm{EA}}$ by

$$\Delta G^\circ_{\mathrm{EA}} = \Delta G^\circ_{1/2} = G^\circ\left(\mathrm{AH}^{(n_H - n_e)}_{n_H}\right) - G^\circ(\mathrm{A}) - n_H G^\circ(\mathrm{H}^+) = n_e F E^\circ_{1/2} \qquad (2-4)$$

In our model, we described $G^\circ(H^+)$ using following equations

$$G^\circ(\mathrm{H}^+) = G^\circ(\mathrm{H}^+(\mathrm{H_2O})_3) - G^\circ((\mathrm{H_2O})_3) \qquad (2-5)$$

The dependence of the oxidation half potential on pH is obtained from the Nernst equation, where nonstandard $E_{1/2}$ is calculated using the following equation

$$E_{1/2} = -\left(\frac{\Delta G^\circ_{1/2}}{n_e}\right) - \frac{\mathrm{RTln}(10) n_H}{n_e}\mathrm{pH} - E^{\circ,\mathrm{ref}}_{1/2} \qquad (2-6)$$

where $E^{\circ,\mathrm{ref}}{}_{1/2}$ is the reference potential (usually standard hydrogen electrode (SHE) at 4.24 V).[45-46] This approach is a widely accepted method. [47-49]

2.2.2 Computational model

Figure 2-3 (a) and (b) shows the structures of **Ir^{III}–OH_2** obtained from the X-ray measurement[23] and present DFT calculations, respectively. In the real experimental conditions, **Ir^{III}–OH_2** is immobilized over WO_3 electrode, where H atoms of the bpy$(COOH)_2$ moiety is separated to form bpy$(COO^-)_2$ bonding to W atoms. However, for simplicity, in this study the number of atoms in the bpy$(COOH)_2$ moiety is kept for all reaction steps and the effects of the electrodes are not considered. Calculated distance in Ir–O, Ir–N1, and Ir–N2 bonds and d_{Cp^*} in **Ir^{III}–OH_2** are calculated to be 2.27, 2.12, 2.12, and 2.21 Å, respectively, which are slightly longer than the corresponding experimental values of 2.16, 2.10, and 2.10, and 2.16 Å. However, it is widely accepted that these small errors are due to the tendency of DFT methods.[19,50,51] Moreover, Kazaryan et al. demonstrated that the B3LYP-D3 method, compared to the CCSD(T) method as a benchmark, is accurate enough for calculating energy diagrams of H_2O oxidation over a similar half-sandwich iridium complex.[52] Additionally, the bond distance around Ir center (Ir–N1, and Ir–N2 bonds and d_{Cp^*}) in **Ir^{V}=O** remains unchanged (Ir–N1: 2.14 Å, Ir–N2: 2.14 Å, d_{Cp^*}: 2.29 Å,) during following reaction (**Ir^{III}–OH_2** → **Ir^{V}=O** + $2H^+ + 2e^-$). Therefore, this is assumed to be reasonable electrode removal catalyst model.

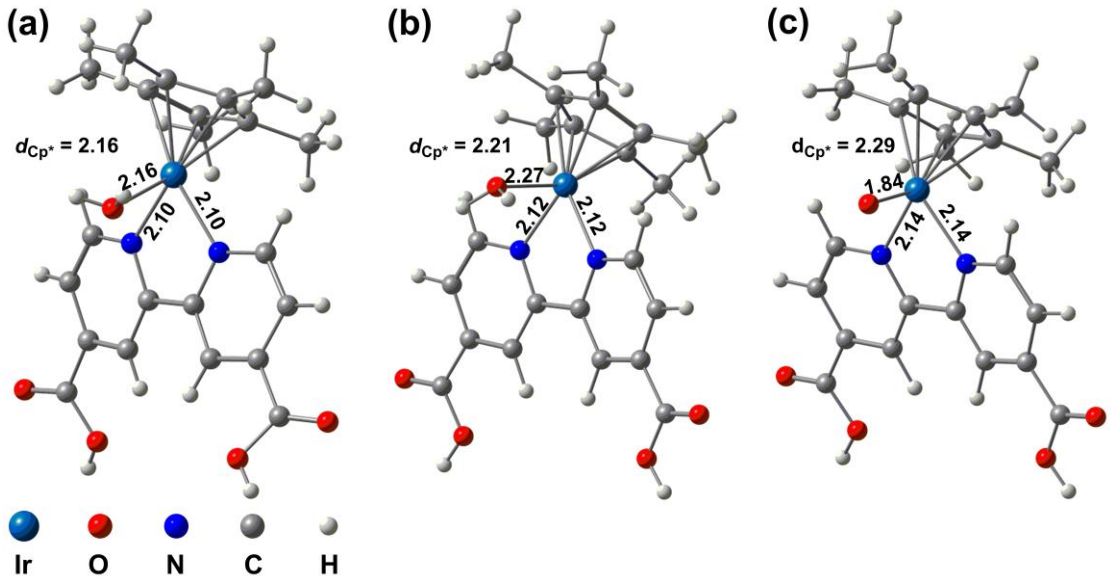

Figure 2-3. (a) X-ray crystal and (b)DFT-optimized structures of the Ir-aqua complex (**Ir^{III}–OH_2**) and (c) DFT-optimized structure od Ir-oxo complex (**Ir^{V}=O**). d_{Cp^*} denotes the average bond distance between Ir and C atoms of the Cp* ring. Distances are in Å.

2.3 Results and discussion

Figure 2-4 shows a schematic representation of computational suggestions for the catalytic cycle of H_2O oxidations. In this cycle there are two electrode reactions (green line (1) and (3)) and one thermal reaction (blue line (2)). First, a two-electron oxidation of **Ir^{III}–OH_2** (1) occurs to form **Ir^{V}=O** (**Ir^{III}–OH_2** → **Ir^{V}=O** + $2H^+ + 2e^-$). After that, an O–O bond formation (2) proceeds by reacting **Ir^{V}=O** with a H_2O molecule to form **Ir^{III}–OOH**, where a proton is release. Finally, two-electron oxidation (3) takes place to form **Ir^{III}–OH_2** and O_2 with a ligand exchange reaction between H_2O and O_2 molecules. We first discuss about the formation of **Ir^{V}=O** from **Ir^{III}–OH_2** with a square scheme. Next, we discuss the O–O bond formation (2) using an energy diagram and then briefly describe the reaction pathways for the regeneration of **Ir^{III}–OH_2** using a square scheme.

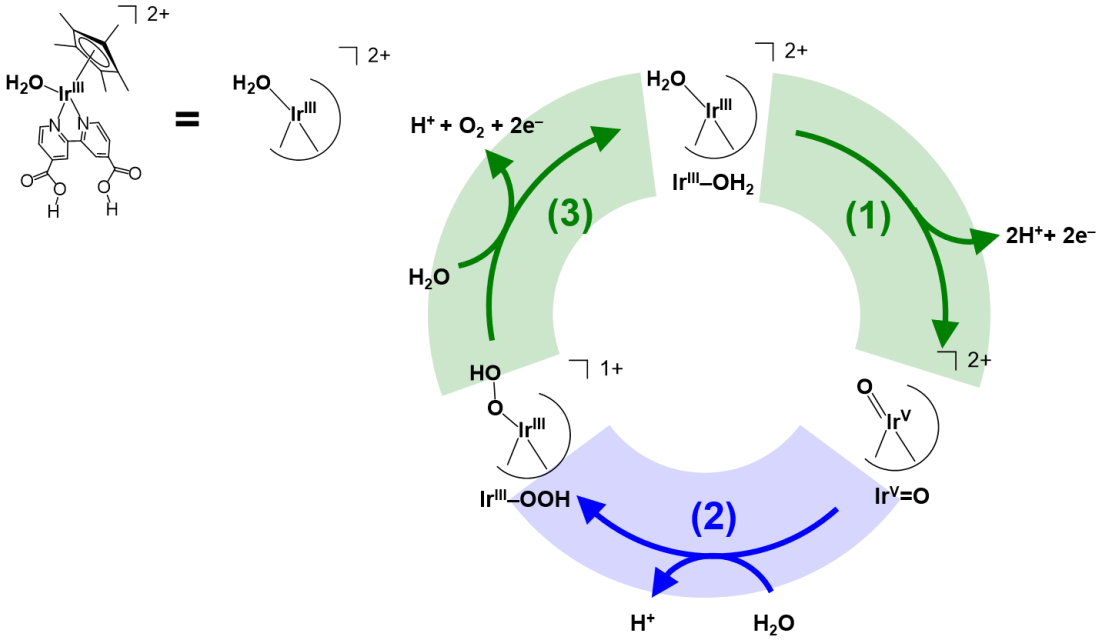

Figure 2-4. Catalytic cycle of water oxidation catalyzed by Ir-aqua complex $[Ir^{III}(\eta^5\text{-}C_5Me_5)\{bpy(COOH)_2\}(H_2O)]^{2+}$, where $bpy(COOH)_2$ is 2,2'-bipyridine-4,4'-dicarboxylic acid.

2.3.1 Formation of Ir^{V}=O from Ir^{III}–OH_2 (1)

In this reaction, a two-electron oxidation of **Ir^{III}–OH_2** to **Ir^{V}=O** takes place on the WO_3 electrode according to the following reaction: **Ir^{III}–OH_2** → **Ir^{V}=O** + $2H^+$ + $2e^-$. Scheme 2-1 shows a square scheme of this reaction, where solid lines is computational suggesting plausible reaction. As shown in Scheme 2-1, the first step is the deprotonation reaction because one-oxidation corresponding to following reaction: **Ir^{III}–OH_2** → **Ir^{IV}–OH_2** + e^-, requires rather high oxidation potential (2.58 V). A deprotonation free energy (**Ir^{III}–OH_2** → **Ir^{III}–OH** + $2H^+$) is calculated to be 14.7 kcal/mol. Subsequently, a one-electron oxidation of **Ir^{III}–OH** proceeds to form a hydroxyl complex (**Ir^{IV}–OH**) with $E_{1/2}$ of 1.44 V, which is higher than the oxidation potential of H_2O (1.23 V), This indicates that this reaction should occur with the assistance of light irradiation. Calculated a total spin population of Ir and O atoms is 0.86 $e^-/Å^3$, which is assigned to Ir^{IV} center. Afterward, since one-electron oxidation corresponding to following reaction: **Ir^{IV}–OH** → **Ir^{V}–OH** + e^-, requires rather high oxidation potential (3.27 V), next step is considered to be the deprotonation reaction. A second deprotonation occurs to form **Ir^{IV}–O**, requiring a high deprotonation free energy of 22.0 kcal/mol. The computed total spin

population for Ir and O atoms in **Ir^{IV}–O** is 0.99 e$^-$/Å^3, showing that an iridium-oxyl radical (Ir=O$^•$) is formed. Finally, **Ir^{IV}–O** is oxidized to form **Ir^{V}=O**, where the ground state is changed from the double state to the triplet state. $E_{1/2}$ of this final step is calculated to be 1.19 V.

Scheme 2-1. Square Scheme of Reaction: Ir^{III}–OH$_2$ → Ir^{V}=O + 2H$^+$ + 2e$^-$.

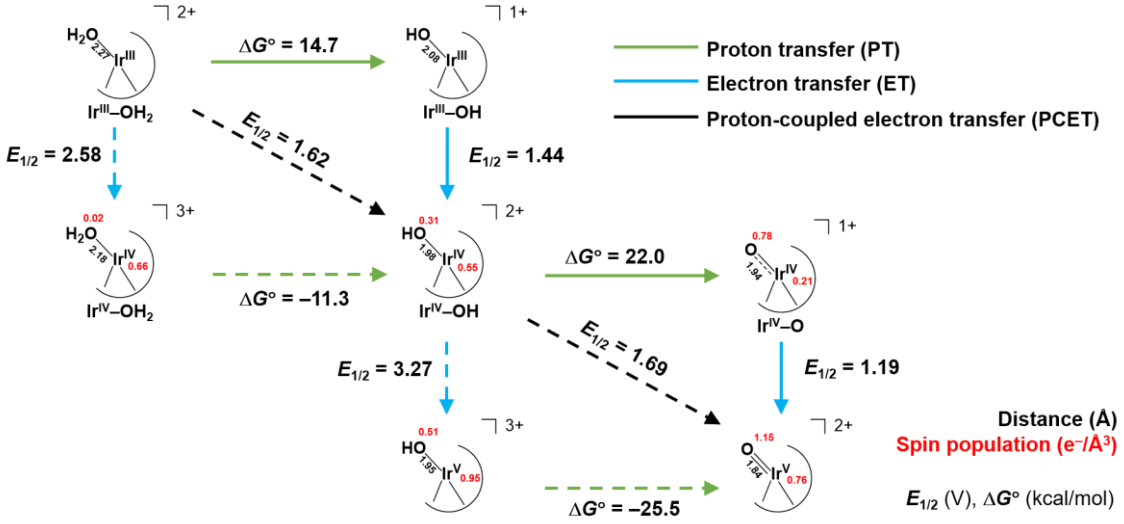

2.3.2 O–O bond formation by reacting Ir^{V}=O with H$_2$O (2)

We next investigate the H$_2$O oxidation (2), where an O–O bond is formed by reacting **Ir^{V}=O** with H$_2$O molecules. Figure 2-5 shows computed energy diagrams for the O–O bond formation involving one or two H$_2$O molecules corresponding to **Path1** and **Path2**, respectively.[17] **Ir^{V}=O** has three spin state, i.e. triplet, open-shell singlet (^{OS}singlet), and closed-shell singlet (^{CS}singlet) state corresponding to black, red and blue lines, respectively. As shown in figure, **Ir^{V}=O** prefers the triplet state as the ground state, whereas **Ir^{V}=O** in the ^{OS}singlet and ^{CS}singlet state, respectively, lie 6.7 and 7.3 kcal/mol above that in the triplet state. In **Path1**, the first step of the adsorption of a H$_2$O molecule leading to the formation of reactant complex (**rc1**) give arise to the energetically stabilization by 4.2, 4.7, and 4.6 kcal/mol in the triplet, ^{OS}singlet, and ^{CS}singlet state, respectively. Subsequent reaction corresponding to a H atom abstraction in the H$_2$O molecule by Ir^{V}=O species requires activation energies of 23.9, 18.6, and 29.4 kcal/mol in the triplet, ^{OS}singlet, and ^{CS}singlet state, respectively. This reaction in the triplet state leads to the radical intermediate consisting of hydroxyl-radical (•OH) and **Ir^{IV}–OH**, whereas **ts1** in the ^{OS}singlet, and ^{CS}singlet state leads to the H$_2$O$_2$ complex (**Ir^{III}–O$_2$H$_2$**), directly. Because the activation energy in the ^{CS}singlet state is rather high than that in the triplet and

^{OS}singlet states, we conclude that a H atom abstraction by Ir^{V}=O species proceeds in the triplet state, and a spin inversion from triplet to ^{CS}singlet is expected to occur after **ts1** to form **Ir^{III}–O_2H_2**.

Path2, on the other hand, leads to the O–O bond formation without H atom abstraction. **Path2** begins with an exothermic adsorption of two H_2O molecules on **Ir^{V}=O** to form **rc2** with an adsorption energy of –9.5 kcal/mol and –9.6 kcal/mol in the triplet and ^{cs}singlet state, respectively. Subsequently, the oxo ligand of **^{3}rc2** reacts with one of the adsorbed H_2O molecules via **^{1}ts2** to form a dioxygen complex (**^{1}int2**) involving an oxo-water ligand (–OOH_2). The activation energy for this reaction step is calculated to be 21.0 kcal/mol with a spin inversion from the triplet state to the ^{CS}singlet state being expected to occur before **^{1}ts2**. During the O–O bond formation from **^{3}rc2** to **^{1}int2**, no radical species are formed and the formal charge of Ir atom is changed from +5 to +3 by a two-electron transfer from the O atom in the H_2O molecules to the Ir center. This indicates that the O–O bond formation occurs through the water nucleophilic attack (WNA) mechanism, where a lone pair in a H_2O molecule attacks to unoccupied π* orbital in the high-valent Ir^{V}=O species. The reverse reaction from **^{1}int2** to **^{3}rc2** is more likely to occur with an activation barrier of only 1.5 kcal/mol, indicating a weak O–O bond in **^{1}int2**. This is consistent with the optimized geometries that the O–O bond in **^{1}int2** is 1.51 Å being by 0.28 Å longer than that for O_2 molecules in the gas phase.[53] Nonetheless, **^{1}int2** may readily be stabilized by the deprotonation without barrier to form **Ir^{III}–OOH**, indicate that this activation barrier low enough for the reaction to proceed at mild conditions. The O–O bond in **Ir^{III}–OOH** is 1.46 Å, indicating that OOH moieties is hydroperoxide.

Computational results show that the activation energy in **Path2** (21.0 kcal/mol) is slightly lower than in **Path1** (23.9 kcal/mol). Therefore, the O–O bond formation reaction proceed in **Path2** through WNA mechanism. These results are consistent with the previous DFT study by Blakemore et al.[17]

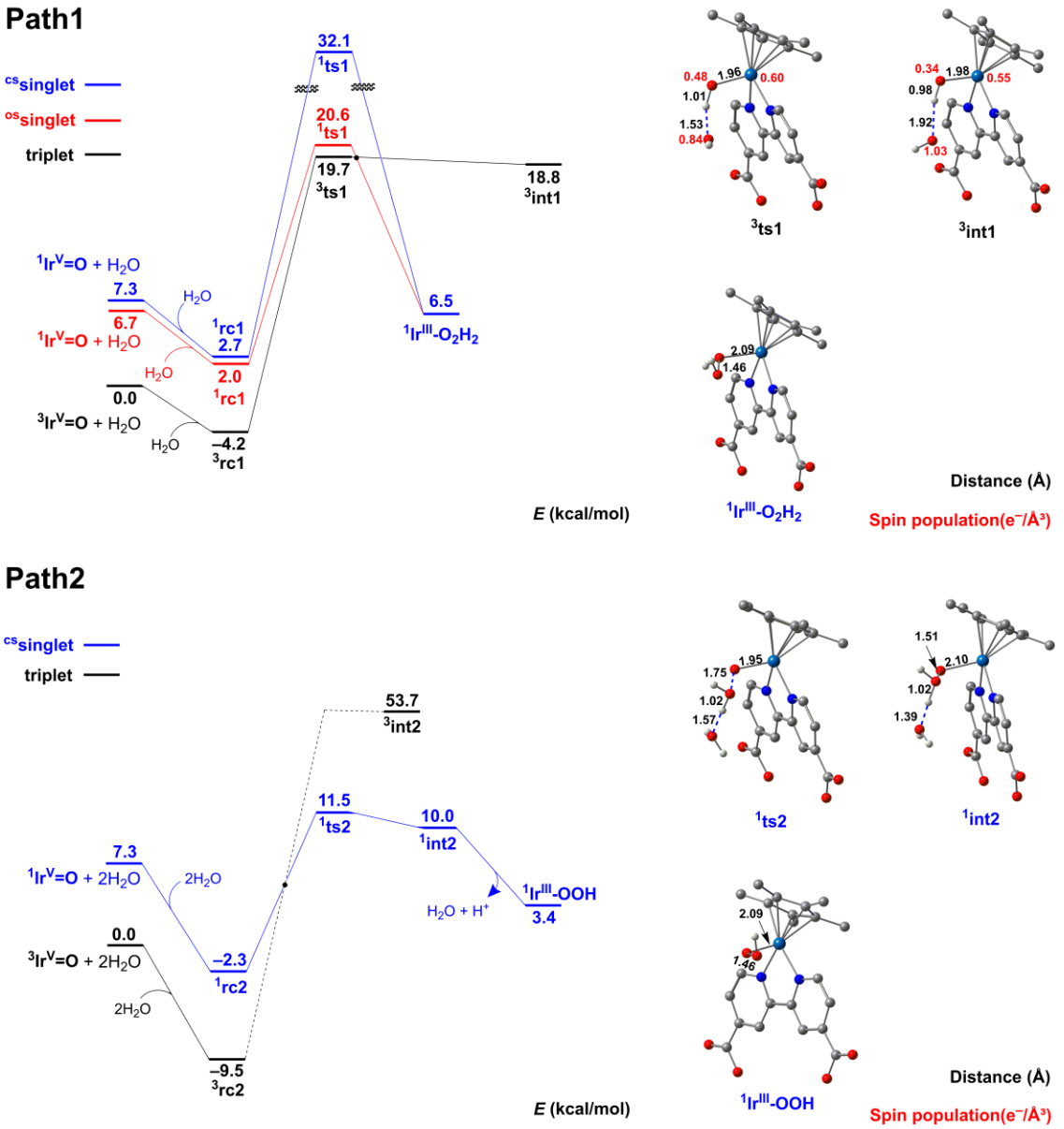

Figure 2-5. Energy diagrams of water oxidation reaction by **Ir^{V}=O** via Path1 and Path2 involving one and two water molecules, respectively, and ball-and-stick models of optimized geometries in the **^{3}ts1**, **^{3}int1**, **$^{1}Ir^{III}$-O_2H_2**, **^{1}ts2**, **^{1}int2**, and **$^{1}Ir^{III}$-OOH**, where the superscripts describe the spin state. Black, red and blue lines in the energy diagrams indicate the triplet, open-shell singlet and closed-shell singlet state, respectively.

2.3.3 Regeneration of Ir^{III}–OH_2 (3)

In this reaction, a two-electron oxidation and one proton dissociation are occurred on the WO_3 electrode, leading to the regeneration of initial complex (**Ir^{III}–OH_2**) through a ligand exchange between O_2 and H_2O molecules. Scheme 2-2 shows a square scheme of the following reaction: **Ir^{III}–OOH** + H_2O → **Ir^{III}–OH_2** + H^+ + $2e^-$ + O_2, where solid lines is computational suggesting plausible reaction. As shown in Scheme 2-2, **Ir^{III}–OOH** initially releases one proton to solvent and one electron to the WO_3 electrode to form a Ir-dioxygen complex (**Ir^{III}–$O_2^{\bullet-}$**) through proton-coupled electron transfer (PCET), where $E_{1/2}$ is calculated to be 0.83 V. Since the O–O bond in dioxygen moiety is 1.31 Å and the sum of spin population is 1.02 e^-/$Å^3$, the dioxygen moieties is assigned to superoxo ligand ($O_2^{\bullet-}$). After that, a ligand exchange between O_2 moiety and a H_2O molecule occurs to form **Ir^{II}–OH_2**, where the Ir center is reduced to Ir^{II} by $O_2^{\bullet-}$ with a reaction free energy of 7.9 kcal/mol. The final step is the one-electron oxidation of **Ir^{II}–OH_2** to **Ir^{III}–OH_2** as discussed in Scheme2-2, where $E_{1/2}$ is calculated to be 0.24 V. This electrode reaction requires of rather small value of $E_{1/2}$, indicating that **Ir^{III}–OOH** is converted to **Ir^{III}–OH_2** immediately.

Scheme 2-2. Square Scheme of Reaction: Ir^{III}–OOH + H_2O → Ir^{III}–OH_2 + H^+ + $2e^-$ + O_2.

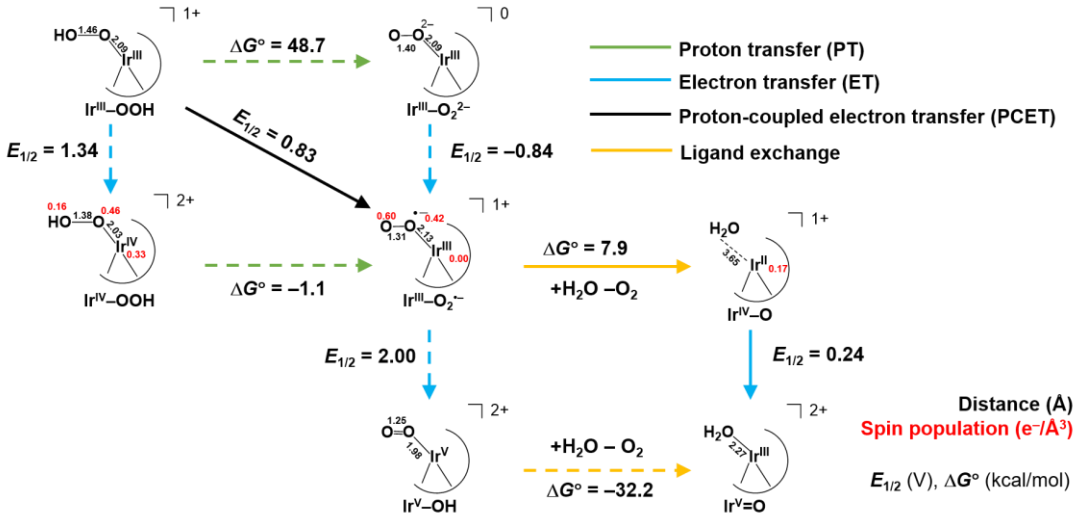

2.4 Conclusions

In this chapter, detailed mechanisms for the catalytic cycle of H_2O oxidations by the iridium–aqua complex $[Ir^{III}(\eta^5\text{-}C_5Me_5)\{bpy(COOH)_2\}(H_2O)]^{2+}$ (**Ir^{III}–OH_2**) toward the design of devices capable of light-driven fuel cell that oxidize substrate have been proposed and discussed by performing DFT calculations. Three key intermediate structures (i.e. aqua complex **Ir^{III}–OH_2**, oxo complex **Ir^{V}=O**, and hydroperoxide complex **Ir^{III}–OOH**) and three reaction steps (i.e. **Ir^{III}–OH_2** → **Ir^{V}=O** → **Ir^{III}–OOH** → **Ir^{III}–OH_2**) to the catalytic cycle was suggested. In the H_2O oxidation cycle, **Ir^{III}–OH_2** initially release two protons and two electrons to form **Ir^{V}=O**, where the oxidation half potential ($E_{1/2}$) corresponding to the oxidation of Ir center (Ir^{III} → Ir^{IV}) require 1.44 V being higher than the oxidation potential of H_2O (1.23 V). After the formation of **Ir^{V}=O**, a H_2O molecule attacks to Ir^{V}=O species through water nucleophilic attack (WNA) mechanism to form an oxo-water ligand (–OOH_2) intermediate with a weak O–O bond, where the activation energy is calculated to be 21.0 kcal/mol. Due to its instability, this ligand is spontaneously deprotonated to –OOH ligand (**Ir^{III}–OOH**) with a stronger O–O bond. Subsequently, **Ir^{III}–OOH** releases a proton and an electron concertedly through PCET mechanism to form **Ir^{III}–$O_2^{\bullet-}$**, which undergoes a ligand exchange between H_2O and O_2 molecules and the oxidation of Ir center, leading to the regeneration of **Ir^{III}–OH_2**. These computational results describe that two reactions (**Ir^{V}=O** → **Ir^{III}–OOH** and **Ir^{III}–OOH** → **Ir^{III}–OH_2**) easily proceed at the experimental condition. In contrast, the formation of **Ir^{V}=O** (**Ir^{III}–OH_2** → **Ir^{V}=O**) requires external-power. Therefore, it is concluded that **Ir^{V}=O** is an important intermediate for the catalytic cycles of H_2O oxidation.

Reference

1. Chow, J.; Kopp, R. J.; Portney, P. R. Energy Resources and Global Development. *Science* **2003**, *302*, 1528-1531.

2. Lewis, N. S.; Nocera, D. G. Powering the Planet: Chemical Challenges in Solar Energy Utilization. *Proc. Natl. Acad. Sci. U.S.A.* **2006**, *103*, 15729−15735.

3. Sun, L.; Hammarström, L.; Åkermark, B.; Styring, S. Towards Artificial Photosynthesis: Ruthenium-Manganese Chemistry for Energy Production. *Chem. Soc. Rev.* **2001**, *30*, 36−49.

4. Tachibana, Y.; Vayssieres, L.; Durrant, J. R. *Artificial Photosynthesis for Solar Water-Splitting*. *Nat. Photonics* **2012**, *6*, 511−518.

5. Kärkäs, M. D.; Johnston, E. V.; Verho, O.; Åkermark, B. Artificial Photosynthesis: From Nanosecond Electron Transfer to Catalytic Water Oxidation. *Acc. Chem. Res.* **2014**, *47*, 100−111.

6. Allakhverdiev, S. I.; Casal, J. J.; Nagata, T. Photosynthesis from Molecular Perspectives: Towards Future Energy Production. *Photochem. Photobiol. Sci* **2009**, *8*, 137−138.

7. Umena, Y.; Kawakami, K.; Shen, J.-R.; Kamiya, N. Crystal Structure of Oxygen-Evolving Photosystem II at a Resolution of 1.9 Å. *Nature* **2011**, *473*, 55−60.

8. McEvoy, J. P.; Brudvig, G. W. Water-Splitting Chemistry of Photosystem II. *Chem. Rev.* **2006**, *106*, 4455−4483.

9. Cox, N.; Pantazis, D. A.; Neese, F.; Lubitz, W. Biological Water Oxidation. *Acc. Chem. Res.* **2013**, *46*, 1588−1596.

10. Yano, J.; Yachandra, V. Mn_4Ca Cluster in Photosynthesis: Where and How Water Is Oxidized to Dioxygen. *Chem. Rev.* **2014**, *114*, 4175−4205.

11. Blakemore, J. D.; Crabtree, R. H.; Brudvig, G. W. Molecular Catalysts for Water Oxidation. *Chem. Rev.* **2015**, *115*, 12974−13005.

12. Kärkäs, M. D.; Verho, O.; Johnston, E. V.; Åkermark, B. Artificial Photosynthesis: Molecular Systems for Catalytic Water Oxidation. *Chem. Rev.* **2014**, *114*, 11863−12001.

13. Cady, C. W.; Crabtree, R. H.; Brudvig, G. W. Functional Models for the Oxygen-Evolving Complex of Photosystem II. *Coord. Chem. Rev.* **2008**, *252*, 444−455.

14. Gersten, S. W.; Samuels, G. J.; Meyer, T. J. *J. Am. Chem. Soc.* **1982**, *104*, 4029– 4030.

15. Gilbert, J. A.; Eggleston, D. S.; Murphy, W. R., Jr.; Geselowitz, D. A.; Gersten, S. W.; Hodgson, D. J.; Meyer, T. J. Structure and Redox Properties of the Water-Oxidation Catalyst $[(bpy)_2(OH_2)RuORu(OH_2)(bpy)_2]^{4+}$. *J. Am. Chem. Soc.* **1985**, *107*, 3855−3864.

16. Hull, J. F.; Balcells, D.; Blakemore, J. D.; Incarvito, C. D.; Eisenstein, O.; Brudvig, G. W.; Crabtree, R. H. Highly Active and Robust Cp* Iridium Complexes for Catalytic Water Oxidation. *J. Am. Chem. Soc.* **2009**, *131*, 8730−8731.

17. Blakemore, J. D.; Schley, N. D.; Balcells, D.; Hull, J. F.; Olack, G. W.; Incarvito, C. D.; Eisenstein, O.; Brudvig, G. W.; Crabtree, R. H. Half-Sandwich Iridium Complexes for Homogeneous Water-Oxidation Catalysis. *J. Am. Chem. Soc.* **2010**, *132*, 16017−16029.

18. Grotjahn, D. B.; Brown, D. B.; Martin, J. K.; Marelius, D. C.; Abadjian, M. C.; Tran, H. N.; Kalyuzhny, G.; Vecchio, K. S.; Specht, Z. G.; Cortes-Llamas, S. A.; Miranda-Soto, V.; van Niekerk, C.; Moore, C. E.; Rheingold, A. L. Evolution of Iridium-Based Molecular Catalysts during Water Oxidation with Ceric Ammonium Nitrate. *J. Am. Chem. Soc.* **2011**, *133*, 19024-19027.

19. Vilella, L.; Vidossich, P.; Balcells, D.; Lled**ó**s, A. Basic Ancillary Ligands Promote O–O Bond Formation in Iridium-Catalyzed Water Oxidation: A DFT study. *Dalton Trans.*, **2011**, *40*, 11241−11247.

20. Zhang, T.; deKrafft, K. E.; Wang, J.-L.; Wang, C.; Lin, W. The Effects of Electron-Donating Substituents on $[Ir(bpy)Cp^*Cl]^+$: Water Oxidation versus Ligand Oxidative Modifications. *Eur. J. Inorg. Chem.* **2014**, *4*, 698-707.

21. Thomsen, J. M.; Huang, D. L.; Crabtree, R. H. Brudvig, G. W. Iridium-Based Complexes for Water Oxidation. *Dalton Trans.*, **2015**, *44*, 12452−12472.

22. Joya, K. S.; Subbaiyan, N. K.; D'Souza, F.; de Groot, H. J. M. Surface-Immobilized Single-Site Iridium Complexes for Electrocatalytic Water Splitting. *Angew. Chem., Int. Ed.* **2012**, *51*, 9601−9605.

23. Kikkawa, M.; Yatabe, T.; Matsumoto, T.; Yoon, K.-S.; Suzuki, K.; Enomoto, T.; Kaneko,

K.; Ogo, S. A Fusion of Biomimetic Fuel and Solar Cells Based on Hydrogenase, Photosystem II, and Cytochrome c Oxidase. *ChemCatChem* **2017**, *9*, 4024−4028.

24. Becke, A. D. Density-Functional Exchange-Energy Approximation with Correct Asymptotic Behavior. *Phys. Rev. A*, **1988**, *38* 3098−3100.

25. Lee, C.; Yang, W.; Parr. R. G. Development of the Colle-Salvetti Correlation-Energy Formula into a Functional of the Electron Density. *Phys. Rev. B*, **1988**, *37*, 785−789.

26. Becke, A. D. Density-Functional Thermochemistry. III. The Role of Exact Exchange. *J. Chem. Phys.*, **1993**, *98*, 1372−1377.

27. Grimme, S.; Antony, J.; Ehrlich S.; Krieg H. A Consistent and Accurate *ab initio* Parametrization of Density Functional Dispersion Correction (DFT-D) for the 94 Elements H-Pu. *J. Chem. Phys.*, **2010**, *132*, 154104.

28. Frisch, M. J.; Trucks, G. W.; Schlegel, H. B.; Scuseria, G. E.; Robb, M. A.; Cheeseman, J. R.; Scalmani, G.; Barone, V.; Petersson, G. A.; Nakatsuji, H.; Li, X.; Caricato, M.; Marenich, A. V.; Bloino, J.; Janesko, B. G.; Gomperts, R.; Mennucci, B.; Hratchian, H. P.; Ortiz, J. V.; Izmaylov, A. F.; Sonnenberg, J. L.; Williams-Young, D.; Ding, F.; Lipparini, F.; Egidi, F.; Goings, J.; Peng, B.; Petrone, A.; Henderson, T.; Ranasinghe, D.; Zakrzewski, V. G.; Gao, J.; Rega, N.; Zheng, G.; Liang, W.; Hada, M.; Ehara, M.; Toyota, K.; Fukuda, R.; Hasegawa, J.; Ishida, M.; Nakajima, T.; Honda, Y.; Kitao, O.; Nakai, H.; Vreven, T.; Throssell, K.; Montgomery, J. A., Jr.; Peralta, J. E.; Ogliaro, F.; Bearpark, M. J.; Heyd, J. J.; Brothers, E. N.; Kudin, K. N.; Staroverov, V. N.; Keith, T. A.; Kobayashi, R.; Normand, J.; Raghavachari, K.; Rendell, A. P.; Burant, J. C.; Iyengar, S. S.; Tomasi, J.; Cossi, M.; Millam, J. M.; Klene, M.; Adamo, C.; Cammi, R.; Ochterski, J. W.; Martin, R. L.; Morokuma, K.; Farkas, O.; Foresman, J. B.; Fox, D. J. *Gaussian 16*, Revision A. 03; Gaussian, Inc.: Wallingford ,CT, 2016.

29. Schaefer, A.; Huber, C.; Ahlrichs, R. Fully Optimized Contracted Gaussian Basis Sets of Triple Zeta Valence Quality for Atoms Li to Kr. *J. Chem. Phys.*, **1994**, 100, 5829−5835.

30. Andrae, D.; Haeussermann, D.; Dolg, M.; Stoll, H.; Preuss, H. Energy-Adjusted *ab initio* Pseudopotentials for the Second and Third Row Transition Elements. *Theor. Chem. Acc.*, **1990**, *77*, 123−141.

31. Tomasi, J.; Mennucci, B.; Cammi, R. Quantum Mechanical Continuum Solvation Models. *Chem. Rev.*, **2005** *105*, 2999−3093.

32. Cossi, M.; Barone, V.; Cammi, R.; Tomasi, J. Ab initio Study of Solvated Molecules: A New Implementation of the Polarizable Continuum Model. *Chem. Phys. Lett.*, **1996**, *255*, 327−335.

33. Cances, E.; Mennucci, B.; Tomasi, J. A New Integral Equation Formalism for the Polarizable Continuum Model: Theoretical Background and Applications to Isotropic and Anisotropic Dielectrics. *J. Chem. Phys.*, **1997**, *107*, 3032−3041.

34. Barone, V.; Cossi, M. Quantum Calculation of Molecular Energies and Energy Gradients in Solution by a Conductor Solvent Model. *J. Phys. Chem. A.*, **1998,** *102*, 1995−2001.

35. Heuft, J. M.; Meijer, E. J. A Density Functional Theory Based Study of the Microscopic Structure and Dynamics of Aqueous HCl Solutions. *Phys. Chem. Chem. Phys.*, **2006**, *8*, 3116-3123.

36. Calleja, M.; Mason, S. A.; Prince, P. D.; Steed, J. W.; Wilkinson, C. Single Crystal Neutron and X-ray Diffraction Studies of $(H_7O_3)[AuCl_4]$•15-crown-5. *New J. Chem.*, **2001**, *25*, 1475-1478.

37. Kurniawan, D.; Morita, S.; Kitagawa, K. Hydration Structure of Trifluoromethanesulfonate Studied by Quantum Chemical Calculation. *Comput. Theor. Chem.*, **2012**, *982*, 30-33.

38. Stoyanov, E. S.; Stoyanova, I. V.; Tham F. S.; Reed, C. A. The Nature of the Hydrated Proton $H_{(aq)}^+$ in Organic Solvents. *J. Am. Chem. Soc.* **2018**, *130*, 12128-12138.

39. Chen, H.-T.; Chang, J.-G.; Chen, H.-L. A Computational Study on the Decomposition of Formic Acid Catalyzed by $(H_2O)_x$, x = 0–3: Comparison of the Gas-Phase and Aqueous-Phase Results. *J. Phys. Chem. A* **2008**, *112*, 8093–8099.

40. Inaba, S. Theoretical Study of Water Cluster Catalyzed Decomposition of Formic Acid. *J. Phys. Chem. A* **2014**, *118*, 3026–3038.

41. Inaba, S.; Sameera, W. M. C. Dehydration of Methanediol ini Aqueous Solution: An ONIOM(QM/MM) Study. *J. Phys. Chem. A* **2016**, *120*, 6670–6676.

42. Chen, L.; Wang, W.; Zhou, L.; Wang, W.; Liu, F.; Li, C.; Lu, J. Role of Water Clusters

in the Reaction of the simplest Criegee Intermediate CH_2OO with Water Vapour. *Theor. Chem. Acc.* **2016**, *135*, 252.

43. Inaba, S. Catalystic Role of H_2O Molecules in Oxidation of CH_3OH in Water. *Catalysts* **2018**, *8*, 157.
44. Wang, L.; Ertem, M. Z.; Murata, K.; Muckerman, J. T.; Fujita, E.; Himeda, Y. Highly Effect and Selective Methanol Production from Paraformaldehyde and Water at Room Temperature. *ACS Catal.* **2018**, *8*, 5233-5239.
45. Wang, L.-P.; Wu, Q.; Voorhis, T. V. Acid-Base Mechanism for Ruthenium Water Oxidation Catalysts. *Inorg. Chem.* **2010**, *49*, 4543−4553.
46. Kelly, C. P.; Cramer, C. J.; Truhlar, D. G. Single-Ion Solvation Free Energies and the Notmal Hydrogen Electrode Potential in Methanol, Acetonitrile, and Dimethyl Sulfoxide. *J. Phys. Chem. B* **2007**, *111*, 408–422.
47. Nørskov, J. K.; Rossmeisl, J.; Logadottir, A.; Lindqdvist, L. Origin of the Overpotential for Oxygen Reduction at a Fuel-Cell Cathode. *J. Phys. Chem. B* **2004**, *108*, 17886–17892.
48. Yang, X.; Baik, M.-H. The Mechanism of Water Oxidation Catalysis Promoted by $[tpyRu(IV)=O]_2L^{3+}$: A Computational Study. J. Am. Chem. Soc. **2008**, *130*, 16231–16240.
49. Hughes, T. F.; Friesner, R. A. Systhematic Investigation of the Catalytic Cycle of a Single Site Ruthenium Oxygen Evolving Complex Using Density Functional Theory. *J. Phys. Chem. B* **2011**, *115*, 9280–9289.
50. Iron, M. A.; Ben-Ari, E.; Cohen, R.; Milstein, D. Metal-Ligand Cooperation in the Trans Addition of Dihydrogen to a Pincer Ir(I) Complex: A DFT Study. *Dalton Trans.*, **2009**, *0*, 9433-9439.
51. Suna, Y.; Ertem, M. Z.; Wang, W.-H.; Kambayashi, H.; Manaka, Y. Muckerman, J. T.; Fujita, E.; Himeda, Y. Positional Effects of Hydroxy Groups on Catalytic Activity of Proton-Responsive Half-Sandwich Cp*Iridium(III) Complexes. *Organometallics*. **2014**, *33*, 6519−6530.
52. Kazaryan, A.; Baerends, E. J. Assessment of Density Functional Methods for Reaction Energetics: Iridium-Catalyzed Water Oxidation as Case Study. *J. Comput. Chem.* **2013**, *34*, 870−878.

53. Huber, K. P.; Herzberg, G. *Molecular Spectra and Molecular Structure: IV. Constants of Diatomic Molecules*; van Nostrand Reinhold: New York, 1979; pp 250.

Chapter 3

Light-Induced Oxidation of Iridium-Aqua Complex to Iridium-Oxo Complex over WO_3(001) Surface

3.1 Introduction

The catalytic reactions of H_2O and CH_4 oxidations by photosystem II (PSII)[1-4] and particulate methane monooxygenase (pMMO) enzymes, respectively, take place under mild conditions. PSII and pMMO have the active sites of Mn–oxo and Cu–oxyl complexes, respectively, where these metal–oxo (M–O) active centers can be formed by visible-light irradiation[1-4] or reduction of O_2 molecule.[5-8,9-12] These two catalysts have inspired the creation of a large number of biomimetic catalysts with similar functionalities and activities.[13-18] A few promising candidates are a half sandwich iridium–oxo complex-based catalysts such as $Cp^*Ir(O)(ppy)^+$ (Cp^* = pentamethyl cyclopentadienyl anion, ppy = 2-phenylpyridine),[19-27] which has high robustness and stability in water solution. However, only metal centers with an oxidation state of no less than 4+ and no more than four *d* electrons can form stable M–O groups as described by Holm in his review.[28] In other words, M–O complexes of the early transition metals (groups 3-6) are stable and common, those of the middle transition metals (groups 7-8) exist and have been often investigated and observed experimentally, but those of the late transition metals (groups 9-11) are unstable and have rarely been observed and isolated. The line separating those of groups 8 and 9 is so-called Oxo-Wall.[29,30] The instability of M–O complexes of groups 9-11 is due to the high electron number in the antibonding metal–oxygen orbitals of the complexes.[28-30] Accordingly, iridium–oxo complexes, which are parts of group 9, can neither be observed nor detected esperimentally despite the high importance of understanding the formation mechanism and the electronic structures of iridium–oxo complexes.

In 2017, Ogo and coworkers reported an iridium–aqua complex $[Ir^{III}(\eta^5\text{-}C_5Me_5)\{bpy(COOH)_2\}(H_2O)]^{2+}$ ($bpy(COOH)_2$ = 2,2'-bipyridine-4,4'-dicarboxylic acid), namely $\mathbf{Ir^{III}–OH_2}$, immobilized over WO_3 surface can catalyze H_2O oxidation through the high-valent iridium–oxo complex $[Ir^{III}(\eta^5\text{-}C_5Me_5)\{bpy(COOH)_2\}(H_2O)]^{2+}$, namely $\mathbf{Ir^{V}=O}$,

although no experimental evidence of its existence is observed so far.[27] Nonetheless, they have hypothesized a mechanism for the formation of this **Ir^{V}=O** (Scheme2-1). As shown in Scheme2-1, **Ir^{V}=O**, reacting with a H_2O molecule to form O–O bond, is formed by visible-light irradiation for WO_3 electrode, i.e. electron excitations from the valence band to the conduction band of WO_3 electrode take place by visible-light irradiation, in which excited electrons move to the cathode electrode and electron holes in WO_3 anode electrode generated by this excitation oxidize the **Ir^{III}–OH_2**, resulting in the deprotonation and formation of the **Ir^{V}=O**. Here, the band gap of the anode is essential for determining the absorbable wavelength range of light. Since WO_3 has a band gap of more than 2.7 eV (equivalent to wavelength of 460 nm),[31-37] it can release two protons even in the visible-light wavelength range to form the **Ir^{V}=O**.

Scheme 3-1. Schematic Representation of Reaction Steps Involved in the Formation of Ir^{V}=O Proposed by Ogo and Coworkers[27]

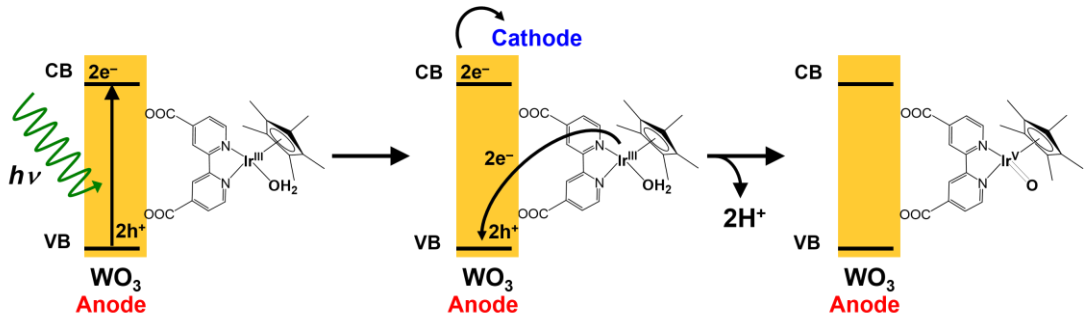

In chapter 2, by performing density functional theory (DFT) calculations, the detail reaction mechanism for the catalytic cycle of H_2O oxidation by **Ir^{V}=O** are discussed, in which the formation of **Ir^{V}=O** from **Ir^{III}–OH_2** and the regeneration of **Ir^{III}–OH_2** from **Ir^{III}–OOH** involving the oxidation of Ir center were investigated by treating it as the electrochemical reaction. In particularly, DFT calculations in Chapter 2 leads us to the conclusions that the formation of **Ir^{V}=O** from **Ir^{III}–OH_2** is the most important step for this catalytic cycle due to the active species for the O–O bond formation by reacting with a H_2O molecule. However, the presence of light irradiation and WO_3 anode support was not considered, which are important for correctly describing the photochemical and supportive effects on the reaction. Thus, it is indispensable to investigate how the energies required for the **Ir^{III}–OH_2** oxidation are influenced by the electron transfer from the Ir atom to the conduction band of WO_3.

In this chapter, by performing DFT and time-dependent DFT (TD-DFT) calculations, the detail reaction mechanisms of the formation of the **Ir^{V}=O** from **Ir^{III}–OH_2** are investigated by considering the effect of WO_3 anode and light irradiation. The present study suggests the electron transfer path of the light-induced oxidation and provides the relationship between the orbital energies of WO_3 anode and the iridium complex. It also demonstrates the minimum required wavelength of light for the formation of the **Ir^{V}=O**.

3.2 Computational methodology

3.2.1 Computational method

A cluster model of the **Ir^{III}–OH_2** supported on a WO_3 cluster surface (after referred to as **{(Ir^{III}–OH_2)/WO_3}**) was used. This approach has been often applied to investigate systems with excited electronic structures such as dye-sensitized solar cells and photoreduction catalysts.[38-41] A full geometry optimization of **{(Ir^{III}–OH_2)/WO_3}** was performed by using the Resolution-of-identity approximation,[42] the B3LYP functional,[43-45] and the def-SVP basis set for all atoms,[46,47] as implemented in the TURBOMOLE 7.2 program package.[48] From this optimization, only the WO_3 surface was used for the partial geometry optimizations of other intermediate structures, where the WO_3 surface was frozen. Then, single-point energy calculations using the TD-DFT[49-50] method were performed on these partially optimized geometries. In this study 350 excitations are analyzed which includes wavelength of more than 350 nm in **{(Ir^{III}–OH_2)/WO_3}** and **{(Ir^{III}–OH)$^{-1}$/WO_3}$^{-1}$** and 395 nm in **{(Ir^{IV}–OH)/WO_3}** and **{(Ir^{IV}=O)$^{-1}$/WO_3}$^{-1}$**, by performing TD-DFT calculations. Oscillator strength was broadened by a Lorentzian function with a width of 20 nm. Because the high humidity in the real operation conditions of fuel cells results in water vapor around the WO_3 anode and iridium complex, implicit sol-vent effects of H_2O (dielectric constant = 78.39) were considered by performing single-point calculations using the COSMO.[51] The energy of H^+ $E(H^+)$ is calculated by the following equation.

$$E(\mathrm{H}^+) = E(\mathrm{H}^+(\mathrm{H_2O})_4) - E((\mathrm{H_2O})_4) \qquad (3-1)$$

Where $E(H^+(H_2O)_4)$ and $E((H_2O)_4)$ are the energies of $H^+(H_2O)_4$ and $(H_2O)_4$ clusters, respectively. The $H^+(H_2O)_4$ cluster is a more reasonable and widely acceptable model[52-55] of H^+ in water solution (Figure 2-2).[53]The electron density difference maps (EDDMs) between the excited (ρ_e) and ground states (ρ_g) obtained from the TD-DFT calculations were visualized by using GaussSum3.0 programs.[56]

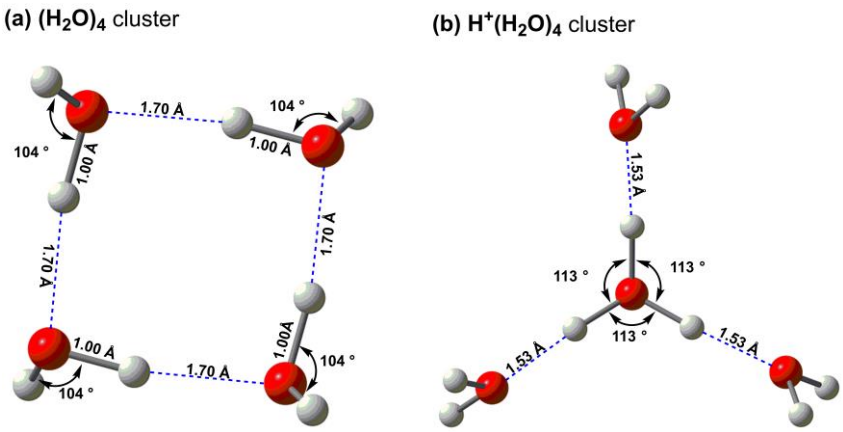

Figure 3-1. The Optimized geometries of (a) $(H_2O)_4$ cluster and (b) $H^+(H_2O)_4$ cluster models. Units are in Å and degree.

2.2.2 Computational model

The WO_3 surface was modeled by arranging 40 units of WO_3 into two layers (6.0 Å) of monoclinic (001) surface, which has a dimension of 14.6 Å × 19.5 Å, equivalent to a 4 × 5 slab model. This model satisfies the three principles of cluster models proposed by Nakatsuji and co-wokers.,[57-59] that is, charge neutrality, stoichiometry balance, and good coordination without dangling bonds. Figure 3-2 shows the optimized structure of a bare $(WO_3)_{40}$ cluster and its highest occupied molecular orbital (HOMO), HOMO–2, lowest unoccupied molecular orbital (LUMO). The HOMO in the $(WO_3)_{40}$ is assumed to be equivalent to the edge of the WO_3 valence band, because it is localized at the edge O atoms of the WO_3(001) surface.[60] Such an MO localization in cluster border was also reported in previous theoretical cluster-modeled calculations.[38,39,41] The LUMO in the $(WO_3)_{40}$, on the other hand, is evenly distributed on the W 5*d* orbitals. The HOMO–LUMO gap in the $(WO_3)_{40}$ is calculated to be 2.89 eV, which is consistent with the experimentally measured band gap of 2.7~3.2 eV,[31-37] as well as with the previous theoretical studies at the B3LYP/Hay-Wadt double-ζ basis set(W)+8-411(d1)(O) level of theory (3.13 eV and 2.75 eV corresponding to a bulk structure and a slab model, respectively).[61,62] Although an average bond length of W–O bridge in inner surface calculated to be 2.16 Å, which is little elongated compared with bulk structure,[63] this elongation is often found in previous reports of WO_3 surface.[62,64,65] Therefore, this model is enough to describe WO_3 with chemical and electronic properties. Moreover, Figure 3-3 shows the optimized structure of **{(Ir^{III}–OH_2)/WO_3}** model and its HOMO, HOMO–2, and LUMO. HOMO in

{(Ir^{III}–OH$_2$)/WO$_3$} is localized in the carboxyl group in **Ir^{III}–OH$_2$**. HOMO–2 corresponds to the edge of the WO_3 valence band. As with LUMO in $(WO_3)_{40}$, LUMO in **{(Ir^{III}–OH$_2$)/WO$_3$}** is also distributed on the W 5*d* orbitals, which is assigned to LUMO of WO_3 surface. The HOMO–LUMO gap in the $(WO_3)_{40}$ in **{(Ir^{III}–OH$_2$)/WO$_3$}** is calculated to be 2.87 eV, which is consistent with that value in the $(WO_3)_{40}$. This indicates that the Ir complex induces insignificant change of the electronic structures in $(WO_3)_{40}$.

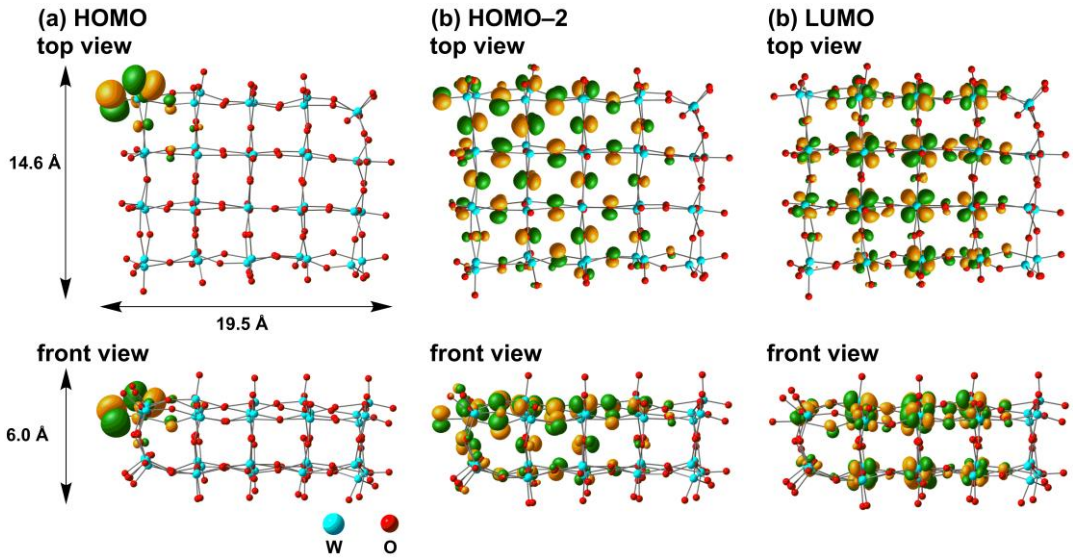

Figure 3-2. (a) Optimized structure of a bare $(WO_3)_{40}$ cluster surface and its (a) highest occupied molecular orbital (HOMO), (b) HOMO–2, and (c) lowest unoccupied molecular orbital (LUMO) (isovalue = 0.025).

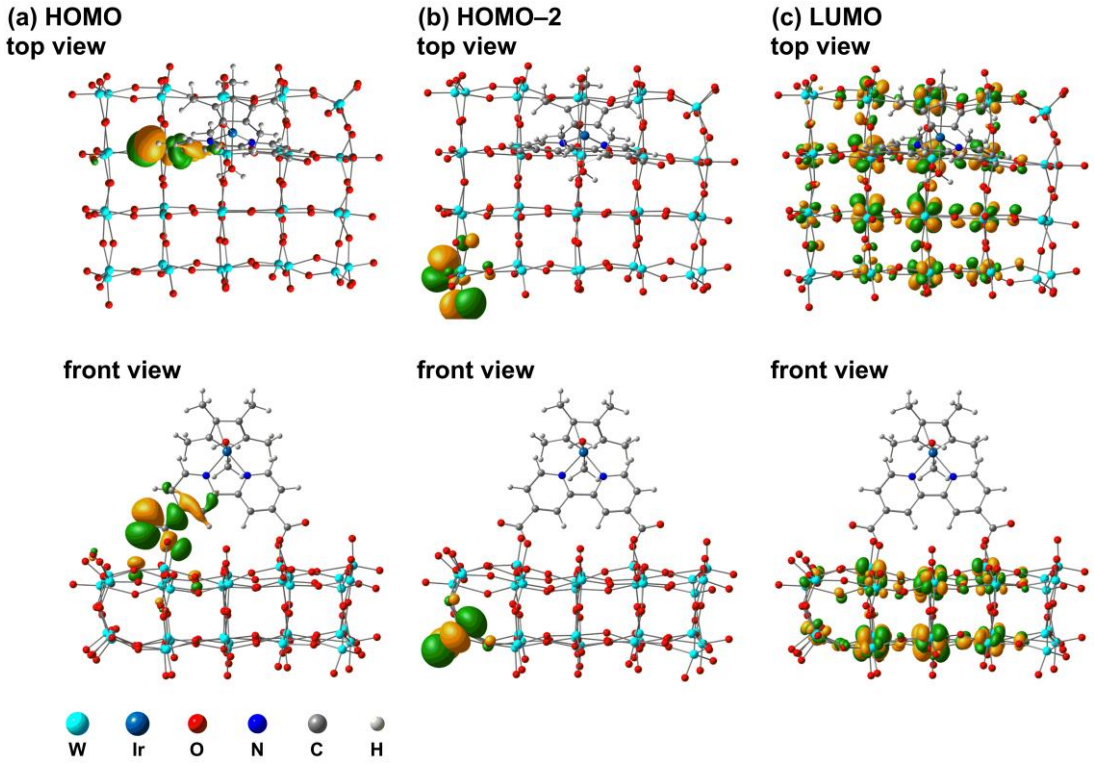

Figure 3-3. (a) Optimized structure of a **{(Ir^{III}–OH_2)/WO_3}** and its (a) HOMO, (b) HOMO–2, and (c) LUMO (isovalue = 0.025).

3.3 Results and discussion

3.3.1 Reaction step of $\{(Ir^{III}–OH_2)/WO_3\} \rightarrow \{(Ir^{V}=O)/WO_3\} + 2H^+ + 2e^–$

As shown in Scheme 3-2 (blue solid arrows), the formation of **$\{(Ir^{V}=O)/WO_3\}$** from **$\{(Ir^{III}–OH_2)/WO_3\}$** consists of four reaction steps: two deprotonation reactions of **$\{(Ir^{III}–OH_2)/WO_3\} \rightarrow \{(Ir^{III}–OH)^{-1}/WO_3\}^{-1}$** and **$\{(Ir^{IV}–OH)/WO_3\} \rightarrow \{(Ir^{IV}–O)^{-1}/WO_3\}^{-1}$** and two light-induced oxidation reactions of **$\{(Ir^{III}–OH)^{-1}/WO_3\}^{-1} \rightarrow \{(Ir^{IV}–OH)/WO_3\}$** and **$\{(Ir^{IV}–O)^{-1}/WO_3\}^{-1} \rightarrow \{(Ir^{V}=O)/WO_3\}$**. This reaction step is consistent with the computational result with respect to the formation of **$Ir^{V}=O$** from **$Ir^{III}–OH_2$** in Chapter 2. At first, one H atom of the aqua ligand in **$\{(Ir^{III}–OH_2)/WO_3\}$** is released to form **$\{(Ir^{III}–OH)^{-1}/WO_3\}^{-1}$** with a deprotonation energy of 14.0 kcal/mol, which is 0.7 kcal/mol lower than that without the support of WO_3 anode model in Chapter 2. Calculated spin populations in Ir and O in **$\{(Ir^{III}–OH)^{-1}/WO_3\}^{-1}$** are 0.51 and 0.36 $e^–/Å^3$, respectively, which is consistent with the that of 0.55 and 0.31 in Chapter 2. Subsequently, a light-induced oxidation reaction from **$\{(Ir^{III}–OH)^{-1}/WO_3\}^{-1}$** to **$\{(Ir^{IV}–OH)/WO_3\}$** takes place by visible-light at least the wavelength of 524 nm. Next, the deprotonation of the $OH^–$ ligand in **$\{(Ir^{IV}–OH)/WO_3\}$** occurs to form **$\{(Ir^{IV}–O)^{-1}/WO_3\}^{-1}$** with a reasonable deprotonation energy of 14.4 kcal/mol, which is by 7.6 kcal/mol lower than that without the support of WO_3 anode model in Chapter 2. Calculated spin population in Ir and O in **$\{(Ir^{IV}–OH)^{-1}/WO_3\}^{-1}$** (0.86 and 0.13 $e^–/Å^3$) is also consistent with the that in Chapter 2 (0.78 and 0.21). Since Ir^{IV} is a rather unstable oxidation state,[30] the formed **$\{(Ir^{IV}–O)^{-1}/WO_3\}^{-1}$** is immediately oxidized to form **$\{(Ir^{V}=O)/WO_3\}$** by visible-light at least the wavelength of 504 nm.

Scheme 3-2. Square Scheme of Reaction: {(Ir^{III}–OH_2)/WO_3} → {(Ir^{V}=O)/WO_3} + $2H^+$ + $2e^-$.

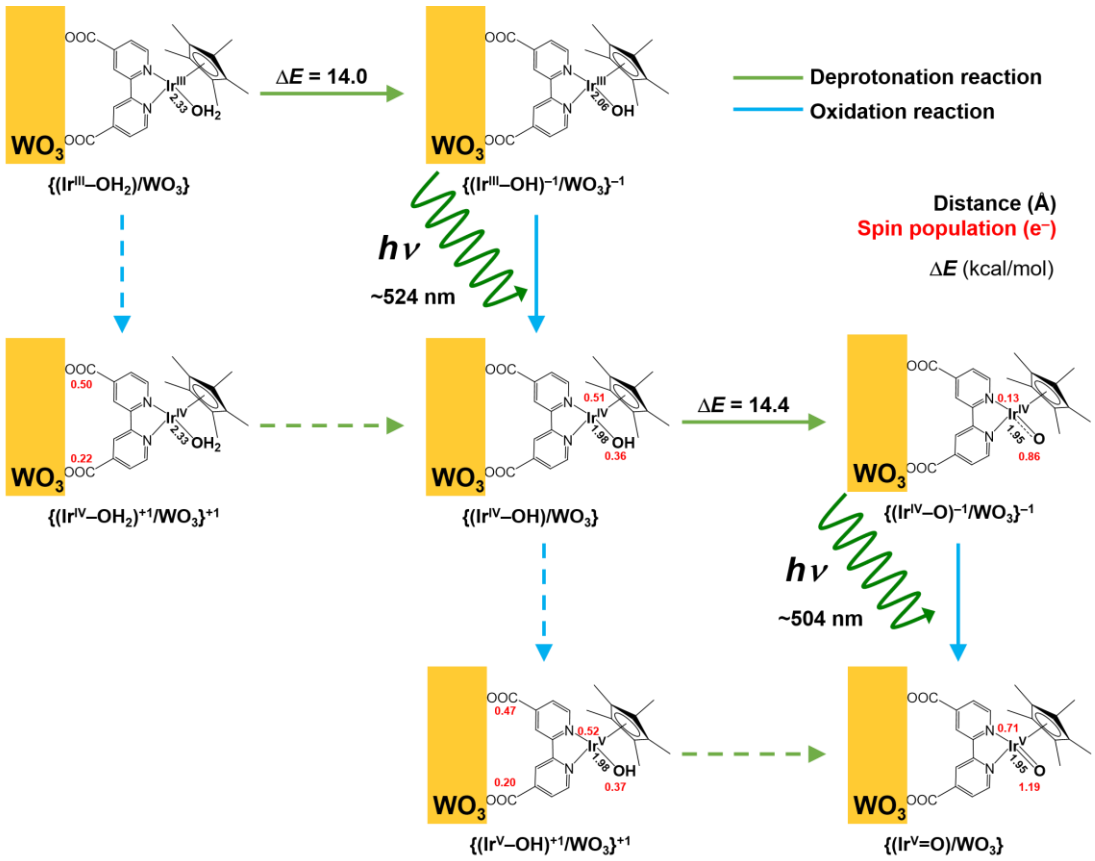

3.3.2 TDDFT analysis

To investigate the effect of visible-light excitations on the formation of **{(Ir^{V}=O)/WO_3}** from **{(Ir^{III}–OH_2)/WO_3}**, TD-DFT calculations were performed. First, we look at the formation of **{(Ir^{IV}–OH)/WO_3}** from **{(Ir^{III}–OH_2)/WO_3}**. Figure 3-4(a) and (d) show calculated oscillator strengths of **{(Ir^{III}–OH_2)/WO_3}** and **{(Ir^{III}–OH)$^{-1}$/WO_3}$^{-1}$**, respectively (black bars). The calculated spectrum of **{(Ir^{III}–OH_2)/WO_3}** is similar to that of $(WO_3)_{40}$ cluster (red line). In addition, there is no excitation corresponding to the electron transfer from the Ir atom to $(WO_3)_{40}$ cluster in the visible range (> 400 nm). In **{(Ir^{III}–OH)$^{-1}$/WO_3}$^{-1}$**, on the other hand, the lowest excitation with a sizable oscillator strength (> 0.00250) is the 39th (S0 → S39) excited state, which is calculated at the wavelength of 524 nm with an oscillator strength of 0.00979. The largest MO contribution for this excitation state is the electron transfer from the HOMO to the LUMO+17 (Figure 3-4(d)), the ratio of which is calculated to be 18.4 % (the lists of relative MO contribution of sizable electron excitations in

{(Ir^{III}–OH)$^{-1}$/WO$_3$}$^{-1}$ are shown in Table 3-3). This excitation corresponds to the electron transfer from the occupied π* orbital of the Ir^{III}–OH part to the W 5*d* orbitals, which are equivalent to the conduction band of the WO$_3$ surface. Additionally, EDDM corresponding to this excitation (Figure 3-4(c)) indicates the localization of an electron hole (red region) in the Ir^{III}–OH part following the light adsorption.

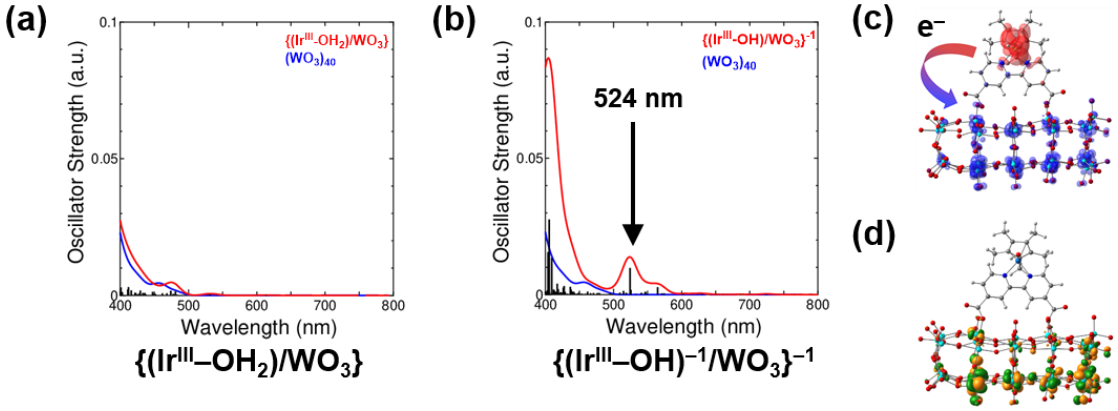

Figure 3-4. Calculated oscillator strengths of (a) **{(Ir^{III}–OH$_2$)/WO$_3$}** and (b) **{(Ir^{III}–OH)$^{-1}$/WO$_3$}$^{-1}$** (black bars), and their broadened values (red curves). Blue curves are the broadened oscillator strengths of the (WO$_3$)$_{40}$ only. (c) EDDM of **{(Ir^{III}–OH)$^{-1}$/WO$_3$}$^{-1}$** at the wavelengths of 524 nm, where the red and blue isosurfaces respectively indicate the decrease and increase of electron density upon electron excitation (isovalue = 0.0005) (d) The LUMO+17 of **{(Ir^{III}–OH)$^{-1}$/WO$_3$}$^{-1}$** (isovalue = 0.025).

Moreover, there is a sizable excitation (the 290th electron) with an oscillator strength of 0.0106 in the UV-light range corresponding to 3.48 eV (equivalent to wavelength 356 nm). From the observation of the largest MO contribution (Table 3-2), large components (sum of 32.6 %) of this excitation is derived from various occupied orbitals corresponding to the valence band of WO$_3$ surface with arriving at LUMO and LUMO+3 corresponding to the conduction bands of the WO$_3$ surface. Figure 3-5 (b) shows the EDDM of this sizable excitation, where the electron density decrease region (red isosurface) is localized at the O atoms. This indicates that an electron hole generated on the WO$_3$ surface, leading to the oxidation of Ir^{III}–OH complex to form **{(Ir^{IV}–OH)/WO$_3$}**. This analysis is fully consistent with the mechanism proposed by Ogo and co-workers (Scheme 3-1).[27]

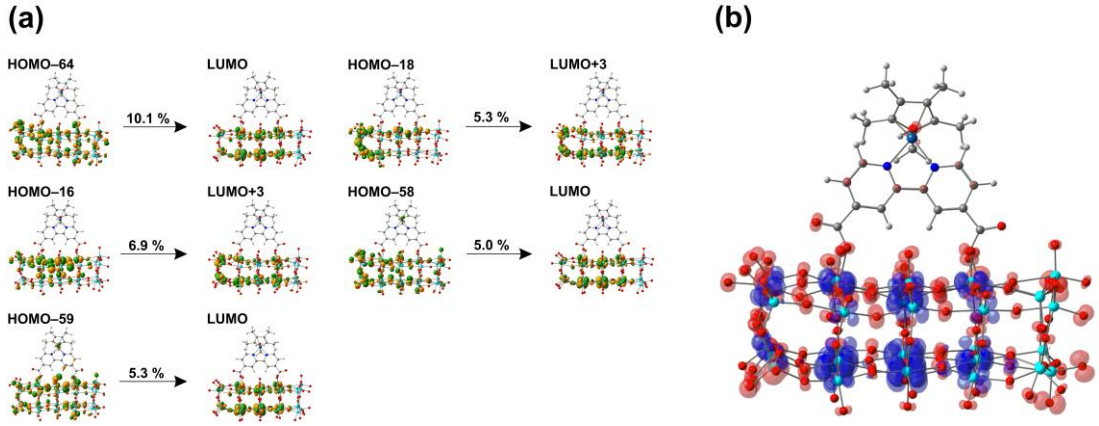

Figure 3-5. Relatively large MO changes at the 290th excitation (isovalue = 0.025). (b) Electron density differential map (EDDM) of **{(Ir^{III}–OH)$^{-1}$/WO$_3$}$^{-1}$** at the 290th excitation, where the red and blue isosurfaces (isovalue = 0.0005) respectively indicates the decrease and increase of electron density upon electron excitation.

We next discuss about the formation of **{(Ir^{V}=O)/WO$_3$}** from **{(Ir^{IV}–OH)/WO$_3$}**. Figure 3-6(a) and (d) show calculated oscillator strengths of **{(Ir^{IV}–OH)/WO$_3$}** and **{(Ir^{IV}–O)$^{-1}$/WO$_3$}$^{-1}$**, respectively (black bars). In **{(Ir^{IV}–OH)/WO$_3$}** these are some excitations with the relative strong oscillator strengths (~0.01) around 500 and 400 nm. As shown in Figure 3-7, EDDMs of these excitations shows the electron transfer from O atoms in WO_3 surface to the Ir atom corresponding to the reduction of the Ir atom from $Ir^{IV} \rightarrow Ir^{III}$. On the other hand, the strongest excitation of **{(Ir^{IV}=O)/WO$_3$}**$^{-1}$ in the visible-light range is the 99th excited state at the wavelength of 504 nm (see Figure 3-6(b)) with a calculated oscillator strength of 0.0213. As shown in Table 3-5, the largest contribution of this excitation state is the electron transfer from the HOMO(β) corresponding to the π* orbital between Ir and O atoms (π*(Ir–O)(β)) to the LUMO+57(β) (shown in Figure 3-6(d)). The EDDM of this excitation (Figure 3-6(c)) indicates the electron transfer from the occupied π* orbital of Ir^{IV}–O$^{\bullet}$ part to WO_3 surface, corresponding to the formation of an electron hole in the Ir^{IV}–O$^{\bullet}$ part. This supports the high possibility of the light-induced oxidation reaction of **{(Ir^{IV}=O)/WO$_3$}$^{-1}$** $\rightarrow$ **{(Ir^{V}=O)/WO$_3$}** in the visible-light range.

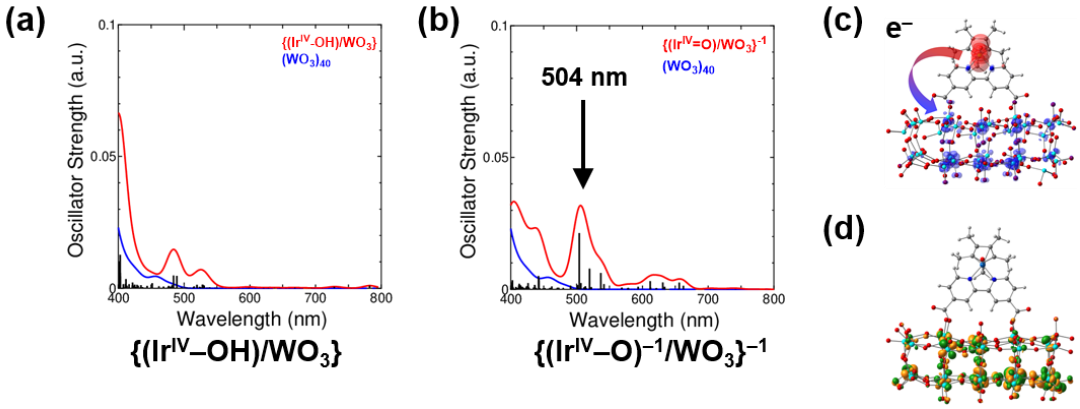

Figure 3-6. Calculated oscillator strengths of (a) **{(Ir^{IV}–OH)/WO$_3$}** and (b) **{(Ir^{IV}–O)$^{-1}$/WO$_3$}$^{-1}$** (black bars), and their broadened values (red curves). Blue curves are the broadened oscillator strengths of the $(WO_3)_{40}$ only. (c) Electron density differential map (EDDM) of **{(Ir^{IV}–O)$^{-1}$/WO$_3$}$^{-1}$** at the wavelengths of 524 nm, where the red and blue isosurfaces respectively indicate the decrease and increase of electron density upon electron excitation (isovalue = 0.0005). (d) The LUMO+17 of **{(Ir^{IV}–O)$^{-1}$/WO$_3$}$^{-1}$** (isovalue = 0.025).

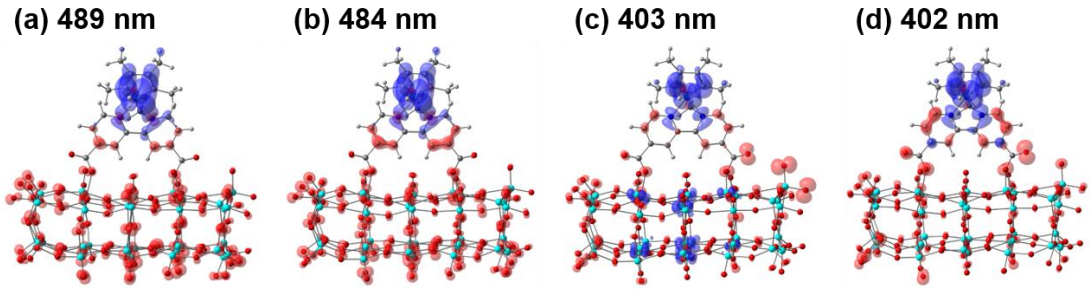

Figure 3-7. Electron density differential map (EDDM) of **{(Ir^{IV}–OH) /WO$_3$}** at the wavelengths of (a) 489, (b) 484, (c) 403, and (d) 402 nm, where the red and blue isosurfaces respectively indicate the decrease and increase of electron density upon electron excitation (isovalue = 0.0005).

3.3.3 Molecular orbital analysis

To investigate why the excitation corresponding to the electron transfer from the Ir atom to W 5*d* orbital in **{(Ir^{III}–OH)$^{-1}$/WO$_3$}$^{-1}$** in the visible range, the molecular orbital analysis are performed. As shown in Figure 3-8, the HOMO–LUMO gaps of the WO_3 surface before and after the presence of the Ir complexes (2.8~2.9 eV) are found to be similar, suggesting that the Ir complexes insignificantly change the WO_3 electronic structures. In **{(Ir^{III}–OH$_2$)/WO$_3$}**, there is no MO mainly coming from the Ir 5*d* orbitals between HOMO–2 and LUMO (green lines), which are respectively assigned to the HOMO and LUMO of the WO_3 surface (*w*HOMO and *w*LUMO, respectively). As indicated by a blue line for **{(Ir^{III}–OH$_2$)/WO$_3$}**, the HOMO–42, where the Ir 5*d* orbitals plays principal role, lies 0.99 eV below the *w*HOMO. The energy gap between the HOMO–42 and *w*LUMO is calculated to be 3.86 eV, indicating that the light-induced oxidation of **{(Ir^{III}–OH$_2$)/WO$_3$}** forming **{(Ir^{IV}–OH$_2$)$^{+1}$/WO$_3$}$^{+1}$** in the visible-light range is unfavorable. In contrast, after the first deprotonation forming **{(Ir^{III}–OH)$^{-1}$/WO$_3$}$^{-1}$**, the HOMO (i.e. π*(Ir–O)) is positioned in between the *w*HOMO and *w*LUMO (2.05 eV above the *w*HOMO). Such a change of electronic structure along the **{(Ir^{III}–OH$_2$)/WO$_3$}** → **{(Ir^{III}–OH)$^{-1}$/WO$_3$}$^{-1}$** reaction indicates that the deprotonation of the aqua ligand induces the hybridization between Ir 5*d* and O 2*p* orbitals and increases MO energies with respect to the Ir 5*d* orbitals. Thus, this suggests the trigger of the light-induced oxidation of **{(Ir^{III}–OH)/WO$_3$}$^{-1}$** to **{(Ir^{IV}–OH)/WO$_3$}**. After the formation of **{(Ir^{IV}–OH)/WO$_3$}**, the HOMO –118(α) corresponding to the π*(Ir–O)(α), lies below the *w*HOMO. Interestingly, the LUMO(β) is positioned in between the *w*HOMO and *w*LUMO and similar to the HOMO (i.e. π*(Ir–O)) of **{(Ir^{III}–OH)$^{-1}$/WO$_3$}$^{-1}$**, suggesting that an electron transfer occurs from the π*(Ir–O) of **{(Ir^{III}–OH)$^{-1}$/WO$_3$}$^{-1}$**. After deprotonation of **{(Ir^{IV}–OH)/WO$_3$}**, the HOMO(β) in **{(Ir^{IV}=O)$^{-1}$/WO$_3$}$^{-1}$**, which corresponds to π*(Ir–O)(β), is again positioned in between the *w*HOMO and *w*LUMO and is similar to the HOMO–211(β). This is because the deprotonation of the OH ligand increases MO energies with respect to the Ir 5*d* orbitals. In **{(Ir^{V}=O)/WO$_3$}** LUMO(β) and LUMO+1(β) is positioned in between *w*HOMO and *w*LUMO, both of which are spatially orthogonal to each other. Additionally, LUMO(β) is similar to the HOMO(β) (i.e. π*(Ir–O)) of **{(Ir^{IV}=O)$^{-1}$/WO$_3$}$^{-1}$**, suggesting that an electron transfer occurs from the π*(Ir–O) of **{(Ir^{IV}=O)$^{-1}$/WO$_3$}$^{-1}$**.

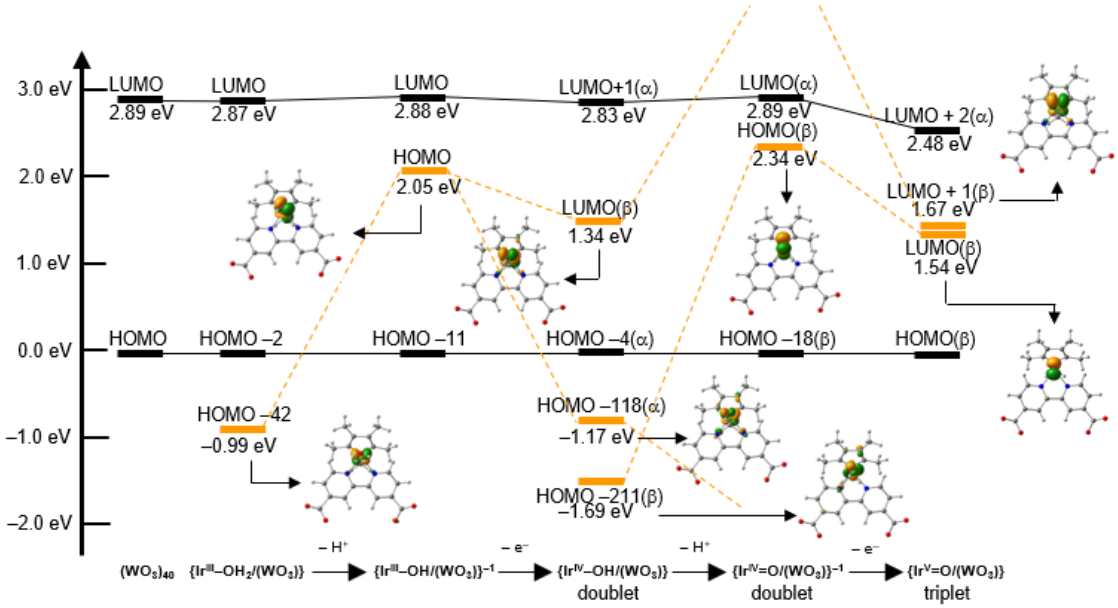

Figure 3-8. Calculated orbital energies of the **{(Ir^{III}–OH$_2$)/WO$_3$}**, **{(Ir^{III}–OH)$^{-1}$/WO$_3$}$^{-1}$**, **{(Ir^{IV}–OH)/WO$_3$}**, **{(Ir^{IV}=O)$^{-1}$/WO$_3$}$^{-1}$** and **{(Ir^{V}=O)/WO$_3$}**. Relative energies are measured from the HOMO of WO_3 surface in each system. Black and yellow lines indicate the MO mainly coming from orbitals of the WO_3 surface and the Ir 5*d*, respectively. The WO_3 surface moiety is omitted for clarity and insignificantly contribution in MO related to Ir 5*d*.

3.3.4 Mechanism of the light-induced oxidation

Above discussions suggest that the light-induced oxidation of the Ir atom forming the **Ir^{IV}=O** may proceed through two possible paths: visible and UV-light excitation paths. In the visible-light excitation, as shown in Figure 3-9 (a), electrons are transferred from the occupied π^* orbitals of Ir^{III}–OH or Ir^{IV}–O$^{\bullet}$ to the WO_3 conduction band. For this case, the adsorption wavelength depends on the lowest energy of the WO_3 conduction band rather than on the WO_3 band gap. Thus, other semiconductor surfaces with a lower conduction band energy such as SnO_2 surface[66] are predicted to form the **Ir^{IV}=O** under longer wavelength of light irradiation, although SnO_2 has a large band gap of 3.59 eV (Figure 3-9 (c)).[66-70] In the UV-light excitation (Figure 3-9 (b)), on the other hand, electrons are first excited from the valence band to the conduction band of the WO_3 surface induced by the UV-light irradiation and subsequently the resultant electron hole oxidizes the Ir complex. This mechanism is proposed by Ogo and coworkers.[27]

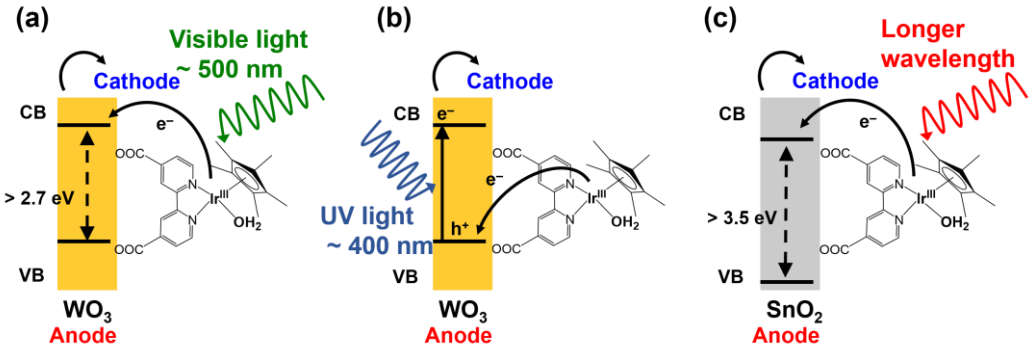

Figure 3-9. Schematic representation of the light-induced oxidation through (a) visible-light excitation mechanism, (b) UV-light excitation mechanism, and (c) prediction system.

3.4 Conclusions

In this chapter the mechanism for the formation of the iridium–oxo complex $[Ir^{V}(\eta^5\text{-}C_5Me_5)\{bpy(COOH)_2\}(O)]^{2+}$ (**Ir^{V}=O**) from iridium–aqua complex $[Ir^{III}(\eta^5\text{-}C_5Me_5)\{bpy(COOH)_2\}(H_2O)]^{2+}$ (**Ir^{III}–OH_2**) considered the effect of WO_3(001) anode and light irradiation were investigated by using DFT and time-dependent DFT (TD-DFT) calculations. DFT calculations shows the plausible reaction pathway of the formation of **Ir^{V}=O** from **Ir^{III}–OH_2** (**{(Ir^{III}–OH_2)/WO_3}** → **{(Ir^{III}–OH)$^{-1}$/WO_3}$^{-1}$** → **{(Ir^{IV}–OH)/WO_3}** → **{(Ir^{IV}–O)$^{-1}$/WO_3}$^{-1}$** → **{(Ir^{V}=O)/WO_3}**), which is consistent with the computational results in Chapter 2. Calculated deprotonation energies of the aqua or hydroxyl ligand are respectively 14.0 and 14.4 kcal/mol, both of which is lower than without WO_3(001) surface model in Chapter 2. From the calculated oscillator strengths, we found two distinct mechanisms for the light-induced oxidation of the Ir complex to the Ir-oxo complex, namely the visible-light and UV-light excitation mechanisms. In the visible-light excitation mechanism, the light-induced oxidation of the Ir complex takes place by the electron transfer directly from the occupied π* orbitals of Ir^{III}–OH or Ir^{IV}–O$^{\bullet}$ to the WO_3 conduction band in the visible-light range, where the energy level of the anode's conduction band determines the adsorption wavelength. In the UV-light excitation mechanism, on the contrary, the Ir complex is oxidized by the electron hole generated by the electron excitation in the WO_3 surface due to the UV light irradiation. By performing molecular orbital analysis we demonstrated that the deprotonation reactions play essential roles in activating the Ir 5*d* orbitals, which enable the visible-light excitation from Ir 5*d* orbitals to W 5*d* orbitals

Reference

1. McEvoy, J. P.; Brudvig, G. W. Water-Splitting Chemistry of Photosystem II. *Chem. Rev.* **2006**, *106*, 4455−4483.

2. Umena, Y.; Kawakami, K.; Shen, J.-R.; Kamiya, N. Crystal Structure of Oxygen-Evolving Photosystem II at a Resolution of 1.9 Å. *Nature* **2011**, *473*, 55−60.

3. Cox, N.; Pantazis, D. A.; Neese, F.; Lubitz, W. Biological Water Oxidation. *Acc. Chem. Res.* **2013**, *46*, 1588−1596.

4. Yano, J.; Yachandra, V. Mn_4Ca Cluster in Photosynthesis: Where and How Water Is Oxidized to Dioxygen. *Chem. Rev.* **2014**, *114*, 4175−4205.

5. Lieberman, R. L.; Rosenzweig, A. C. Crystal Structure of a Membrane-Bound Metalloenzyme That Catalyses the Biological Oxidation of Methane. *Nature* **2005**, *434*, 177–182.

6. Solomon, E. I.; Heppner, D. E.; Johnston. E. M.; Ginsbach, J. W. Cirera, J. Qayyum, M.; Kieber-Emmons, M. T.; Kjaergaard, C. H.; Hadt, R. G.; Tian, L. Copper Active Sites in Biology. *Chem. Rev*. **2014**, *114*, 3659−3853.

7. Wang, V. C.-C.; Maji, S.; Chen, P. P.-Y.; Lee, H. K.; Yu, S. S.-F.; Chan, S. I. Alkane Oxidation: Methane Monooxygenases, Related Enzyme, and Their Biomimetics. *Chem. Rev.* **2017**, *117*, 8574–8621.

8. Cao, L.; Caldararu, O.; Rosenzweig, A. C.; Ryde, U. Quantum Refinement Dose Not Support Dinuclear Copper in Crystal Structures of Particulate Methane Monooxygenase. *Angew. Chem., Int. Ed*. **2018**, *57*, 162−166.

9. Culpepper, M. A., Cutsail III, G. E.; Hoffman, M.; Rosenzweig, A. C. Evidence for Oxygen Binding at the Active Site of Particulate Methane Monooxygenase. *J. Am. Chem. Soc.* **2012**, *134*, 7640–7643.

10. Culpepper, M. A.; Cutsail III, G. E.; Gunderson, W. A.; Hoffman, B. M.; Rosenzweig, A. C. Identification of the Valence and Coordination Environment of the Particulate

Methane Monooxygenase Copper Centers by Advanced EPR Characterization. *J. Am. Chem. Soc.* **2014**, *136*, 11767–11775. 2001, 40, 2782–2807.

11. Yoshizawa, K.; Suzuki, A.; Shiota, Y.; Yamabe, T. Conversion of Methane to Methanol on Diiron and Dicopper Enzyme Models of Methane Monooxygenase: A Theoretical Study on a Concerted Reaction Pathway. *Bul. Chem. Soc. Jpn.* **2000**, *73*, 815–827.

12. Yoshizawa, K.; Shiota Y. Conversion of Methane to Methanol at the Mononuclear and Dinuclear Copper Sites of Particulate Methane Monooxygenase (pMMO): A DFT and QM/MM Study. *J. Am. Chem. Soc.* **2006**, *128*, 9873–9881.

13. Cady, C. W.; Crabtree, R. H.; Brudvig, G. W. Functional Models for the Oxygen-Evolving Complex of Photosystem II. *Coord. Chem. Rev.* **2008**, *252*, 444−455.

14. Kärkäs, M. D.; Verho, O.; Johnston, E. V.; Åkermark, B. Artificial Photosynthesis: Molecular Systems for Catalytic Water Oxidation. *Chem. Rev.* **2014**, *114*, 11863−12001.

15. Blakemore, J. D.; Crabtree, R. H.; Brudvig, G. W. Molecular Catalysts for Water Oxidation. *Chem. Rev.* **2015**, *115*, 12974−13005.

16. Wang, V. C.-C.; Maji, S.; Chen, P. P.-Y.; Lee, H. K.; Yu, S. S.-F. Chan, S. I. Alkane Oxidation: Methane Monooxygenase, Related Enzymes, and Their Biomimetics. *Chem. Rev*. **2017** *117*, 8574−8621.

17. Mahyuddin, M. H.; Shiota, Y.; Staykov, A.; Yoshizawa, K. Theoretical Overview of Methane Hydroxylation by Copper-Oxygen Species in Enzymatic and Zeolitic Catalysts. *Acc. Chem. Res*. **2018**, *51*, 2382–2390.

18. Mahyuddin, M. H.; Shiota, Y.; Yoshizawa, K. Methane Selective Oxidation to Methanol by Metal-Exchanged Zeolites: A Review of Active Sites and Their Reactivity. *Catal. Sci. Technol*. **2019**, *9*, 1744–1768.

19. Hull, J. F.; Balcells, D.; Blakemore, J. D.; Incarvito, C. D.; Eisenstein, O.; Brudvig, G. W.; Crabtree, R. H. Highly Active and Robust Cp* Iridium Complexes for Catalytic Water Oxidation. *J. Am. Chem. Soc*. **2009**, *131*, 8730−8731.

20. Blakemore, J. D.; Schley, N. D.; Balcells, D.; Hull, J. F.; Olack, G. W.; Incarvito, C. D.; Eisenstein, O.; Brudvig, G. W.; Crabtree, R. H. Half-Sandwich Iridium Complexes for Homogeneous Water-Oxidation Catalysis. *J. Am. Chem. Soc*. **2010**, *132*, 16017−16029.

21. Grotjahn, D. B.; Brown, D. B.; Martin, J. K.; Marelius, D. C.; Abadjian, M. C.; Tran, H. N.; Kalyuzhny, G.; Vecchio, K. S.; Specht, Z. G.; Cortes-Llamas, S. A.; Miranda-Soto, V.; van Niekerk, C.; Moore, C. E.; Rheingold, A. L. Evolution of Iridium-Based Molecular Catalysts during Water Oxidation with Ceric Ammonium Nitrate. *J. Am. Chem. Soc.* **2011**, *133*, 19024-19027.

22. Vilella, L.; Vidossich, P.; Balcells, D.; Lled**ó**s, A. Basic Ancillary Ligands Promote O–O Bond Formation in Iridium-Catalyzed Water Oxidation: A DFT study. *Dalton Trans.*, **2011**, *40*, 11241−11247.

23. Zhou, M.; Balcells, D.; Parent, A. R.; Crabtree, R. H.; Eisenstein, O. Cp* iridium Precatalysts for Selective C–H Oxidation via Direct Oxygen Insertion: A Joint Experimental/Computational Study. *ACS. Catal*. **2012**, *2*, 208−218.

24. Joya, K. S.; Subbaiyan, N. K.; D'Souza, F.; de Groot, H. J. M. Surface-Immobilized Single-Site Iridium Complexes for Electrocatalytic Water Splitting. *Angew. Chem., Int. Ed.* **2012**, *51*, 9601−9605.

25. Zhang, T.; deKrafft, K. E.; Wang, J.-L.; Wang, C.; Lin, W. The Effects of Electron-Donating Substituents on $[Ir(bpy)Cp^*Cl]^+$: Water Oxidation versus Ligand Oxidative Modifications. *Eur. J. Inorg. Chem.* **2014**, *4*, 698-707.

26. Thomsen, J. M.; Huang, D. L.; Crabtree, R. H. Brudvig, G. W. Iridium-Based Complexes for Water Oxidation. *Dalton Trans.*, **2015**, *44*, 12452−12472.

27. Kikkawa, M.; Yatabe, T.; Matsumoto, T.; Yoon, K.-S.; Suzuki, K.; Enomoto, T.; Kaneko, K.; Ogo, S. A Fusion of Biomimetic Fuel and Solar Cells Based on Hydrogenase, Photosystem II, and Cytochrome c Oxidase. *ChemCatChem* **2017**, *9*, 4024−4028.

28. Holm, R. H.; Metal-Centered Oxygen Atom Transfer Reactions. *Chem. Rev*. **1987** *87*, 1401−1449.

29. Winlker, J. R.; Gray. H. B. Electronic Structures of Oxo—Metal Ions. Struc. Bond. Structure and Bonding. **2012**. *142*, 17–28.

30. O'Halloran, K. P.; Zhao, C. C.; Ando, N. S.; Schultz, A. J.; Koetzle, T. F.; Piccoli, P. M. B.; Hedman, B.; Hodgson, K. O.; Bobyr, E.; Kirk, M. L.; Knottenbelt, S.; Depperman, E. C.; Stein, B.; Anderson, T. M.; Cao, R.; Geletii, Y. V.; Hardcastle, K. I.; Musaev, D. G.; Neiwert, W. A.; Fang, X. K.; Morokuma, K.; Wu, S. X.; Kogerler, P.; Hill, C. L. Revisiting the Polyoxometalate-Based Late-Transition-Metal-Oxo Complexes: The ″Oxo Wall″ Stands. *Inorg. Chem*. **2012**, *51*, 7025–7031

31. Bange, K. Colouration of Tungsten Oxide Films: A model for Optically Active Coatings. *Sol. Energy Mater. Sol. Cells* **1999**, *58*,1–131.

32. Bamwenda, R. G.; Sayama, K.; Arakawa, H. The Effect of Selected Reaction Parameters on the Photoproduction of Oxygen and Hydrogen Form a WO_3-Fe_2^+–Fe_3^+ Aqueous Suspension. *J. Photochem. Photobiol. A* **1999**, *122*, 175.

33. Granqvist, C. G. Electronic Tungsten Oxide Films: Review of Progress 1993–1998. *Sol. Energy Mater. Sol. Cells* **2000**, *60*, 201–262.

34. Gesheva, K.; Szekeres, A.; Ivanova, T. Optical Properties of Chemical Vapor Deposited Thin Films of Molybdenum and Tungsten Based Metal Oxides. *Sol. Energy Mater. Sol. Cells* **2003**, *76*, 563–576.

35. Marsen, B.; Cole, B.; Miller, E. L. Influence of Sputter Oxygen Partial Pressure in Photoelectrochemical Performance of Tungsten Oxide Films. *Sol. Energy Mater. Sol. Cells* **2007**, *91*, 1954.

36. Kharade, R. R.; Mane, S. R.; Mane, R. M.; Patil, P. S.; Bhosale, P. N. Synthesis and Characterization of Chemically Grown Electrochromic Tungsten Oxide. *J. Sol-Gel Sci. Technol*. **2010**, *56*, 177–183.

37. González-Borrero, P. P.; Sato, F.; Medina, A. N.; Baesso, M. L.; Bento, A. C.; Baldissera, G.; Persson, C.; Niklasson, G. A.; Granqvist, C. G.; Ferreira da Silva, A. Optical Band-Gap Determination of Nanostructured WO_3 Films. *Appl. Phys. Lett*. **2010**, *96*, 061909.

38. De Angelis, F.; Fantacci, S.; Selloni, A.; Grätzel, M.; Nezeeruddin, M. K. Influence of the Sensitizer Adsorption Mode on the Open-Circuit Potential of Dye-Sensitized Solar Cells. *Nano Lett*. **2007**, *7*, 3189–3195.

39. De Angelis, F.; Fantacci, S.; Mosconi, E.; Nezeeruddin, M. K.; Grätzel, M. Adsorption Spectra and Excited State Energy Levels of the N719 Dye on TiO_2 in Dye-Sensitized Solar Cell Models. *J. Phys. Chem. C* **2011**, *115*, 8825−8831.

40. Mosconi, E.; Yum, J.-H.; Kessler, F.; Gómez García, C. J.; Zuccaccia, C.; Cinti, A.; Nezeeruddin, M. K.; Grätzel, M.; De Angelis, F. Cobalt Electrolyte/Dye Interactions in Dye-Sensitized Solar Cells: A Combined Computational and Experimental Study. *J. Am. Chem. Soc*. **2012**, *134*, 19438–19456.

41. Shirai, S.; Sato, S.; Suzuki, T. M.; Jinnouchi, R.; Ohba, N.; Asahi, R.; Morikawa, T. Effects of Ta_2O_5 Surface Modification by NH_3 on the Electronic Structures of a Ru-Complex/N–Ta_2O_5 Hybrid Photoccatalyst for Selective CO_2 Reduction. *J. Phys. Chem. C* **2018**, *122*, 1921−1929.

42. Eichkorn, K.; Treutler, O.; Öhm, H.; Häser, M.; Ahlrichs, R.; Auxiliary Basis Sets to Approximate Coulomb Potentials. *Chem. Phys. Letters*, **1995**, *242*, 652–660.

43. Becke, A. D. Density-Functional Exchange-Energy Approximation with Correct Asymptotic Behavior. *Phys. Rev. A* **1988**, *38* 3098−3100.

44. Lee, C.; Yang, W.; Parr. R. G. Development of the Colle-Salvetti Correlation-Energy Formula into a Functional of the Electron Density. *Phys. Rev. B* **1988**, *37*, 785−789.

45. Becke, A. D. Density-Functional Thermochemistry. III. The Role of Exact Exchange. *J. Chem. Phys*. **1993**, *98*, 1372−1377.

46. Schäfer, A.; Horn H.; Ahlrichs, R.; Fully Optimized Contracted Gaussian Basis Sets for Atoms Li to Kr. *J. Chem. Phys*. **1992**, *97*, 2571–2577.

47. Eichkorn, K.; Weigend, F.; Treutler O.; Ahlrichs, R.; Theor. Auxiliary Basis Sets for Main Row Atoms and Transition Metals and Their Use to Approximate Coulomb Potentials. *Theor. Chem. Acc*. **1997**, *97*, 119–124.

48. Ahlrichs, R.; Bär, M.; Häser, M.; Horn, H.; Kölmel, C. Electronic Structure Calculations on Workstation Computers: The Program System Turbomole. *Chem. Phys. Lett*. **1989**, *162*, 165–169.

49. Bauernschmitt R.; Ahlrichs, R. Treatment of Electronic Excitations within the Adiabatic Approximation of Time Dependent Density Functional Theory. *Chem. Phys. Letters* **1996**, *256*, 454–464.

50. Bauernschmitt, R.; Häser, M.; Treutler, O.; Ahlrichs, R. Calculation of Excitation Energies within Time-Dependent Density Functional Theory Using Auxiliary Basis Set Expansions. *Chem. Phys. Letters* **1997**, *264*, 573–578.

51. Klamt, A.; Schüürmann, G. COSMO: A New Approach to Dielectronic Screening in Solvent with Explicit Expressions for the Screening Energy and Its Gradient. *J. Chen. Soc. Perkin Trans. 2*, **1993**, *0*, 799–805.

52. Xie, Z.; Bau, R.; Reed, C. A. A Crystalline$[H_9O_4]^+$ Hydronium Ion Salt with a Weakly Coordinating Anion. *Inorg Chem*. **1995**, *34*, 5403–404.

53. Zhan, C.-G.; Dixon, D. A. Absolute Hydration Free Energy of the Proton from First-Principle Electronic Structure Calculations. *J. Phys. Chem. A* **2001**, *105*, 11534–1540.

54. Headrick, J. M.; Diken, E. G.; Walters, R. S.; Hammer, N. I.; Christie, R. A.; Cui, J.; Myshakin, E. M.; Duncan, M. A.; Johnson, M. A.; Jordan, K. D. Spectral Signatures of Hydrated Proton Vibrations in Water Clusters. *Science* **2005**, *308*, 1765–1769.

55. Esser, T. K.; Knorke, H.; Asmis, K. R. Deconstructing Prominent Bands in the Terahertz Spectra of $H_7O_3^+$ and $H_9O_4^+$: Intermolecular Modes in Eigen Clusters. *J. Phys. Chem. Lett*. **2018**, *9*, 798–803.

56. O'Boyle, N. M.; Tenderholt, A. L.; Langner, K. M. cclib: A library for package‐independent computational chemistry algorithms. *J. Comput. Chem*. **2008**, *29*, 839–845.

57. Lü, X.; Xu, X.; Wang, N. Q.; Zhang, Q.; Ehara, M.; Nakatsuji, H. Cluster Modeling of Metal Oxides: How to Cut Out a Cluster? *Chem. Phys. Lett*. **1998**, *291*, 445−452.

58. Xu, X.; Nakatsuji, H.; Ehara, M.; Lü, X.; Wang, N. Q.; Zhang, Q. E. Cluster Modeling of Metal Oxides: The Influence of the Surrounding Point Charges on the Embedded Cluster. *Chem. Phys. Lett*. **1998**, *292*, 282−288.

59. Xu, X.; Nakatsuji, H.; Lu, X.; Ehara, M.; Cai, Y.; Wang, N. Q.; Zhang, Q. E. Cluster Modeling of Metal Oxides: Case Study of MgO and the CO/MgO Adsorption System. *Theor. Chem. Acc*. **1999**, *102*, 170−179.

60. Huda, M. N.; Yan, Y.; Moon, C.-Y.; Wei, S.-H.; Al-Jassim, M. M. Density-Functional Theory of the Effects of Atomic Impurity on the Band Edge of Monoclinic WO_3. *Phys. Rev. B* **2008**, *77*, 195102.

61. Wang, F.; Di Valentin, C.; Pacchioni, G. Electronic and Structural Properties of WO_3: A Systematic Hybrid DFT Study. *J. Phys. Chem. C* **2011**, *115*, 8345–8353.

62. Wang, F.; Di Valentin, C.; Pacchioni, G. DFT study of Hydrogen Adsorption on the Monoclinic WO_3(001) Surface. *J. Phys. Chem. C* **2012**, *116*, 10672–10679.

63. Xu, Y.; Carlson, S.; Norrestam, R. Single Crystal Diffraction Studies of WO_3 at High Pressures and the Structure of a High-Pressure WO_3 Phase. *J. Solid State Chem.* **1997**, *132*, 123–130.

64. Jin, H.; Zhou, H.; Zhang, Y. Insight into the Mechanism of CO Oxidation on WO_3(001) Surfaces for Gas Sensing: A DFT Study. *Sensors* **2017**, *17*, 1898.

65. Albanses, E.; Valentin, C. D.; Pacchioni, G. H_2O Adsorption on WO_3 and WO_{3-x}(001) Surfaces. *ACS Appl. Mater. Interfaces* **2017**, *9*, 23212–23221.

66. Ola, O.; Maroto-Valer M. M. Reviw od Material Design and Reactor Engineering on TiO_2 Photocatalysis for CO_2 Reduction. *J. Photochem. Photobiol. C* **2015**, *24*, 16-42.

67. Fröhlich, D.; Kenklies, R. Band-Gap Assignment in SnO_2 by Two-Photon Spectroscopy. *Phys. Rev. Lett*. **1978**, *41*, 1750–1751.

68. Reimann, K.; Steude, M. Experimental Determination of the Electronic Band Structure of SnO_2. *Solid State Commun*. **1998**, *105*, 649–652.

69. Feneberg, M; Lidig, C.; Lange, K.; Goldhahn, R.; Deumann, M. D.; Esser, N.; Bierwagen, O.; White, M. E.; Tsai, M. Y.; Speck, J. S. Ordinary and Extraordinary Dielectric Functions of Rutile SnO_2 up to 20 eV. *Appl. Phys. Lett*. **2014**, *104*, 231106.

70. Anwar, M. Z.; Kim, D. J.; Kumar, A.; Patel, S. K. S.; Otari, S.; Mardina, P.; Jeong, J.-H.; Sohn, J.-H.; Kim, J. H.; Park, J. T.; Lee, J.-K. SnO_2 hollow nanotubes: a novel and efficient support matrix for enzyme immobilization. *Scientific Reports* **2017**, *7*, 15333.

Table 3-1. Relative MO contribution of sizable electron excitation for the $(WO_3)_{40}$ cluster.

λ (nm)	Oscillator strength	Assignment	Contribution (%)
462.9	0.00238	HOMO–4 → LUMO	51.4
		HOMO–5 → LUMO	14.8
		HOMO–8 → LUMO	5.4
452.3	0.00247	HOMO–5 → LUMO	49.9
		HOMO–9 → LUMO	8.3
		HOMO–4 → LUMO	7.2
		HOMO–4 → LUMO+1	6.4
429.9	0.00214	HOMO–2 → LUMO+1	27.2
		HOMO–9 → LUMO	21.2
		HOMO–6 → LUMO	14.4
		HOMO–3 → LUMO	11.7
		HOMO–10 → LUMO	5.7
420.2	0.00241	HOMO–11 → LUMO	54.8
		HOMO–6 → LUMO+1	5.6
		HOMO–4 → LUMO+1	65.3

Table 3-2. Relative MO contribution of sizable electron excitation for **{$(Ir^{III}–OH_2)/WO_3$}**.

λ (nm)	Oscillator strength	Assignment	Contribution (%)
412.0	0.00306	HOMO–17 → LUMO	30.2
		HOMO–20 → LUMO	15.3
		HOMO–8 → LUMO+1	8.3
		HOMO–18 → LUMO	7.0
		HOMO–22 → LUMO	6.3
411.1	0.00216	HOMO–8 → LUMO+1	45.1
		HOMO–19 → LUMO	7.2
		HOMO–24 → LUMO	6.8
		HOMO–15 → LUMO	6.3
		HOMO–21 → LUMO	5.0
400.9	0.00293	HOMO–21 → LUMO	42.8
		HOMO–19 → LUMO	14.9
		HOMO–25 → LUMO	6.6

Table 3-3. Relative MO contribution of sizable electron excitation for **{(Ir^{III}–OH)$^{-1}$/WO$_3$}$^{-1}$**.

λ (nm)	Oscillator strength	Assignment	Contribution (%)
524.3	0.00979	HOMO → LUMO+17	18.4
		HOMO → LUMO+18	13.3
		HOMO → LUMO+41	8.4
		HOMO → LUMO+30	7.9
		HOMO → LUMO+40	5.8
436.5	0.00289	HOMO–19 → LUMO	37.4
		HOMO–20 → LUMO	23.3
		HOMO–21 → LUMO	9.4
		HOMO–3 → LUMO+6	7.1
427.4	0.00318	HOMO–1 → LUMO+15	50.4
		HOMO–1 → LUMO+14	25.7
		HOMO–1 → LUMO+13	10.5
426.3	0.00254	HOMO–16 → LUMO+1	30.4
		HOMO–25 → LUMO	8.8
		HOMO–30 → LUMO	6.8
		HOMO–27 → LUMO	6.4
		HOMO–23 → LUMO	5.8
417.4	0.00399	HOMO–4 → LUMO+9	55.1
		HOMO–4 → LUMO+8	8.1
		HOMO–4 → LUMO+6	6.4
409.4	0.0135	HOMO–1 → LUMO+18	65.9
		HOMO–1 → LUMO+19	5.3
405.7	0.0275	HOMO–1 → LUMO+19	43.8
		HOMO–1 → LUMO+20	10.1
403.8	0.0156	HOMO–1 → LUMO+19	41.8
		HOMO–1 → LUMO+18	21.5
426.3	0.00254	HOMO–64 → LUMO	10.1
		HOMO–16 → LUMO+3	6.9
		HOMO–59 → LUMO	5.3
		HOMO–18 → LUMO+3	5.3
		HOMO–58 → LUMO	5.0

Table 3-4. Relative MO contribution of sizable electron excitation for **{(Ir^{IV}–OH)/WO_3}**.

λ (nm)	Oscillator strength	Assignment	Contribution (%)
489.0	0.00467	HOMO–171 (β) → LUMO (β)	36.6
		HOMO–251 (β) → LUMO (β)	12.6
		HOMO–163 (β) → LUMO (β)	8.0
		HOMO–165 (β) → LUMO (β)	6.7
		HOMO–173 (β) → LUMO (β)	6.1
483.9	0.00479	HOMO–251 (β) → LUMO (β)	17.1
		HOMO–175 (β) → LUMO (β)	14.0
		HOMO–171 (β) → LUMO (β)	12.8
		HOMO–173 (β) → LUMO (β)	12.6
		HOMO–183 (β) → LUMO (β)	9.7
411.6	0.00369	HOMO–16 (β) → LUMO+4 (β)	16.1
		HOMO–17 (α) → LUMO+3 (α)	15.8
		HOMO–35 (β) → LUMO+2 (β)	7.0
		HOMO–34 (α) → LUMO+1 (α)	6.7
402.9	0.0127	HOMO–118 (α) → LUMO+5 (α)	19.1
		HOMO–306 (β) → LUMO (β)	8.4
		HOMO–14 (β) → LUMO+4 (β)	5.6
402.8	0.00451	HOMO–15 (α) → LUMO+3 (α)	9.5
		HOMO–118 (α) → LUMO+5 (α)	8.0
		HOMO–14 (β) → LUMO+4 (β)	6.4
402.8	0.00579	HOMO–38 (β) → LUMO+2 (β)	9.5
		HOMO–39 (α) → LUMO+1 (α)	7.5
		HOMO–40 (α) → LUMO+1 (α)	6.2
401.7	0.0103	HOMO–306 (β) → LUMO (β)	17.7
		HOMO–118 (α) → LUMO+5 (α)	14.4
		HOMO–322 (β) → LUMO (β)	6.6
		HOMO–308 (β) → LUMO (β)	5.7
		HOMO–256 (β) → LUMO (β)	5.5

Table 3-5. Relative MO contribution of sizable electron excitation for **{(Ir^{IV}=O)$^{-1}$/WO_3}$^{-1}$**.

λ (nm)	Oscillator strength	Assignment	Contribution (%)
536.8	0.00623	HOMO–1 (α) → LUMO+26 (α)	62.6
		HOMO–1 (α) → LUMO+25 (α)	13.0
		HOMO–1 (α) → LUMO+30 (α)	10.5
519.8	0.00782	HOMO–1 (α) → LUMO+28 (α)	45.7
		HOMO–1 (α) → LUMO+30 (α)	17.9
		HOMO–1 (α) → LUMO+26 (α)	11.8
		HOMO (β) → LUMO+53 (β)	5.2
504.0	0.0213	HOMO (β) → LUMO+57 (β)	10.1
		HOMO (β) → LUMO+59 (β)	7.8
		HOMO–1 (α) → LUMO+32 (α)	7.4
		HOMO–1 (α) → LUMO+30 (α)	6.8
		HOMO–1 (α) → LUMO+68 (α)	6.3
		HOMO–1 (α) → LUMO+60 (α)	6.1
442.9	0.00337	HOMO–2 (α) → LUMO+28 (α)	32.9
		HOMO–2 (α) → LUMO+30 (α)	18.1
		HOMO–2 (α) → LUMO+155 (α)	12.1
		HOMO–2 (α) → LUMO+167 (α)	11.7
442.7	0.00394	HOMO–5 (β) → LUMO+21 (β)	51.2
		HOMO–4 (α) → LUMO+20 (α)	19.8
442.0	0.00504	HOMO–2 (α) → LUMO+28 (α)	31.0
		HOMO–2 (α) → LUMO+167 (α)	16.7
		HOMO–2 (α) → LUMO+155 (α)	15.2
		HOMO–2 (α) → LUMO+30 (α)	9.8
402.5	0.00345	HOMO –5 (β) → LUMO+31 (β)	11.0
		HOMO –11 (β) → LUMO+8 (β)	8.2
		HOMO –5 (β) → LUMO+27 (β)	6.8
402.0	0.00269	HOMO (β) → LUMO+122 (β)	18.8
		HOMO (β) → LUMO+115 (β)	9.6
		HOMO–4 (α) → LUMO+26 (α)	6.8
		HOMO–4 (α) → LUMO+30 (α)	5.5.

Chapter 4

Methane Hydroxylation by an Iridium-Oxo Complex

4.1 Introduction

Methane is a major component of natural gas (about 90%) and methanol, its hydroxide, is the chemical row materials for industrial various chemical productions. However, it is difficult to activate C–H bond in methane due to its high stability derived from high and low energy of lowest unoccupied molecular orbital (LUMO) and highest occupied molecular orbital (HOMO), respectively.[1] In the currently commercial process, methane is converted into methanol involves a two-step reaction process via the synthesis gas ($CO + H_2$).[2,3] The first step is a steam-reforming, which is a reaction of methane with water to produce synthesis gas (Eq. 4–1). The second step is water-gas shift reaction, in which synthesis gas is converted to methanol and hydrogen gas via the formation of carbon dioxide by reacting with water (Eq. 4–2 and 3).[4,5] Because whole conversion process is endothermic reaction (Eq. 4–4), this industrial method requires high pressure (40 atm) and temperature (850 °C).

$CH_4 + H_2O \rightarrow CO + 3H_2$ ΔH = 49.3 kcal/mol. (4 – 1)

$CO + 2H_2 \rightarrow CH_3OH$ ΔH = –24.7 kcal/mol. (4 – 2)

$CO + H_2O \rightarrow CO_2 + H_2$ ΔH = –9.9 kcal/mol. (4 – 3)

$CO_2 + 3H_2 \rightarrow CH_3OH + H_2O$ ΔH = –14.8 kcal/mol. (4 – 4)

In contrast, the soluble and particulate methane monooxygenase (sMMO and pMMO) enzymes, which involve iron– and copper–oxo active sites, respectively, can catalyze the direct conversion of methane to methanol under mild conditions[6-11] with a calculated activation energy for the C–H bond cleavage being less than 20 kcal/mol.[11] This direct oxidation of methane is exothermic by 30.7 kcal/mol.[12,13] Therefore, many researcher have attempt to develop homogeneous and heterogeneous catalysts involving transition metal–oxo active sites like these enzymes [14-17]

$CH_4 + 1/2O_2 \rightarrow CH_3OH$ $\Delta H = -30.7$ kcal/mol. (4 – 5)

Among all transition metal–oxo species that have been investigated so far for the activation of small molecules,[18-20] iridium–oxo complexes show a promising ability to catalyze oxidation reactions.[20-23] Blakemore et al., for instance, reported a H_2O oxidation by $Cp^*Ir(O)(ppy)^+$ complex, where Cp* and ppy are pentamethyl cyclopentadienyl anion and 2-phenylpryridine, respectively, in the presence of cerium ammonium nitride (CAN) as an oxidant. They also performed the computational studies that the activation energy for the O–O bond formation is calculated to be 24.0 kcal/mol.[21] More interestingly, Zhou et al. in 2012 reported a catalytic decalin hydroxylation to 9-decalol (tertiary carbon oxidation) using the same catalyst and oxidant.[23] They demonstrated that $Cp^*Ir(O)(ppy)^+$ in the triplet and singlet states are energetically competitive and thus both are accessible due to a rather low activation energy for C–H bond cleavage in decalin (12.4 and 3.4 kcal/mol, respectively). Furthermore, they showed that the C–H bond cleavage of decalin in the triplet and singlet states proceeds through different mechanisms, namely radical rebound and oxygen insertion mechanisms. Interestingly, the oxygen insertion mechanism does not result in a radical intermediate. leading to a catalyst degradation.[24-29] Unfortunately, this complex is unable to catalyze methane hydroxylation due to rather high activation energy (25.7 kcal/mol) via the oxygen insertion mechanism.[23]

Meanwhile, Ogo and coworkers reported[30] a different kind of iridium–aqua complex, namely $[Ir^{III}(\eta^5\text{-}C_5Me_5)\{bpy(COOH)_2\}(H_2O)]^{2+}$ (**Ir^{III}–OH_2**), where $bpy(COOH)_2$ is 2,2'-bipyridine-4,4' dicarboxylic acid. This complex is able to catalyze H_2O oxidation on the WO_3 semiconductor electrodes without a need of such an oxidant as CAN. In Chapter 2 catalytic cycle of H_2O oxidation is discussed by performing density functional theory (DFT) calculations, where an iridium–oxo complex $[Ir^{V}(\eta^5\text{-}C_5Me_5)\{bpy(COOH)_2\}(O)]^{2+}$ (**Ir^{V}=O**) reacts with H_2O molecule to form O–O bond through water nucleophilic attack mechanism with a calculated activation energy of 21.0 kcal/mol being by 3 kcal/mol lower than that for $Cp^*Ir(O)(ppy)^+$[21], indicating that **Ir^{V}=O** is more electrophilic than $Cp^*Ir(O)(ppy)^+$. In Chapter 3 the reaction mechanism of the formation of **Ir^{V}=O** immobilized $WO_3(001)$ (**{(Ir^{V}=O)/WO_3}**) from **{(Ir^{III}–OH_2)/WO_3}** were demonstrated by considering the effect of electrode and visible-light irradiation, where deprotonation of the aqua or hydroxyl ligand play essential roles in activating the Ir 5*d* orbitals. Additionally, a Cp* degradation[24-29] leading to the decreasing of catalytic-

performance is unlikely to occur because such a surface-immobilized catalyst as **Ir^{V}=O** is a single-site catalyst[31] and does not require an oxidant.

Given such a background, in this chapter the possibility of methane hydroxylation by **Ir^{V}=O** is discussed by using DFT calculations. In particular, detail the mechanisms of how the C–H bond of methane is cleaved and how methanol is formed in triplet, open-shell singlet (^{OS}singlet), and closed-shell singlet (^{CS}singlet) states are Investigated. Since **Ir^{V}=O** is generated by the light-induced oxidation that generates electricity, as suggested in Chapter 3, the insertion of CH_4 and H_2O into **Ir^{V}=O** forming CH_3OH completes the catalytic cycle of a fuel cell (see Figure 4-1). Thus, the present study provides a theoretical prediction of an alternative promising catalyst for methane hydroxylation and light-driven methane fuel cell.[32]

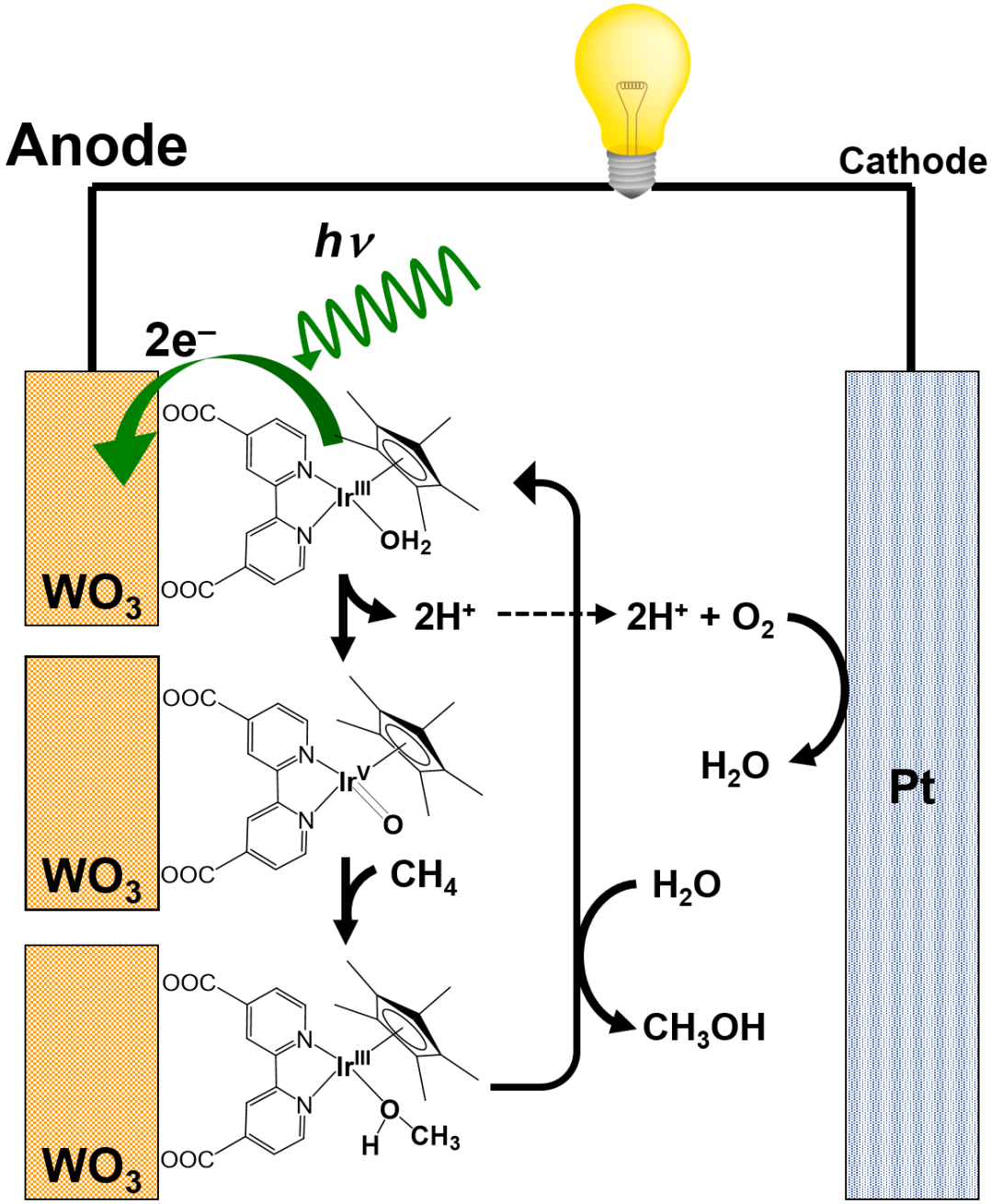

Figure 4-1. Schematic representation of the light-drive methane fuel cell catalyzed by **{(Ir^{III}–OH_2)/WO_3}** in anode.

4.2 Computational methodology

All optimized structures were obtained by using the B3LYP-D3 functional[33-36] as implemented in the Gaussian 16 packages.[37] The SDD[38] and TZVP[39] basis sets were used for the Ir atom and the rest of atoms, respectively. By calculating the analytical harmonic vibration frequencies, we confirmed that the obtained local minima and transition states have none and one imaginary frequency, respectively. All energies include zero-point correction (ZPC). To obtain intrinsic bond orbital (IBO)[40,41] we performed single-point calculations at the B3LYP/cc-pVTZ-PP(Ir)[42] + cc-pVTZ(H, C, O, N)[43] level of theory using TURBOMOLE program,[44] where transition state1, transition state2 and their intrinsic reaction coordinate (IRC) structures were obtained by using the Gaussian program. [37] IBOs are generated and visualized by using IboView30[41] using electron structures data calculated by TURBOMOLE. To analyze IBO changes provide important chemical information which can help one to uncover the nature of bonding in molecules and to analyze transition states.[40,41,45-47] IBO changes (ΔC_j) are plotted as the root-mean-square deviation of the orbital partial charges distribution among the toms with respect to the initial partial charge distribution. IBO changes are normalized by setting the last IBO change to 1 so that IBO changes can be easily compared to each other.

4.3 Results and discussion

4.3.1 Electronic Structure of Ir^{V}=O

Figure 4-5 shows MOs of **Ir^{V}=O** and their energies calculated in the ^{OS}singlet state. In **Ir^{V}=O**, the Ir 5*d* orbitals interact with the O 2*p* orbitals to form three bonding (σ_{z^2}, π_{zx}, and π_{yz}), three antibonding (σ_{z^2}*, π_{zx}*, and π_{yz}*), and two nonbonding (δ_{xy} and $\delta_{x^2-y^2}$) orbitals.[48-51] Among these, There are for full occupied (σ_{z^2}, π_{zx}, π_{yz}, and δ_{xy}), two unoccupied ($\delta_{x^2-y^2}$, and σ_{z^2}*), and two single occupied (π_{zx}* and π_{yz}*) orbitals. In α orbital we assign π_{zx}* to HOMO and π_{yz}* to LUMO, both of which are spatially orthogonal to each other (Figure 4-2), whereas in β orbital we assigned π_{zy}* to HOMO and π_{zx}* to LUMO. This indicates the electronic configuration of $(\pi_{zx}^*)^{\alpha}(\pi_{yz}^*)^{\beta}$. Also, these MO analysis propose electronic configurations of $(\pi_{zx}^*)^{\alpha}(\pi_{zx}^*)^{\beta}$, $(\pi_{zx}^*)^{\alpha}(\pi_{yz}^*)^{\beta}$, and $(\pi_{zx}^*)^{\alpha}(\pi_{yz}^*)^{\alpha}$ assigned to ^{CS}singlet, ^{CS}singlet, and triplet state, respectively.

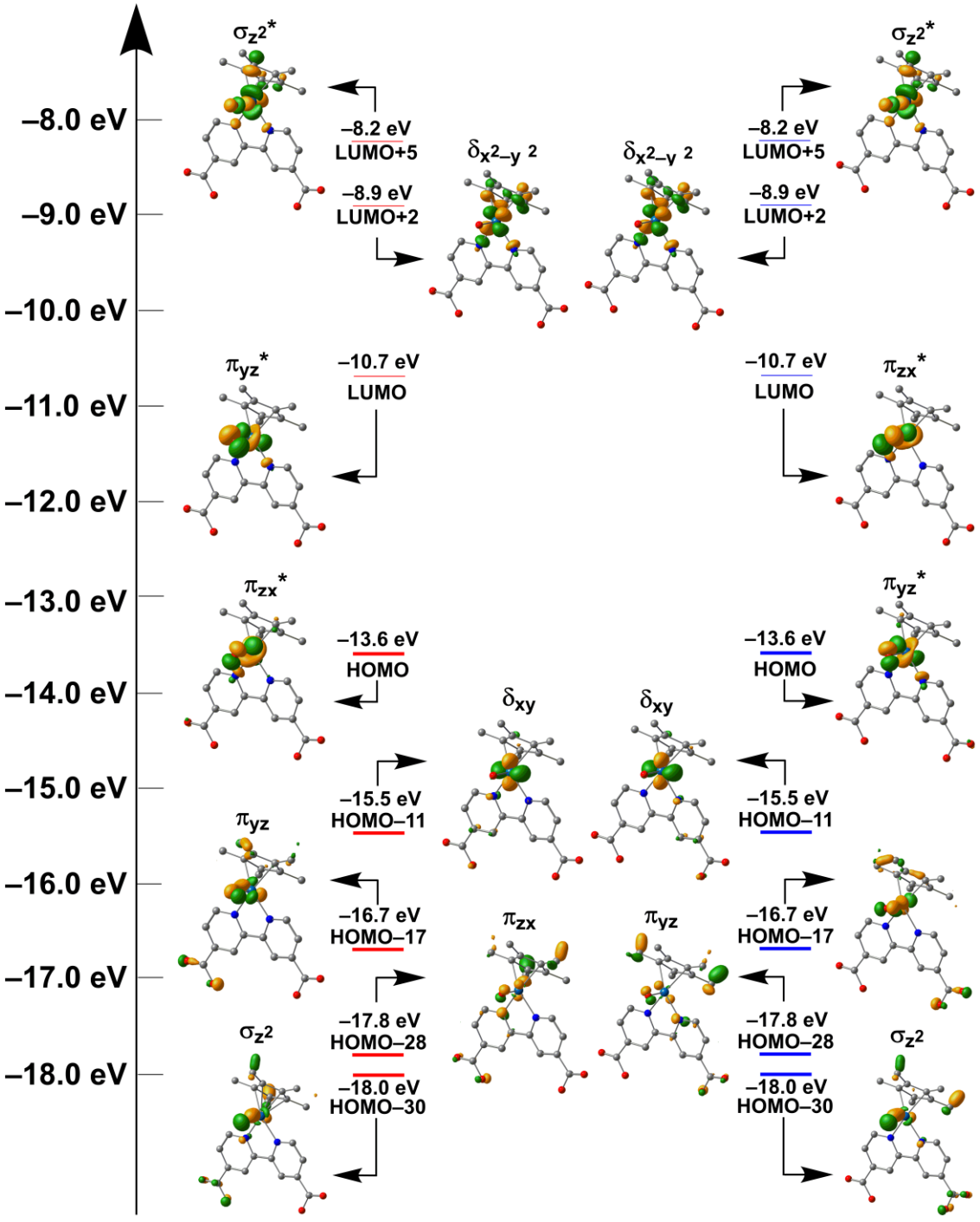

Figure 4-2. Ir=O-based molecular orbitals of **Ir^{V}=O** in the open-shell singlet (^{OS}singlet) state. Red and blue lines indicate the α and β spin orbital, respectively. Bold lines indicate the occupied orbitals. Each subscript describes the origin of each orbital involving the Ir 5*d* orbitals. The z-axis is oriented parallel to the axis of Ir=O. Note that x and y are arbitrary. Isovalue is 0.075. H atoms are omitted for clarity.

4.3.2 Reaction mechanism of the methane hydroxylation by $Ir^{V}=O$

Figure 4-3(a) shows computed energy diagrams for methane hydroxylation to methanol catalyzed by **$Ir^{V}=O$**, where the energies are measured relatively from the dissociation limit of **$Ir^{V}=O$** + CH_4 in the triplet state. As shown in this figure, **$Ir^{V}=O$** prefers the triplet state as the ground state, whereas **$Ir^{V}=O$** in the ^{OS}singlet and ^{CS}singlet states respectively lie 7.1 and 11.9 kcal/mol above that in the triplet state. The formation of a reactant complex (**rc**) provides energetic stabilization by 3.8, 3.7, and 4.0 kcal/mol in the triplet, ^{OS}singlet, and ^{CS}singlet states, respectively, with the triplet state still being the ground state, where methane is adsorbed on **$Ir^{V}=O$**. Subsequently, **rc** in the triplet and ^{OS}singlet states undergoes a homolytic C–H bond cleavage via a radical-like transition state (**ts1**) to form an intermediate species (**int1**). **int1** involves a methyl radical ($^{\bullet}CH_3$) and a hydroxyl bound to the Ir center (Ir–$OH^{\bullet}$). This is evidenced by the calculated Mulliken spin populations for the Ir–O species and C atoms of **int1** in the triplet (^{OS}singlet) state, that is, 0.93 and 1.00 $e^{-}/Å^3$ (–0.86 and 1.01 $e^{-}/Å^3$), respectively, which show a parallel (antiparallel) electron in each of $^{\bullet}CH_3$ and $^{\bullet}OH$ radical species. The activation energies for this reaction step in the triplet (^{OS}singlet) state is calculated to be 11.3 kcal/mol (7.4 kcal/mol). Since the energy difference between **int1** in the triplet and ^{OS}singlet states is only 0.2 kcal/mol, a spin inversion is likely to occur (green circle in Figure 4-3(a)). To estimate the energy cost for this spin-crossing, we plot energy diagrams of **int1** in the two spin states with a variation of fixed N–Ir–O–H dihedral angle from –38° to 12° (increment of 5°). As shown in Figure 4-3(b), the calculated energy for the spin crossover is only 0.7 kcal/mol at a dihedral angle of –10°, suggesting that spin crossover is easily likely to occur in the vicinity of **int1**.

On the other hand, calculated activation energy for the C–H bond cleavage in the ^{CS}singlet state is 5.6 kcal/mol, which is rather low than that in the triplet ground state. To proceed in the ^{CS}singlet state requires the energy of 12.2 kcal/mol for the spin inversion in **$Ir^{V}=O$**, which is higher than the activation energy for the C–H bond cleavage in the triplet state. However, this reaction is a great potential for the conversion of methane to methanol because of an important advantage that the radical intermediate involving $^{\bullet}CH_3$ is not produced, leading to the catalyst degradation.

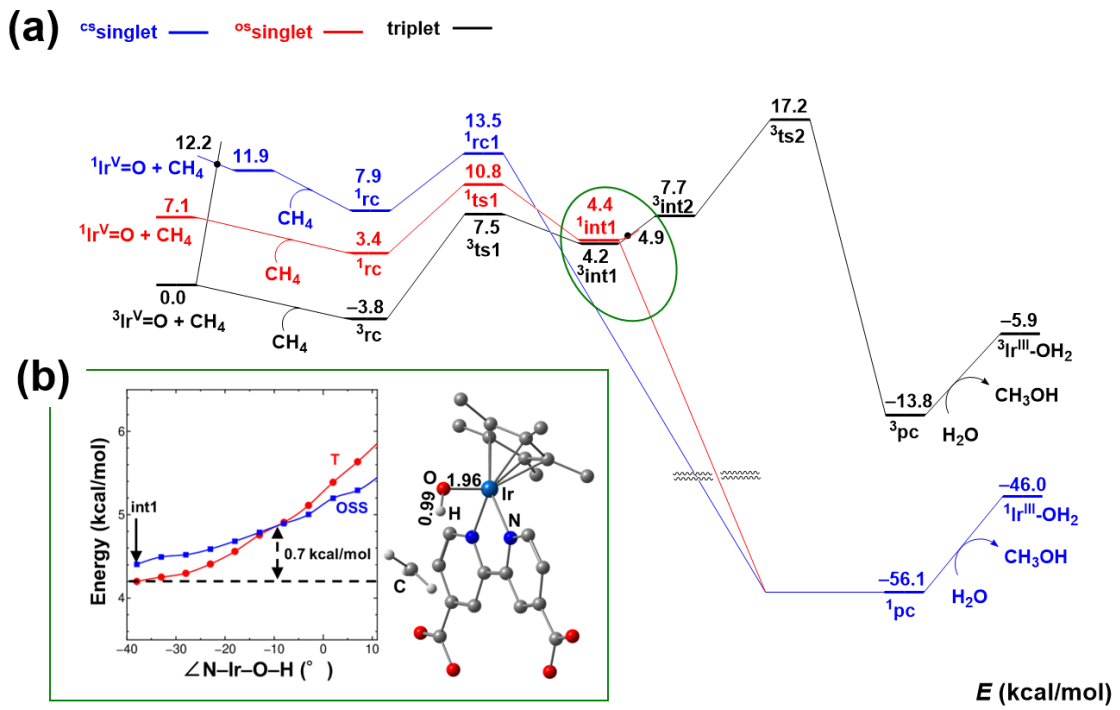

Figure 4-3. (a) Computed energy diagrams for methane hydroxylation to methanol in the triplet, open-shell singlet (^{OS}singlet), and closed-shell singlet (^{CS}singlet) states. **rc**, **ts**, **int**, and **pc** stand for reactant complex, transition state, intermediate state, and product complex, respectively. All energies are in kcal/mol. (b) (left) Potential energy surfaces of **int1** in the triplet and ^{OS}singlet states as a function of ∠N–Ir–O–H dihedral angle fixed and varied from –38° to 12°. To obtain these potential energy surfaces, we performed partial optimizations for **Int1** in the triplet state with a variation of fixed N–Ir–O–H dihedral angle from –38° to 12° (increment of 5°) and single-point calculations in the ^{OS}singlet state were carried out by using the geometries partially optimized in the triplet state. (right) The partial optimized geometry (∠N–Ir–O–H dihedral angle of –8°). Bond

Figure 4-4 shows the optimized structures and the analytical vibration vectors of **ts1** in the three considered spin states. The imaginary frequencies of **ts1** in the ^{OS}singlet and triplet states are calculated to be 1695*i* cm^{-1} and 1675*i* cm^{-1}, respectively, whose vibration vectors are both parallel to the direction of C···O (∠C–H–O = 180°). These also indicate the homolytic cleavage of C–H bond. **ts1** in the ^{CS}singlet state, on the other hand, forms a ∠C–H–O angle of 156° and has an imaginary frequency of 440*i* cm^{-1} with a vibration vector almost perpendicular to the O···H bond. This vibration corresponds to the rotation of OH ligand. The rather low imaginary frequency should derive from this vibration.

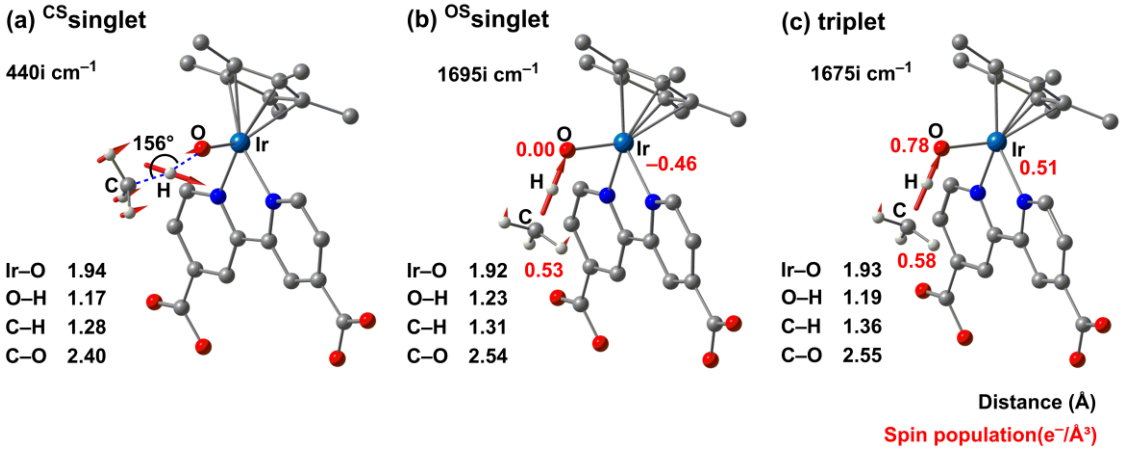

Figure 4-4. Optimized geometries of **ts1** in the (a) ^{CS}singlet, (b) ^{OS}singlet, and (c) triplet states. The imaginary frequency and its vector (red arrow) are shown for each geometry. The H atoms in the Cp* and bpy(COOH)$_2$ ligands are omitted for clarity.

int1 in the ^{OS}singlet state then directly forms **pc** of methanol in the ^{CS}singet state through a barrierless HO–CH$_3$ radical coupling. In contrast, **int1** in the triplet state first undergoes a slightly endothermic rotation of the $^{\bullet}$OH ligand to form **int2**. Subsequent C–O bond formation in the triplet state requires the activation barrier of 9.5 kcal/mol with an imaginary frequency of 467 cm^{-1} to form **pc**. This HO–CH$_3$ recombination is consistent with the rebound mechanism calculated by Shaik and co-workers.[52-54] Alternatively, the resultant $^{\bullet}$CH$_3$ of **int1** in the triplet state may desorb to form by-products (e.g. ethane), as reported by Nam and co-workers.[55-57] Considering that the desorption energy for the $^{\bullet}$CH$_3$ removal from **int1** is calculated to be 6.0 kcal/mol, which is higher than the energy for the **int1** spin crossover and the subsequent **pc** formation in the ^{CS}singlet state, the selectivity toward methanol formation is expected to higher than the by-product formation. The energy difference between **pc** in the ^{CS}singlet and triplet states is 42.3 kcal/mol, which corresponds to the singlet-triplet gap. Considering that **Ir^{V}=O** is originated from the light-induced oxidation of **Ir^{III}–OH$_2$**, the final step is ligand exchange reaction between the methanol aqua ligands, requiring 10.1 and 7.9 kcal/mol in the ^{cs}singlet and triplet states, respectively.

4.3.3 Catalyst degradation reaction

Herein we discuss about the side reaction leading to the decreasing the catalytic performance. Generally, Cp* has a weak C–H bond and decomposes easily under oxidative conditions, leading to the self-destruction.[26-27] Figure 4-5(a) shows the energy diagrams of the C–H bond cleavage in Cp* ligand by abstracting of H by Ir^{V}=O species in the triplet state. Calculated activation energy for abstracting the H atom of Cp* ligand is 19.4 kcal/mol, due to a significant conformational change. This value is rather high than that for the C–H cleavage in methane. Therefore, the catalyst degradation by the Cp* decompose is unlikely to occur. Considering that **Ir^{V}=O** catalyzes H_2O oxidation leading to the O–O bond formation as discussed in Chapter 2, additional calculation of the water oxidation reaction by reacting with **Ir^{V}=O** with H_2O molecules (Figure 4-5(b)) is performed. H_2O oxidation leading to the formation of H_2O_2 is unlikely to occur as the activation energy of 18.6 kcal/mol is rather high than that in the methane hydroxylation (5.6 kcal/mol) although the energy in **ts_{Cp*}** and **ts1** in the ^{CS}singlet state is almost the same.

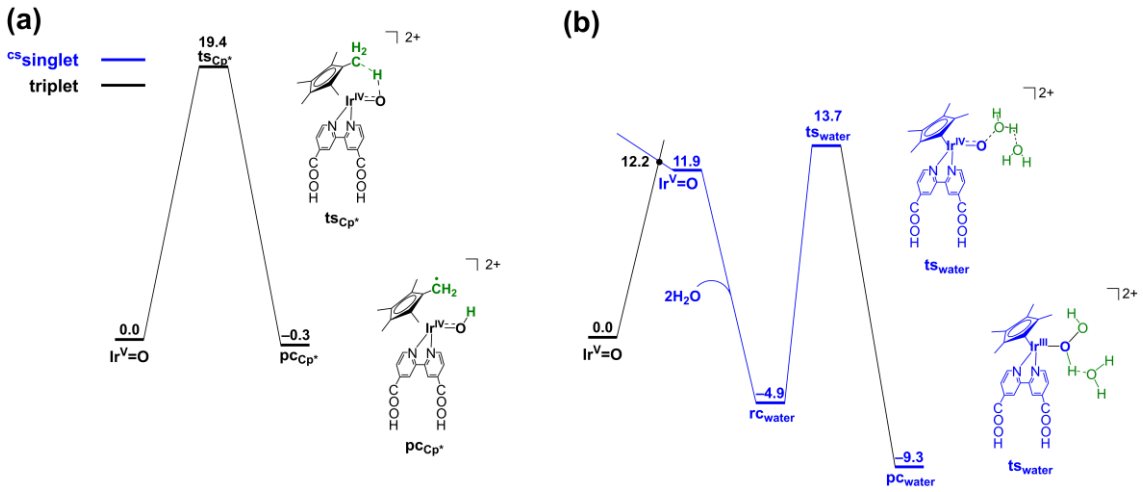

Figure 4-5. Computed energy diagrams for (a) Cp* degradation and (b) H_2O oxidation. Energies are measured from the dissociation limit of **Ir^{V}=O** and methane in the T state.

4.3.4 Detail reaction mechanism in the triplet state

To investigate more detail reaction mechanism in the triplet state, IBO analysis was performed. Let us first discuss in more detail the C–H bond cleavage mechanisms by performing IBO analysis. Figure 4-6(a) shows changes of the α and β IBOs during the

homolytic C–H bond cleavage in the triplet state, where the red and blue IBOs represent the α and β IBOs, respectively.Figure 4-6 (b) shows energy plot and IBO changes along the IRC of H-atom abstraction. In the beginning of this reaction (coordinate 1 (s = –3.12 $amu^{1/2}$bohr)) both the α and β IBOs are initially localized around the C–H bond, indicating a σ(C–H) bond. These two IBOs start to separate from each other when the σ(C–H) bond is elongated at coordinate 2 (s = –1.04 $amu^{1/2}$bohr), where the β IBO starts to migrate to the O moiety of the Ir^{V}=O species whereas α IBO remains unchanged. This IBO change continues to **ts1** (coordinate 3 (s = 0.00 $amu^{1/2}$bohr)) and even after **ts1** (coordinate 4 (s = 1.04 $amu^{1/2}$bohr)). Note that both IBOs abrupt changes near the transition state as shown in Figure 4-6(b). These IBO changes show that the α and β IBOs in σ(C–H) bond change to C-centered and O–H bond orbitals consisting of $^{\bullet}CH_3$ and $^{\bullet}$OH radicals, respectively. Interestingly, α and β IBOs changes at the same time. These results again shows that the cleavage is originated from the migration of the β IBO only and also suggests that the cleavage is a hydrogen atom transfer (HAT) reaction.[58] Due to the similar imaginary frequency, the same description of reaction mechanism also applies to the C–H bond cleavage in the ^{OS}singlet state.

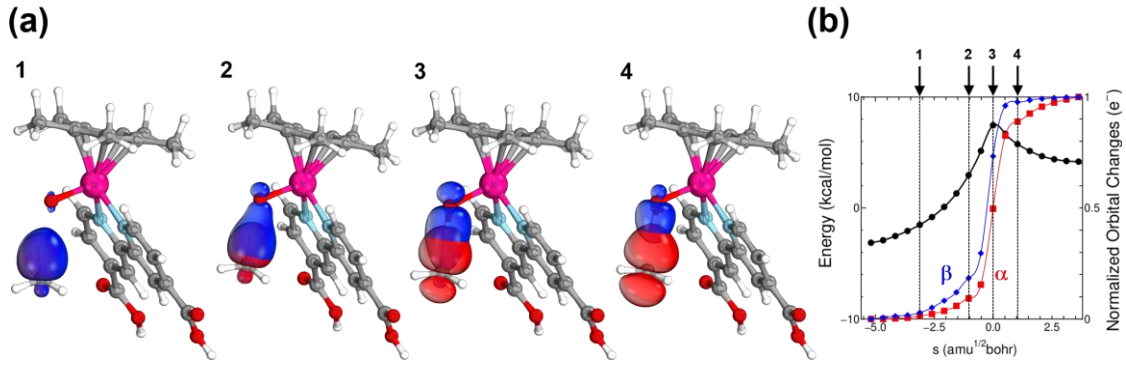

Figure 4-6. (a) Changes of the intrinsic bond orbital (IBO) during the C–H cleavage of methane in the triplet state along selected intrinsic reaction coordinates (IRCs). Red and blue isosurfaces indicate the α and β IBOs, respectively. Phase of wavefunction is removed for clarity. (b) Energy plot (black line, scaled to the y axis on the left) and normalized IBO changes (red and blue lines, scaled to the y axis on the right) along the IRC (s=0 is aligned to **ts1**).

Having discussed about the detail reaction mechanism of the C–H bond cleavage in the triplet state, we next discuss about the C–O bond formation in the triplet state. The main reaction pathway for the formation of methanol is C–O radical coupling in the ^{OS}singlet state without barrier through a direct C–O radical coupling that forms a highly stable **pc** in the ^{CS}singlet state. On the contrary, such a radical coupling in the triplet state cannot proceed due to the Pauli exclusion principle. Instead, **ts2** should first be overcome before the formation of **pc** in the triplet state, which is energetically less preferable than that in the ^{CS}singlet state. It is interesting in the chemical bond formation between radical species with the same spin although this reaction is not the main pathway for the formation of methanol,

To obtain a better understanding on the mechanism of **pc** formation in the triplet state, IBO analysis of **ts2** are performed. Figure 4-7(a) shows changes of O- and C-centered α-IBO s (shown by red and yellow isosurfaces, respectively) along the IRC, where coordinate 2 is **ts2**. Although O-centered IBO is doubly occupied, indicating the lone pair of O atom, it should be noted that Figure 4-7 shows only its α orbital. The O-centered IBO then forms a C–O bonding orbital as the reaction progressing, which describes a nucleophilic attack of the lone pair in O atom to the C atom. On the other hand, the C-centered IBO changes to the Ir-centered IBO, which is a Ir 5*d* orbital. This indicates an electron transfer from the C atom to the Ir atom. Figure 4-7(b) shows that these changes of both IBOs occur simultaneously, indicating a concerted mechanism. Therefore, we obtain the conclusion that the **pc** formation in the triplet state proceeds through the electron transfer from the $^{\bullet}CH_3$ to the Ir 5*d* orbital.

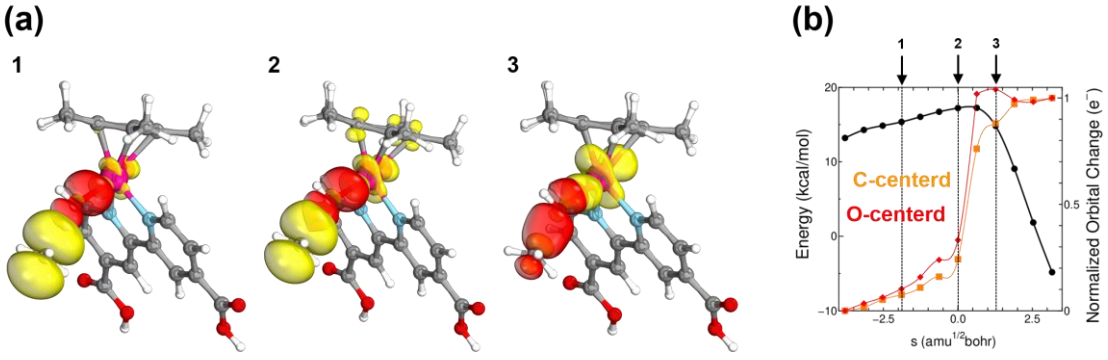

Figure 4-7. (a) Changes of O- and C-centered α- IBOs, shown by red and yellow isosurfaces, respectively, along selected IRCs. Phase of wavefunction is omitted for clarity. (b) Energy plot (black line, scaled to the y axis on the left) and normalized IBO changes (colored lines, scaled to the y axis on the right) along the IRC (s=0 is aligned to **ts2**).

4.3.5 C–H bond cleavage in the ^{CS}singlet state

Having established the reaction mechanism of C–H bond cleavage and C–O bond formation in the triplet state, we now look at the detail reaction mechanism in the ^{cs}singlet state, especially the C–H bond cleavage. The C–H bond cleavage in the ^{CS}singlet state, in which a H atom is abstracted by metal-oxo species ($M^{(n+2)+}$=O), can possibly be described by two different mechanisms, namely the hydride transfer (HT) and proton transfer (PT) mechanisms (Scheme 4-1). In the HT mechanism, a hydride migrates to the O moiety of the $M^{(n+2)+}$=O while electrons localized on one of the M–O bonds are transferred to the metal center, resulting in a reduced metal center ($M^{(n+2)+} \rightarrow M^{n+}$). Subsequently, the resultant methyl cation (CH_3^+) reacts with the hydroxyl ligand (M–OH^-) to form methanol complex (product complex) through Coulomb interactions. This mechanism is originally proposed by Earloss and Privalov. They demonstrated a hydride transfer from alkanes to Re^{VII}OO peroxo species to form alcohol.[59] On the contrary, in the PT mechanism one of the M–O bonds makes a nucleophilic attack to the H atom to form a methyl anion (CH_3^-) and a M–OH^+. Here, a reduction of the M center from $M^{(n+2)+}$ to M^{n+} occurs via electron transfer from the OH ligand to the metal atom to subsequently form a H_3C–OH bond.

Scheme 4-1. The Hydride Transfer (HT) and Proton Transfer (PT) Mechanisms for Methane Hydroxylation to Methanol by Metal-Oxo Complex in the ^{CS}singlet state.

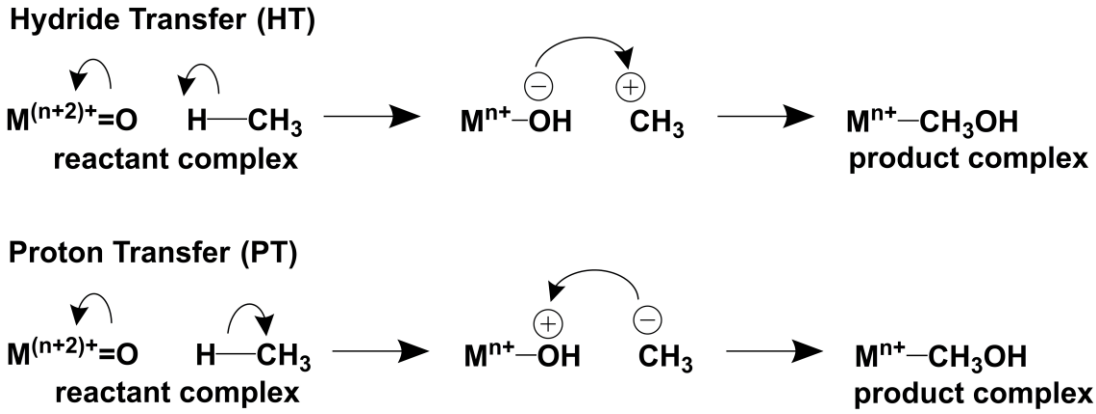

To investigate which mechanisms is plausible path in the methanol formation by **Ir^{V}=O** in the ^{CS}singlet state, IBO analysis for the C–H bond cleavage is performed. Figure 4-8(a), (b), and (c) show change of Ir–O bond (π type), C–H bond (σ type), and O-centered IBOs. As shown in Figure 4-8(a), the Ir–O IBO (π type) changes into an Ir-localized IBO along the IRC, which corresponds to the reduction of the Ir center from Ir^{V} to Ir^{III}. This IBO change starts after coordinate 2 (s = –3.38 $amu^{1/2}$bohr). the The C–H IBO shown in Figure 4-8(b), which forms an O–H σ bond coming mainly from the H 1s orbital. This observation indicates that the H atom of methane is transferred to the Ir=O as a hydride. This IBO change start after coordinate 2 and continues after coordinate 3 (s = 0.00 $amu^{1/2}$bohr). In Figure 4-8(c), it is seen that the IBO of O-centered migrates to the C atom to form a H_3C–OH bond. This IBO change starts after coordinate 2. From this analysis, we conclude that the methane hydroxylation to methanol in the ^{CS}singlet state proceeds through the HT mechanism, which is reasonable since the Ir^{V}=O species has a strong electrophilicity and thus easily reacts with water molecule to form an O–O bond.[20-22] Additionally, these IBO changes take place step by step. This observation is also shown in In Figure 4-8(d). More specifically, the Ir–O IBO first changes to an orbital localized around the Ir center, then the H atom migrates from methane to the Ir–O, and finally the O-centered IBO forms the C–O bond (Figure 4-8(e)). This indicates that the HT mechanism is triggered by the Ir–O IBO changes, showing the reduction of the Ir atom ($Ir^{V} \rightarrow Ir^{III}$).

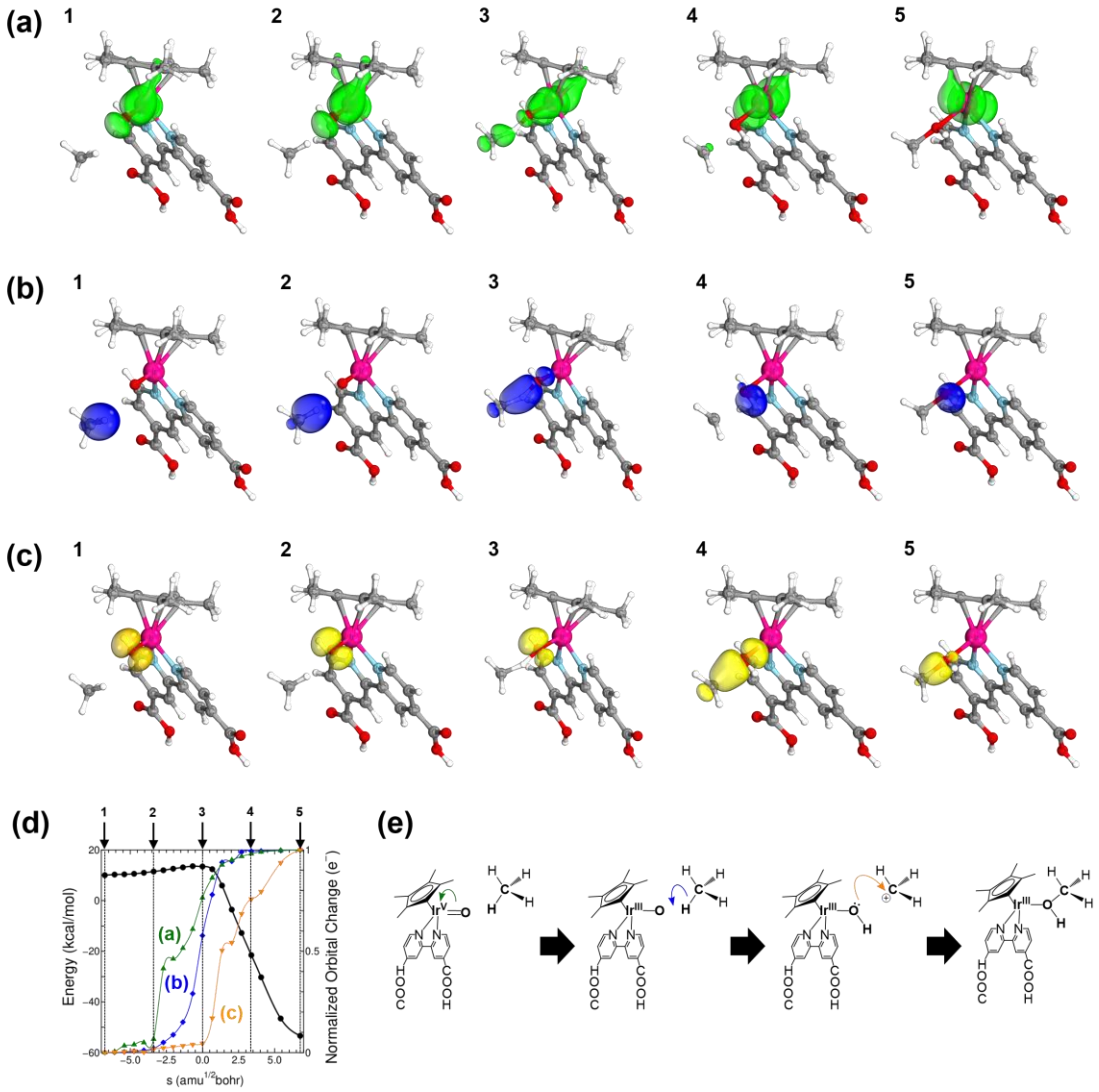

Figure 4-8. Changes of IBO at (a) the Ir–O bond (π type), (b) C–H bond, and (c) O-centered along selected IRCs in the ^{CS}singlet state without spin polarization. Phase of wavefunction is removed for clarity. (d) Energy plot (black line) and normalized IBO changes (green, blue, and yellow lines corresponding to the (a), (b), and (c), respectively) along the IRC (s=0 is aligned to **ts1**). (e) Schematic representation of the reaction mechanism of the C–H bond activation in the ^{CS}singlet state based on IBO analysis.

Zhou et al. suggested from DFT calculations that the activation energy for the C–H bond cleavage of methane by $[Ir^{V}(\eta^{5}\text{-}C_5H_5)\{ppy\}(O)]^{2+}$ in the ^{CS}singlet state is 25.7 kcal/mol,[23] with the result that they conclude that this iridium–oxo complex cannot catalyze the methane hydroxylation. In contrast, our calculated activation energy of 5.6 kcal/mol is low enough to activate the C–H bond of methane at room temperature although this reaction is unfavored than

that in the triplet and ^{OS}singlet states. Considering that the level of theory used in the work of Zhou et al. differs from the present one, which prevents us from direct comparison, recalculations for methane hydroxylation over $[Ir^{V}(\eta^{5}\text{-}C_5H_5)\{ppy\}(O)]^{2+}$ and $[Ir^{V}(\eta^{5}\text{-}C_5Me_5)\{ppy\}(O)]^{2+}$ in the ^{CS}singlet state are performed by using the same methods as presented here. The results shown in Figure 4-9 demonstrated that the C–H activation energy is still higher than that for **Ir^{V}=O**. This result is consistent with the rather high imaginary frequencies in both structures (used ppy ligand) than that in the present case (used bpy(COOH)$_2$ ligand). This suggests that the H-atom abstraction of methane in the ^{CS}singlet state significantly depends on the ligands used, where in the present case the bpy(COOH)$_2$ ligand of **Ir^{V}=O** provides a higher electrophilicity to the Ir–O species, as theoretically demonstrated for H_2O oxidation in Chapter 2. Therefore, we expect that the ligand effect plays an important role in the electrophilicity of iridium complex, which is essential for the methane hydroxylation in the ^{CS}singlet state through the HT mechanism.

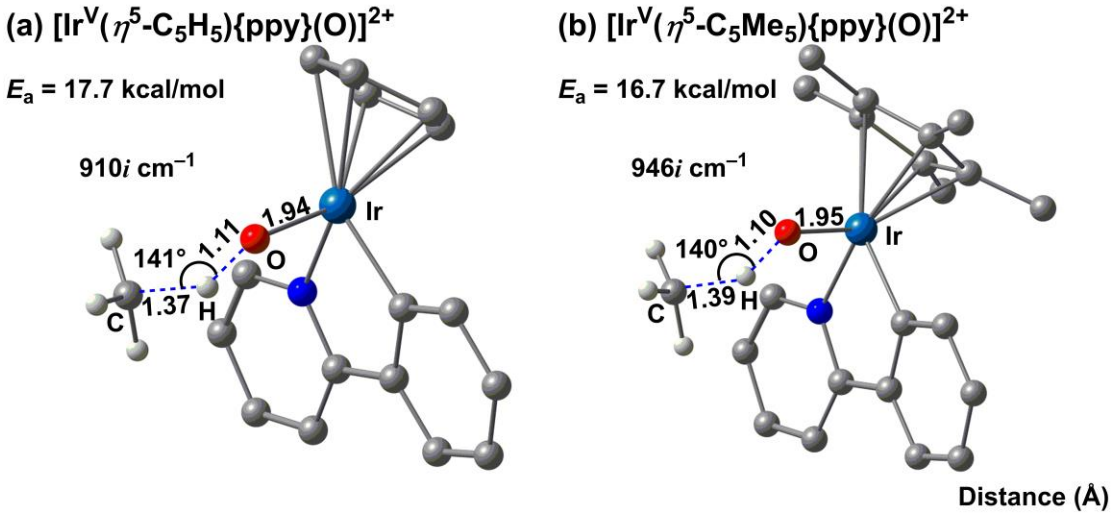

Figure 4-9. Optimized geometries of transition states in the C–H bond activation by (a) $[Ir^{V}(\eta^{5}\text{-}C_5H_5)\{ppy\}(O)]^{2+}$ and (b) $[Ir^{V}(\eta^{5}\text{-}C_5Me_5)\{ppy\}(O)]^{2+}$ in the ^{CS}singlet state. H atom in Cp(C_5H_5), Cp*(C_5Me_5), and ppy ligands are omitted for clarity. Units in bond length are in Å. E_a indicate the activation energy of the C–H bond cleavage in the methane.

4.3.6 Overview of reaction mechanism

The mechanisms of methane hydroxylation by **Ir^{V}=O** in three possible spin states are shown in Scheme 4-2. First, the C–H bond of methane is cleaved preferably in the triplet state with an activation barrier of 11.3 kcal/mol although that in the ^{os}singlet state is also accessible with energy differences at **ts1** and **int1** of only 3.3 and 0.2 kcal/mol, respectively. Mechanistically, **Ir^{V}=O** in the ^{OS}singlet and triplet states abstracts the H atom of methane through the HAT mechanism, leading to the formation of radical intermediate involving Ir–OH$^{\bullet}$ and $^{\bullet}CH_3$ radicals (**int1**) via **ts1**. Subsequently, O–C bond formation, which is a radical coupling between the Ir–OH$^{\bullet}$ and $^{\bullet}CH_3$, takes place in the ^{OS}singlet state to form methanol (**pc**), whereas an electron transfer from the $^{\bullet}CH_3$ radical to the Ir atom and a nucleophilic attack of lone pair in the O atom occur simultaneously in the triplet state. The electron transfer corresponds to the activation barrier of 9.5 kcal/mol.

In the ^{CS}singlet state the H atom of methane, on the contrary, migrates to the iridium–oxo as a hydride and forms **pc** directly. This reaction consists of three elementary reaction steps, i.e. Ir atom reduction, hydride transfer (HT), and C–O bond formation. This indicates that the Ir atom reduction play an essential role for the reaction to proceed.

Scheme 4-2. Reaction Steps Involved in the Methane Hydroxylation by Ir^{V}=O in the ^{CS}singlet, ^{OS}singlet, and triplet states.

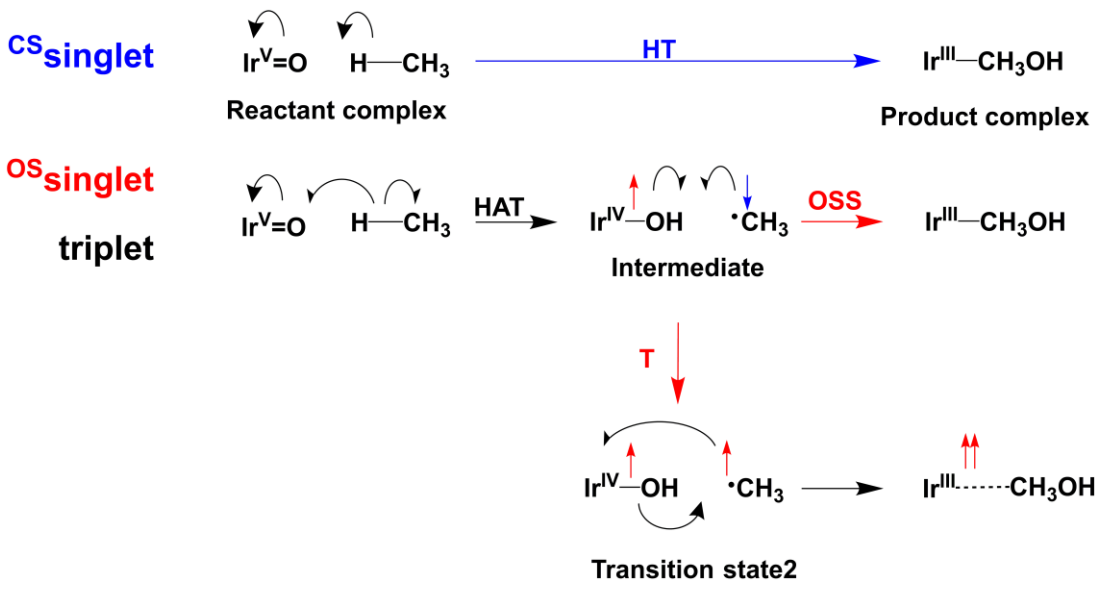

4.4 Conclusions

In this chapter DFT calculations are employed to investigate in detail the performance of an iridium–oxo complex $[Ir^{V}(\eta^{5}\text{-}C_5Me_5)\{bpy(COOH)_2\}(O)]^{2+}$ (**Ir^{V}=O**) hydroxylate methane to methanol toward a light-driven methane fuel cell. DFT calculations show that **Ir^{V}=O** favors the triplet state over the open-shell and closed-shell singlet (^{OS}singlet and ^{CS}singlet) states. In the C–H bond cleavage the H atom of methane migrates to the Ir^{V}=O species as an atom (hydrogen-atom transfer (HAT) mechanism) with activation energies of 11.3 and 7.4 kcal/mol, respectively for the cleavage in the triplet and ^{OS}singlet states. Here, a spin inversion to the ^{OS}singlet state might occur in intermediate species involving an Ir–OH$^{\bullet}$ species and a methyl radical ($^{\bullet}CH_3$). Subsequent HO–CH_3 recombination forming a product complex (**pc**) of methanol occurs preferably through a barrierless $^{\bullet}$C and $^{\bullet}$O radical coupling in the ^{OS}singlet $\rightarrow$ ^{CS}singlet state. The **pc** formation in the triplet state, on the contrary, takes place through the electron transfer from the $^{\bullet}CH_3$ to the Ir *d* orbital with an activation barrier of 9.5 kcal/mol. Since the presently calculated activation energies are lower than those for methane hydroxylation by $Cp^*Ir(O)(ppy)^{+}$, we reach a conclusion that **Ir^{V}=O** is an alternative promising candidate of catalyst for methane hydroxylation.

Despite unfavorable energetically, the C–H bond cleavage of methane in the ^{CS}singlet state occurs through the hydride transfer (HT) mechanism, where a hydride instead of a hydrogen atom is transferred from methane to the Ir^{V}=O species to form directly **pc**. The intrinsic bond orbital (IBO) analysis demonstrated that such a hydride transfer is triggered by the reduction of Ir^{V} to Ir^{III}. Comparison of activation energies and electrophilicity between **Ir^{V}=O** and $Cp^*Ir(O)(ppy)^{+}$ indicates that this reaction significantly depends on the ligands used, where the ligand inducing the decreasing the electron density in Ir^{V}=O is favored for the methane hydroxylation in the ^{CS}singlet state. Since **Ir^{V}=O** is formed by light-induced oxidation, DFT calculations in this study provides a possibility to develop light-driven methane fuel cell.

Reference

1. Yoshizawa, K.; Miyanishi, M. Orbital Concept for Methane Activation. In *Direct Hydroxylation of Methane*; Yoshizawa, K., Ed.; Springer: Singapore, 2020; pp 1–22.
2. Chilov, A. E.; Shul´pin, G. B. Activation of C – H bons by Metal Complexes. *Chem. Rev.* **1997**, *97*, 2879–2832.
3. Rostrup-Nielsen, J. R. Activity of Nickel Catalysts for Steam Reforming of Hydrocarbons. *J. Catal.* **1973,** *31*, 173–199.
4. Chinchen, G. C.; Denny, P. J.; Parker, D. G. Spencer, M. S. Whan, D. A. Mechanism of Methanol Synthesis from CO_2/CO/H_2 Mixtures over Copper/Zinc Oxide/Alumina Catalysts: Use of ^{14}C-Lablled Reactants. *Appl. Catal.* **1987**, *30*, 333–338.
5. Xu, J.; Froment, G. F. Methane Steam Reforming, Methanation and Water-Gas Shift: I. Intrinsic Kinetics. *AIChE J.* **1989**, *35*, 88–96.
6. Rosenzweig, A. C.; Frederick, C. A.; Lippard, S. J.; Nordlund, P. Crystal Structure of a Bacterial Non-Heme Iron Hydroxylase That Catalyzes the Biological Oxidation of Methane. *Nature* **1993**, *366*, 537–543.
7. Lieberman, R. L.; Rosenzweig, A. C. Crystal Structure of a Membrane-Bound Metalloenzyme That Catalyzes the Biological Oxidation of Methane. *Nature* **2005**, *434*, 177–182.
8. Solomon, E. I.; Heppner, D. E.; Johnston. E. M.; Ginsbach, J. W. Cirera, J. Qayyum, M.; Kieber-Emmons, M. T.; Kjaergaard, C. H.; Hadt, R. G.; Tian, L. Copper Active Sites in Biology. *Chem. Rev*. **2014**, *114*, 3659−3853.
9. Wang, V. C.-C.; Maji, S.; Chen, P. P.-Y.; Lee, H. K.; Yu, S. S.-F.; Chan, S. I. Alkane Oxidation: Methane Monooxygenases, Related Enzyme, and Their Biomimetics. *Chem. Rev.* **2017**, *117*, 8574–8621.
10. Cao, L.; Caldararu, O.; Rosenzweig, A. C.; Ryde, U. Quantum Refinement Dose Not Support Dinuclear Copper in Crystal Structures of Particulate Methane Monooxygenase. *Angew. Chem*., *Int. Ed*. **2018**, *57*, 162−166.
11. Yoshizawa, K.; Suzuki, A.; Shiota, Y.; Yamabe, T. Conversion of Methane to Methanol on Diiron and Dicopper Enzyme Models of Methane Monooxygenase: A Theoretical Study on a Concerted Reaction Pathway. *Bul. Chem. Soc. Jpn.* **2000**, *73*, 815–827.

12. Feig, A. L.; Lippard, S. J. Reactions of Non-Heme Iron(II) Centers with Dioxygen in Biology and Chemistry. *Chem. Rev*. **1994**, *94*, 759–805.

13. Lieberman, R. L., Shrestha, D. B.; Doan, P. E. Hoffman, B. M. Stemmler, T. L. Rosenzweig, A. C. Purified Particulate Methane Monooxygenase from *Methlococcus Capsulatus* (*Basth*) is a Dimer with Both Mononuclear Copper and a Copper-Containing Cluster. *Proc. Natl. Aca. Sci. U. S. A.* **2003**, *100*, 3820–3825.

14. Groothaert, M. H.; Smeets, P. J.; Sels, B. F.; Jacobs, P. A.; Schoonheydt, R. A. Selective Ocidation of Methane by the Bis(μ-Oxo)dicopper Core Stabilized on ZSM-5 and Mordenite Zeolites. *J. Am. Chem. Soc.* **2005**, *127*, 1394–1395.

15. Mahyuddin, M. H.; Shiota, Y.; Yoshizawa, K. Methane Selective Oxidation to Methanol by Metal-Exchanged Zeolites: A Review of Active Sites and Their Reactivity. *Catal. Sci. Technol*. **2019**, *9*, 1744–1768.

16. Sorokin, A. B.; Kudril, E. V.; Bouchu, D. Bio-inspired Oxidation of Methane in Water Catalized by N-bridged Diiron Phthalocyanine Complex. *Chem. Commun.* **2008**, 2562–2564.

17. Hori, Y.; Shiota, Y.; Tsuji, T.; Kodera, M.; Yoshizawa, K. Catalytic Performance of a Dicopper–Oxo Complex for Methane Hydroxylation. *Inorg. Chem.* **2018**, *58*, 8–11.

18. Gunay, A.; Theopold, K. H. C–H Bond Activation by Metal Oxo Compounds. *Chem. Rev.* **2010**, *110*, 1060–1081.

19. Borovik, A. S. C–H Functionalisation in Organic Synthesis Themed Issue *Chem. Soc. Rev.* **2011**, *40*, 1870–1874.

20. Blakemore, J. D.; Crabtree, R. H.; Brudvig, G. W. Molecular Catalysts for Water Oxidation. *Chem. Rev.* **2015**, *115*, 12974–13005.

21. Blakemore, J. D.; Schley, N. D.; Balcells, D.; Hull, J. F.; Olack, G. W.; Incarvito, C. D.; Eisenstein, O.; Brudvig, G. W.; Crabtree, R. H. Half-Sandwich Iridium Complexes for Homogeneous Water-Oxidation Catalysis. *J. Am. Chem. Soc.* **2010**, *132*, 16017−16029.

22. Savini, A.; Bellachioma, G.; Ciancaleoni, G.; Zuccaccia, C.; Zuccaccia, D.; Macchioni, A. Iridium(III) Molecular Catalysts for Water Oxidation: the Simpler the Faster. *Chem. Commun.* **2010**, *46*, 9218–9219.

23. Zhou, M.; Balcells, D.; Parent, A. R.; Crabtree, R. H.; Eisenstein, O. Cp* iridium Precatalysts for Selective C–H Oxidation via Direct Oxygen Insertion: A Joint Experimental/Computational Study. *ACS. Catal*. **2012**, *2*, 208−218.

24. Vilella, L.; Vidossich, P.; Balcells, D.; Lledós, A. Basic Ancillary Ligands Promote O–O Bond Formation in Iridium-Catalyzed Water Oxidation: A DFT study. *Dalton Trans*., **2011**, *40*, 11241−11247.

25. Grotjahn, D. B.; Brown, D. B.; Martin, J. K.; Marelius, D. C.; Abadjian, M. C.; Tran, H. N.; Kalyuzhny, G.; Vecchio, K. S.; Specht, Z. G.; Cortes-Llamas, S. A.; Miranda-Soto, V.; van Niekerk, C.; Moore, C. E.; Rheingold, A. L. Evolution of Iridium-Based Molecular Catalysts during Water Oxidation with Ceric Ammonium Nitrate. *J. Am. Chem. Soc*. **2011**, *133*, 19024-19027.

26. Hintermair, U.; Hachmi, S. M.; Elimelech, M.; Crabtree, R. H. Particle Formation during Oxidation Catalysis with Cp* Iridium Complxes. *J. Am. Chem. Soc.* **2012**, *134*, 9785–9795.

27. Hintermair, U.; Cheehan, S. W.; Parent, A. R.; Ess, D. H.; Richens, D. T.; Vaccaro, P. H.; Brudvig, G. W.; Crabtree, R. H. Precurosr Transformation during Molecular Oxidation Catalysis with Organometallic Iridium Complexes. *J. Am. Chem. Soc.* **2013**, *135*, 10837–10851.

28. Thomsen, J. M.; Huang, D. L.; Crabtree, R. H. Brudvig, G. W. Iridium-Based Complexes for Water Oxidation. *Dalton Trans*., **2015**, *44*, 12452−12472.

29. Crabtree, R. H. The Stability of Organometallic Ligands in Oxidation Catalysis. *J. Organomet. Chem.* **2015**, *751*, 174–180.

30. Kikkawa, M.; Yatabe, T.; Matsumoto, T.; Yoon, K.-S.; Suzuki, K.; Enomoto, T.; Kaneko, K.; Ogo, S. A Fusion of Biomimetic Fuel and Solar Cells Based on Hydrogenase, Photosystem II, and Cytochrome c Oxidase. *ChemCatChem* **2017**, *9*, 4024−4028.

31. Joya, K. S.; Subbaiyan, N. K.; D'Souza, F. de Groot, H. J. M. Surface-Immobilized Single-Site Iridium Complex for Electrocatalytic Water Splitting. *Angew. Chem. Int. Ed.* **2012**, *51*, 9601–9605.

32. Joglekar, M.; Nguyen, V.; Pylypenko, S.; Ngo, C.; Li, Q.; O'Reilly, M. E.; Gray, T. S.; Hubbard, W. A.; Gunnoe, T. B.; Herring, A. M.; Trewyn, B. G. Organometallic Complexes Anchored to Conductive Carbon for Electrocatalytic Oxidation of Methane at Low Temperature. *J. Am. Chem. Soc.* **2016**, *138*, 116–125.

33. Becke, A. D. Density-Functional Exchange-Energy Approximation with Correct Asymptotic Behavior. *Phys. Rev. A* **1988**, *38* 3098−3100.

34. Lee, C.; Yang, W.; Parr. R. G. Development of the Colle-Salvetti Correlation-Energy Formula into a Functional of the Electron Density. *Phys. Rev. B* **1988**, *37*, 785−789.

35. Becke, A. D. Density-Functional Thermochemistry. III. The Role of Exact Exchange. *J. Chem. Phys*. **1993**, *98*, 1372−1377.

36. Grimme, S. ; Antony, J.; Ehrlich, S.; Krieg, H. A Consistent an Accurate *ab initio* Parametrization of Density Functional Dispersion Correction (DFT-D) for the 94 elements H-Pu. *J. Chem. Phys.* **2010**, *132*, 154104.

37. Frisch, M. J.; Trucks, G. W.; Schlegel, H. B.; Scuseria, G. E.; Robb, M. A.; Cheeseman, J. R.; Scalmani, G.; Barone, V.; Petersson, G. A.; Nakatsuji, H.; Li, X.; Caricato, M.; Marenich, A. V.; Bloino, J.; Janesko, B. G.; Gomperts, R.; Mennucci, B.; Hratchian, H. P.; Ortiz, J. V.; Izmaylov, A. F.; Sonnenberg, J. L.; Williams-Young, D.; Ding, F.; Lipparini, F.; Egidi, F.; Goings, J.; Peng, B.; Petrone, A.; Henderson, T.; Ranasinghe, D.; Zakrzewski, V. G.; Gao, J.; Rega, N.; Zheng, G.; Liang, W.; Hada, M.; Ehara, M.; Toyota, K.; Fukuda, R.; Hasegawa, J.; Ishida, M.; Nakajima, T.; Honda, Y.; Kitao, O.; Nakai, H.; Vreven, T.; Throssell, K.; Montgomery, J. A., Jr.; Peralta, J. E.; Ogliaro, F.; Bearpark, M. J.; Heyd, J. J.; Brothers, E. N.; Kudin, K. N.; Staroverov, V. N.; Keith, T. A.; Kobayashi, R.; Normand, J.; Raghavachari, K.; Rendell, A. P.; Burant, J. C.; Iyengar, S. S.; Tomasi, J.; Cossi, M.; Millam, J. M.; Klene, M.; Adamo, C.; Cammi, R.; Ochterski, J. W.; Martin, R. L.; Morokuma, K.; Farkas, O.; Foresman, J. B.; Fox, D. J. *Gaussian 16*, Revision A. 03; Gaussian, Inc.: Wallingford ,CT, 2016.

38. Andrae, D.; Haeussermann, D.; Dolg, M.; Stoll, H.; Preuss, H. Energy-Adjusted *ab initio* Pseudopotentials for the Second and Third Row Transition Elements. *Theor. Chem. Acc.*, **1990**, *77*, 123−141.

39. Schaefer, A.; Huber, C.; Ahlrichs, R. Fully Optimized Contracted Gaussian Basis Sets of Triple Zeta Valence Quality for Atoms Li to Kr. *J. Chem. Phys.*, **1994**, 100, 5829−5835.

40. Knizia, G. Intrinsic Atomic Orbitals: An Unbiased Bridge Between Quantum Theory and Chemical Concepts. *J. Chem. Theory Comput.*, **2013** *9*, 4834−4843.

41. Knizia, G.; Klein, J. E. M. N. Electron Flow in Reaction Mechanisms–Revealed from First Principles. *Angew. Chem. Int. Ed.,* **2015**, *54*, 5518−5522.

42. Figgen, D.; Peterson, K. A.; Dolg, M.; Stoll, H. Energy-Consistent Pseudopotentials and Correction Consistent Basis Sets for the 5*d* Elements Hf–Pt. *J. Chem. Phys.* **2009**, *130*, 164108.

43. Dunning, T. H. Gaussin Basis Sets for Use in Correlated Molecular Calculations. I. The Atoms Boron Through Neon and Hydrogen. *J. Chem. Phys.* **1989**, *90*, 1007.

44. Ahlrichs, R.; Bär, M.; Häser, M.; Horn, H.; Kölmel, C. Electronic Structure Calculations on Workstation Computers: The Program System Turbomole. *Chem. Phys. Lett*. **1989**, *162*, 165–169.

45. Nunes dos Santos Comprido, L. Klein, J. E. M. N.; Knizia, G.; Kastner, J.; Häshmi, A. S. K. On the Accessible Reaction Channels of Vinyl Gold(I) Species: π- and σ-Pathways. *Chem. Eur. J.*, **2017**, *23*, 10901−10905.

46. Klein, J. E. M. N.; Knizia, G. cPCET versus HAT: A Direct Theoretical Method for Distinguishing X–H Bond-Activation Mechanisms. *Angew. Chem. Int. Ed.,* **2018**, *57*, 11913−11917.

47. Goetz, M. K.; Anderson, J. S. Experimental Evidence for pK_a-Driven Asynchronicity in C–H Activation by a Terminal Co(III)–Oxo Complex. *J. Am. Chem. Soc.* **2019**, *141*, 4051–4062.

48. Holm, R. H.; Metal-Centered Oxygen Atom Transfer Reactions. *Chem. Rev*. **1987** *87*, 1401−1449.

49. Carter, E. A.; Goddard, W. A. III Early- versus Late-Transition-Metal-Oxo Bonds: The Electronic Structure of VO^+ and RuO^+. *J. Phys. Chem.* **1988**, *92*, 2109–2115.

50. Shiota, Y.; Yoshizawa, K. Methane-to Methanol Conversion by First-Row Transition-Metal Oxide Ions: ScO^+, TiO^+, VO^+, CrO^+, MnO^+, FeO^+, CoO^+, NiO^+, and CuO^+. *J. Am. Chem. Soc.* **2000**, *122*, 12317–12326.

51. Winlker, J. R.; Gray. H. B. Electronic Structures of Oxo—Metal Ions. Struc. Bond. Structure and Bonding. **2012**. *142*, 17–28.

52. Filatov, M.; Harris, N.; Shaik, S. On the ”Rebound” Mechanism of Alkane Hydroxylation by Cytochrome P450: Electronic Structure of the Intermediate and the Electron Transfer Character in the Rebound Step. *Angew. Chem. Int. Ed.,* **1999**, *36*, 3510−3512.

53. Kumar, D.; de Visser, S. P.; Shaik, S. How Does Product Isotope Effect Prove the Operation of a Two-State “Rebound” Mechanism in C-H Hydroxylation by Cytochrome P450? *J. Am. Chem. Soc.* **2000**, *122*, 8977–8989.

54. Cho, K.-B.; Hirao, H.; Shaik, S.; Nam, W. To rebound or Dissociate? This is the Mechanistic Question in C–H hydroxylation by heme and nonheme metal–oxo complexes. *Chem. Soc. Rev*. **2016** *45*, 1197−1210.

55. Cho, K.-B.; Wu, X.; Lee, Y.-M.; Kwon, Y. H.; Shaik, S.; Nam, W. Evidence for an Alternative to the Oxygen Rebound Mechanism in C–H Bond Activation by Non-Heme $Fe^{IV}O$ Complexes. *J. Am. Chem. Soc.* **2012.** *134*, 20222–20225.

56. Cho, K.-B.; Shaik, S.; Nam, W. Theoretical Investigation into C–H Bond Activation Reaction by Nonheme $Mn^{IV}O$ Complexes: Multistate Reacticity with No Oxygen Rebound. *J. Phys. Chem. Lett.* **2012.** *3*, 2851–2856.

57. Cho, K.-B.; Hirao, H.; Shaik, S.; Nam, W. To Rebound or Dissociate? This is the Mechanistic Question in C–H Hydroxylation by Heme and Nonheme Metal-Oxo Complexes. *Chem. Soc. Rev.* **2016.** *45*, 1197–1210.

58. Dietl, N.; Schlangen, M.; Schwarz, H. Thermal Hydrogen-Atom Transfer form Methane: The Role of Radicals and Spin States in Oxo-Cluster Chemistry. *Angew. Chem. Int. Ed.*, **2012**, *51*, 5544–5555.

59. Karlsson, E. A.; Privalov, T. Oxidation of Ethes, Alcohols, and Unfunctionalized Hydrocarbons by the Methyltrioxorhenium/H_2O_2 System: A Computational Study on Catalytic C–H Bond Activation. *Chem. Eur. J.*, **2009**, *15*, 1862−1869.

.

Chapter 5

Benzene Hydroxylation by Ruthenium-Substituted Keggin-Type Polyoxometalate

5.1 Introduction

Owing to the high stability and strong C–H bond (~110 kcal/mol) arising from the resonance effect in aromatic ring, benzene hydroxylation by direct oxidation requires high thermal energy.[1-3] However, it is difficult of the hydroxylation by the aromatic nucleophilic substitution of hydroxyl group (OH^-) due to the electron rich of π orbital. The commercial process of benzene hydroxylation, on the other hand, avoids these problems by performing multi-step through cumene (2-propylbenzene). This industrial method is so-called "Cumene method".[4,5] In Cumene method cumene is first produced by reacting with benzene and propylene in the high pH aqueous solution. Subsequent oxidation reaction of cumene leads to the formation of dioxygen adduct (cumene-hydroperoxo). Finally, phenol is formed in which acetone is also produced as by-product. Although in Cumene method aromatic oxidation of benzene is performed under relative mild conditions, these is a serious problem that the market price of phenol is dependent on the marketability of acetone. In addition, the catalytic conversion of Cumene method is rather low (~5 %). Thus, economical, direct conversion of benzene to phenol has attracted the attention of researchers.

In contrast to the commercial process of conversion of benzene into phenol, some metalloenzymes such as cytochrome P450[6] and tyrosinase[7,8] catalyze direct oxidation of aromatic ring. These enzymes have a transition metal–oxo active site that react with aromatic ring to form C–O bond, directly. Motivated by functional and structure of active site in these enzymes, many catalyst having metal-oxo species have been developed.[9-15] However, it is well known that metal-oxo active site reacts with not only substrate but also catalyst ligand leading to the catalyst degradation. Additionally, the hydroxylation of methane and benzene catalyzed by these metal–oxo complex are performed in the harmful and high toxic organic solvent.

Among all transition metal–oxo species that have been investigated so far for the activation of small molecules, Keggin-type polyoxometalates (POMs) $[XM_{12}O_{40}]^{n-}$ (X = Al, Ga, Si, Ge, P, As and S (heteroatoms); M = Mo and W shown in Figure 5-1(a)), which is the most simple POMs, show a promising ability to catalyze oxidation reactions. This is because POMs is robustness, soluble in aqueous and organic solution, and less susceptible to oxidative damage.[16-18] Keggin-type POM consists of the tungsten oxide frame-work ($(WO_3)_{12}$) (Figure 1 (a) middle) and the heteroatoms oxide core (μ_4O_x –X) (Figure 5-1 (a) right), where the redox potential of POMs change as a direct result of the charge of the anion or bond length of μ_4O_x–X.[19-23] Additionally, Additionally, metal-substituted Keggin-type POMs $[T(O)XM_{11}O_{39}]^{n-}$ (T = transition metal) have a great ability to activate various small molecules,[24-31] of which reactivity can vary depending on the electronic structure of the heteroatom in the heteroatom oxide core (μ_4O_x–X). For example, Fukuzumi and coworkers. have reported[27] on water oxidation by $[Ru^V(O)SiW_{11}O_{39}]^{5-}$ and $[Ru^V(O)GeW_{11}O_{39}]^{5-}$. They proposed that the high catalytic reactivity of $[Ru^V(O)GeW_{11}O_{39}]^{5-}$ is driven by the electron-withdrawing effect of the Ge atom. Su and coworkers later theoretically investigated the mechanism involved in this water oxidation reaction, where the activation energies in the case of both Si and Ge heteroatoms were calculated to be greater than 25 kcal/mol.[28] These experimental and theoretical reports suggest that the electron-withdrawing effect of heteroatoms enhances the catalytic reactivity of the water oxidation reaction.

Although $[Ru(O)XW_{11}O_{39}]^{n-}$ oxidizes water molecules in aqueous solution, in the chapter study, the Ru-substituted Keggin-type POM $[Ru^V(O)XM_{11}O_{39}]^{n-}$ ($3 \leq n \leq 6$)—specifically, $\mathbf{Ru^VO}\boldsymbol{X}$ (X = Al, Ga, Si, Ge, P, As, S; heteroatoms)—is proposed for a candidate catalyst for benzene hydroxylation in aqueous solution. This is because Ru^V=O species have a potential for catalyzing benzene hydroxylation reaction.[12] First, the reaction mechanism for benzene hydroxylation catalyzed by $\mathbf{Ru^VO}\boldsymbol{X}$ is investigated by performing density functional theory (DFT) calculations. The heteroatom effect should be considered if the activation energies for benzene hydroxylation by $\mathbf{Ru^VO}\boldsymbol{X}$ depend on the replacement of Si by X. To determine if the catalytic system is broadly applicable to aqueous solutions, water oxidation as a competitive reaction is also considered. Finally, the most efficient and outstanding catalyst for benzene hydroxylation in aqueous solution is proposed by calculating reaction rate ratio (r^B/r^W) between the reaction rate of benzene hydroxylation (r^B) and water oxidation (r^W).

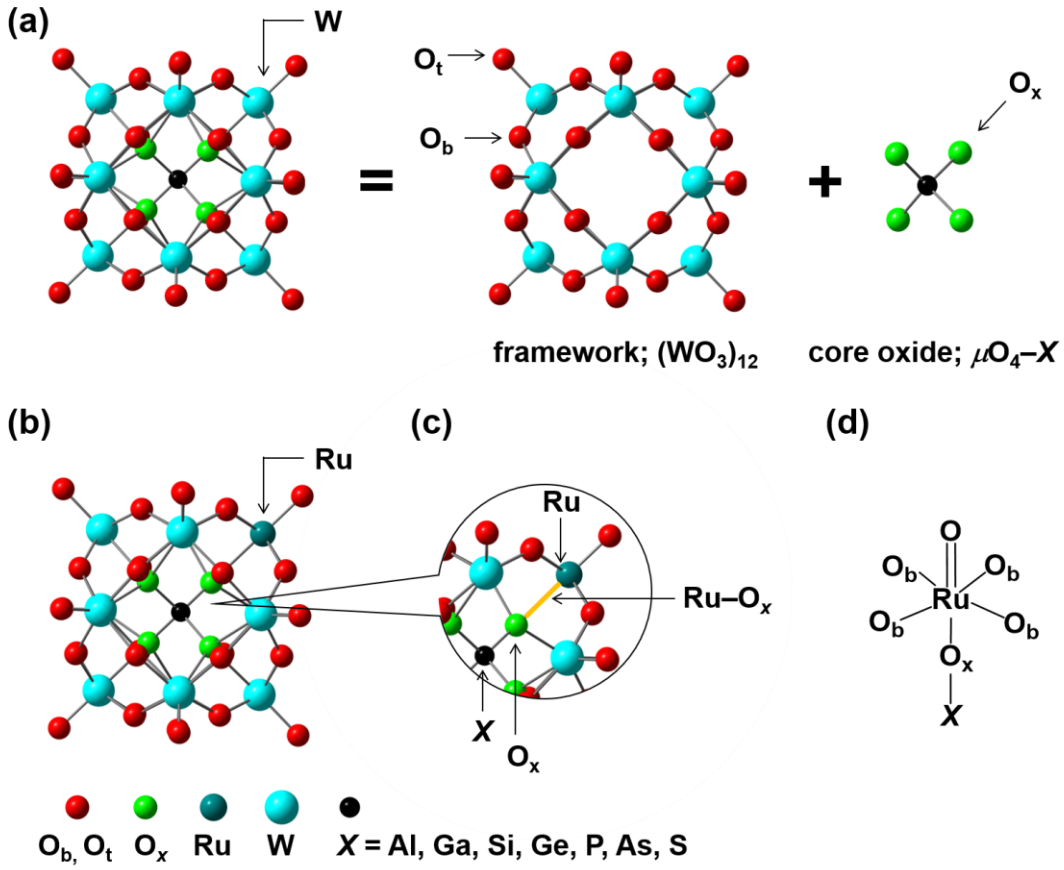

Figure 5-1. (a) A ball-and-stick model of Keggin-type polyoxometalates $[XW_{12}O_{40}]^{n-}$ (X = Al, Ga, Si, Ge, P, As, S). O_t, O_b, and O_x indicate oxygen in a terminal position, bridging two metal atoms, and composing μ_4O–*X*, respectively. (b) A computational model showing of $[Ru^V(O)XW_{11}O_{39}]^{5-}$ (X = Al, Ga, Si, Ge, P, As, S) and (c) its expansion. The O_b bonding W atoms being the nearest Ru site is omitted for clarity. (d) Schematic of the active center in $[Ru^V(O)XW_{11}O_{39}]^{n-}$.

5.2 Computational methodology

All optimized structures were obtained using B3LYP-D3 functional[33-36] as implemented in Gaussian 16 packages.[37] LanL2DZ[38] and 6-31G** basis set[39-41] were used for the W and the Ru atoms and the other atoms (H, C, O, Al, Si, P, S, Ga, Ge, and S), respectively. Implicit solvent effects with a dielectric constant of 78.36 were predicted by using the polarized continuum model.[42-45] Using the vibrational frequency analysis, we confirmed that the obtained local minima and transition state have none and one imaginary frequency, respectively. All energies include thermal and entropic correction at the temperature of 298.15 K. The value of a free energy of proton in aqueous solution was 270.3 kcal/mol.[46]

We calculated the reaction rate ratio (r^{B}/r^{W}) of each $\mathbf{Ru^{V}O}\boldsymbol{X}$ (X = Al, Ga, Si, Ge, P, As, and S) under ideal conditions by following equation[47]:

$$\frac{r^{B}}{r^{W}} = \frac{k^{B}[\mathbf{rc^{B}}]}{k^{W}[\mathbf{rc^{W}}]} = e^{\frac{-\Delta G_a}{RT}} \cdot \frac{[\mathbf{rc^{B}}]}{[\mathbf{rc^{W}}]} \qquad (5-1)$$

where R and T are gas constant and temperature, and ΔG_a (= $G_a^{B} - G_a^{W}$) is activation free energy difference between and benzene hydroxylation (G_a^{B}) and water oxidation (G_a^{W}) reactions. Here [$\mathbf{rc^{B}}$] ([$\mathbf{rc^{W}}$]) denotes the concentration of reactant complex in benzene hydroxylation ($\mathbf{rc^{B}}$) (water oxidation reaction ($\mathbf{rc^{W}}$)) and obtained following equation:

$$[\mathbf{rc^{B}}] = \cdot e^{\frac{-G(\mathbf{rc^{B}})}{RT}} \cdot [\mathbf{B}] \cdot [\mathbf{Ru^{V}O}\boldsymbol{X}] \qquad (5-2)$$

$$[\mathbf{rc^{W}}] = \cdot e^{\frac{-G(\mathbf{rc^{W}})}{RT}} \cdot [\mathbf{W}] \cdot [\mathbf{Ru^{V}O}\boldsymbol{X}] \qquad (5-3)$$

where $G(\mathbf{rc^{B}})$ and $G(\mathbf{rc^{W}})$ denote the free energy for $\mathbf{rc^{B}}$ and $\mathbf{rc^{W}}$, respectively, and [**B**] and [**W**] are molar concentration of benzene and water in aqueous solutions corresponding to 0.023 and 55.4 mol/L, respectively.[48] Herein the sum of $G(\mathbf{rc})$ and G_a leads to the energy in the transition state ($G^{\mathbf{ts}}$), as shown in Figure 5-2. Therefore, we obtained following equation:

$$\frac{r^{B}}{r^{W}} = \frac{k^{B}[\mathbf{rc^{B}}]}{k^{W}[\mathbf{rc^{W}}]} = \frac{e^{\frac{-G_a^{B}}{RT}}}{e^{\frac{-G_a^{W}}{RT}}} \cdot \frac{[\mathbf{rc^{B}}]}{[\mathbf{rc^{W}}]} = \frac{e^{\frac{-G_a^{B}}{RT}}}{e^{\frac{-G_a^{W}}{RT}}} \cdot \frac{e^{\frac{-G(\mathbf{rc^{B}})}{RT}}}{e^{\frac{-G(\mathbf{rc^{W}})}{RT}}} \cdot \frac{[\mathbf{B}]}{[\mathbf{W}]} = e^{\frac{-\Delta G^{\mathbf{ts}}}{RT}} \cdot \frac{[\mathbf{B}]}{[\mathbf{W}]} \qquad (5-4)$$

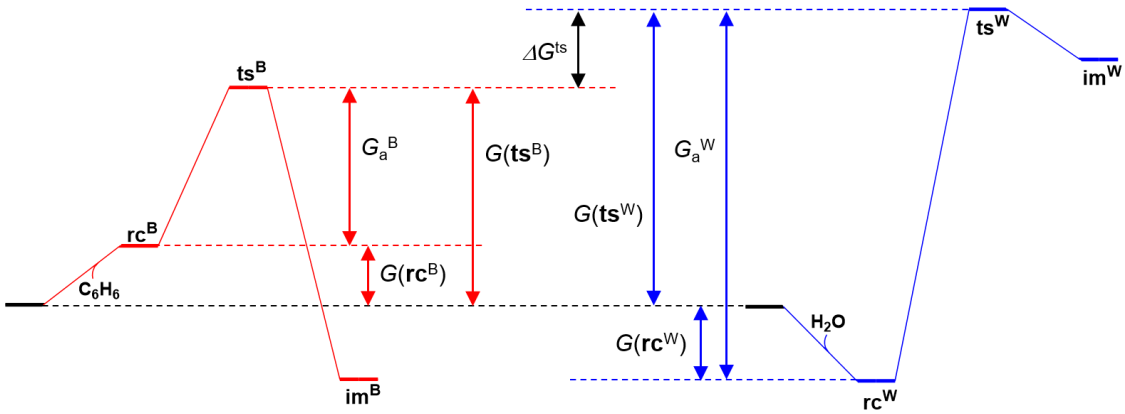

Figure 5-2. Schematic representation of the relationship of follow energies: $G(\mathbf{rc^{B}})$, $G(\mathbf{rc^{W}})$, $G(\mathbf{ts^{B}})$, $G(\mathbf{ts^{W}})$, G_a^{B}, and G_a^{W}.

5.3 Results and discussion

Figure 5-3 shows the catalytic cycles of benzene hydroxylation (B) and water oxidation (W). Using DFT calculations we investigate the reaction mechanism of C–O bond formation by reacting $\mathbf{Ru^{V}O}\boldsymbol{X}$ with a benzene molecule in benzene hydroxylation reaction and O–O bond formation by reacting $\mathbf{Ru^{V}O}\boldsymbol{X}$ with a H_2O molecule in the water oxidation reaction. Since both reactions have the formation of $\mathbf{Ru^{V}O}\boldsymbol{X}$ from aqua complex $[Ru^{III}(H_2O)XW_{11}O_{39}]^{n-}$ (**aq**) in common, we ignore this reaction to keep our discussions. Additionally, Fukuzumi and coworkers suggested[27] that the O–O bond formation by reacting $\mathbf{Ru^{V}O}\boldsymbol{X}$ with a H_2O molecule is the rate-determining step in the water oxidation reaction.

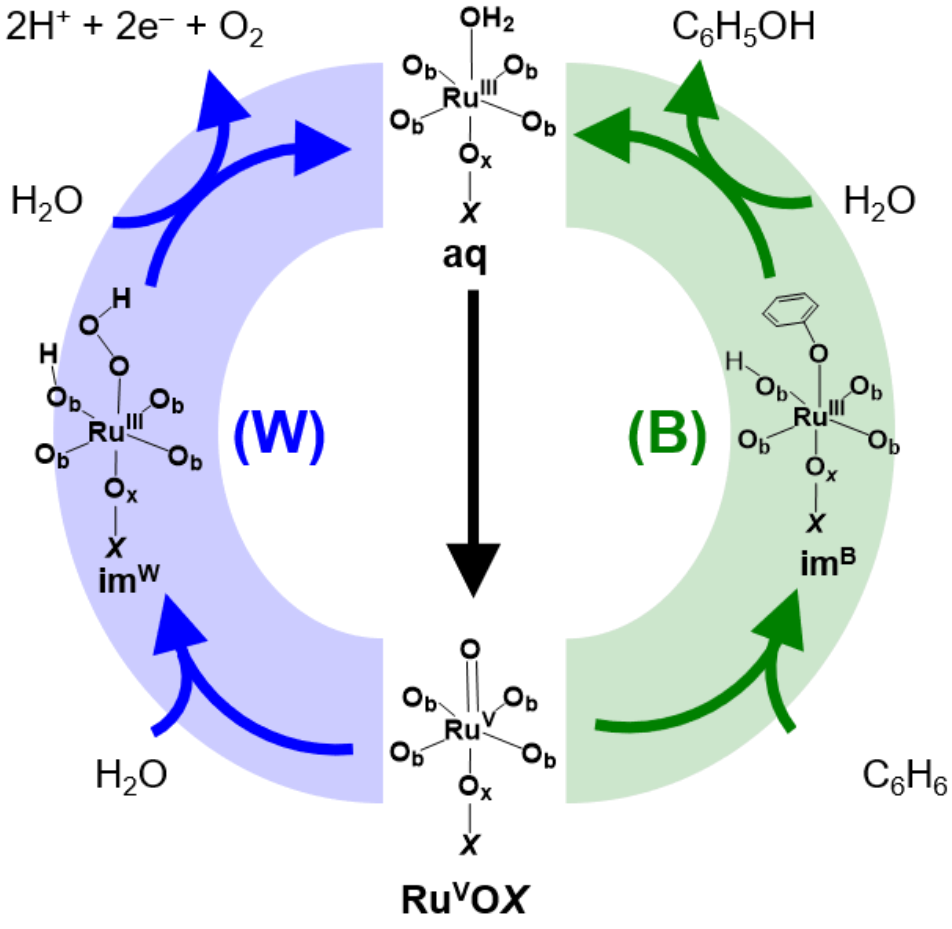

Figure 5-3. Schematic representation of catalytic cycles of benzene hydroxylation (B) and water oxidation (W), where **im** describe the intermediate.

5.3.2 Benzene hydroxylation by $Ru^{V}OX$

The molecular orbitals (MOs) of **$Ru^{V}OSi$** and their energies calculated in the doublet and quartet states are shown in Figure 5-4. Generally, in Ru^{V}=O species the Ru 4*d* orbitals interact with the O 2*p* orbitals to form three bonding (σ_{z^2}, π_{zx}, and π_{yz}), three antibonding (σ_{z^2}*, π_{zx}*, and π_{yz}*), and two nonbonding (δ_{xy} and $\delta_{x^2-y^2}$) orbitals.[49-52] In the doublet state there are doubly occupied of δ_{xy} and unoccupied π_{zx}*, and single occupied π_{yz}* orbitals. On the other hand, $\delta_{xy,}$ π_{zx}*, and π_{yz}* orbitals in quartet state are single occupied. Therefore, The electronic configurations of $(\delta_{xy})^{\alpha+\beta}(\pi_{zx}^*)^{\alpha}(\pi_{yz}^*)^{0}$ and $(\delta_{xy})^{\alpha}(\pi_{zx}^*)^{\alpha}(\pi_{yz}^*)^{\alpha}$ are assigned to quartet and doublet state, respectively. π_{zx}* and π_{yz}* orbitals in both multiplicities are orthogonal to each other. Moreover, in the quartet state highest the occupied molecular orbital (HOMO) in β spin (HOMO(β)) and lowest unoccupied molecular orbital (LUMO) in α spin (LUMO(α)) consists of O 2*p* and W 5*d* orbitals, respectively, assigned to HOMO and LUMO of WO_3.[53] Interestingly, both α and β δ_{xy}, π_{zx}*, and π_{yz}* orbitals lie between HOMO(β) and LUMO(α). These electronic structures can also be observed in the replacement of Si to X.

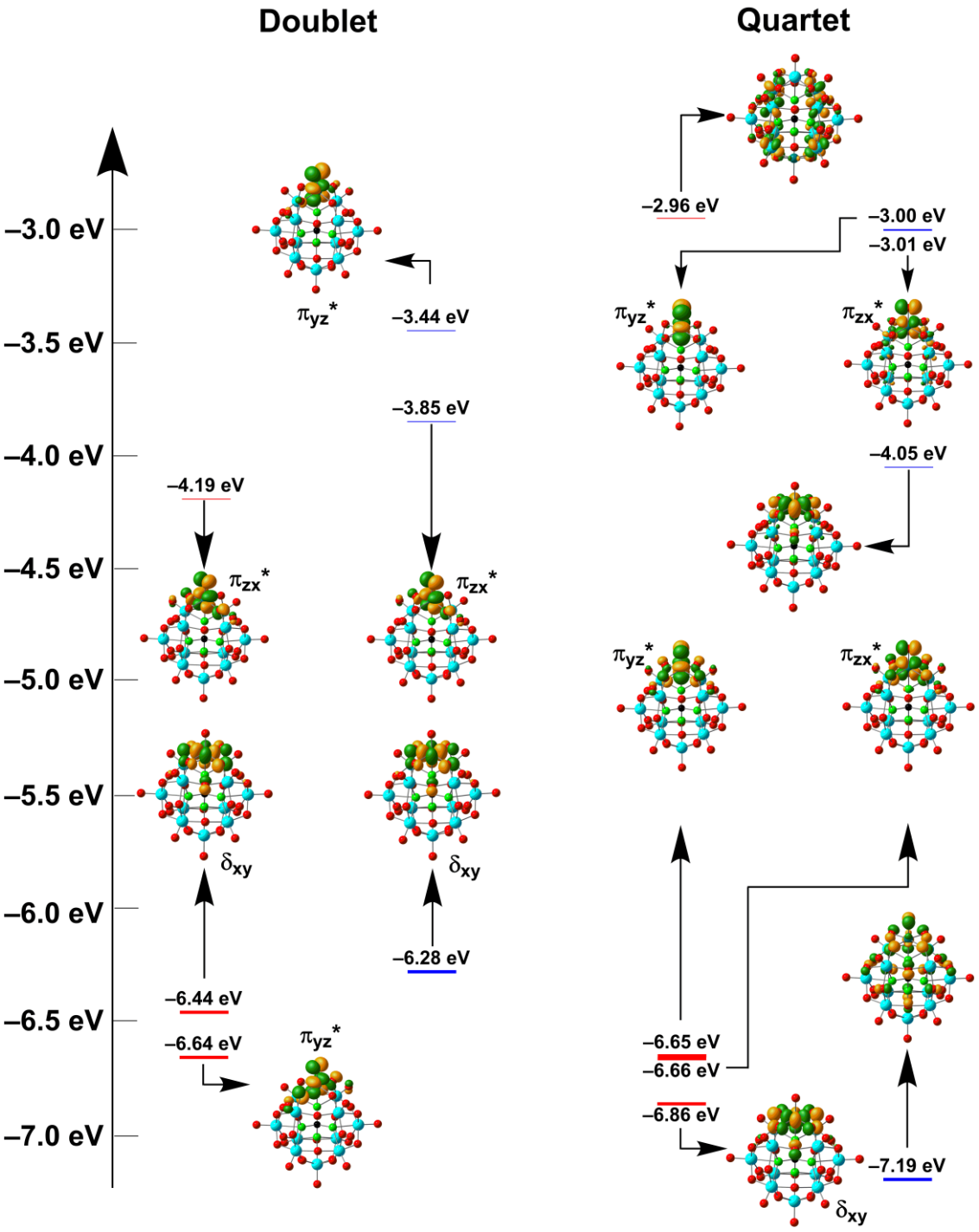

Figure 5-4. Molecular orbitals of **Ru^{V}OSi** in the doublet (left) and quartet(right) states. Red and blue lines indicate the α and β spin orbital, respectively. Bold lines indicate the occupied orbitals. Each subscript describes the origin of each orbital involving the Ru 4*d* orbitals. The z-axis is oriented parallel to the axis of Ir=O. Note that x and y are arbitrary. Isovalue is 0.05.

5.3.2 Benzene hydroxylation by $Ru^{V}O$*X*

We first consider the computed reaction pathway for benzene hydroxylation catalyzed by **Ru^{V}OSi** as the case of *X* = Si. In general, benzene hydroxylation by metal–oxo species involves an oxygen-insertion mechanism and a radical mechanism.[54-56] Generally, the radical mechanism requires rather high energy sue to the unstable of benzene radical ($^{\bullet}C_6H_5$). Thus, the present work is limited to the oxygen insertion mechanism, as shown in Figure 5-5. Benzene hydroxylation proceeds in the doublet and the quartet states. The quartet state in the initial complex (**Ru^{V}OSi**) and in the reactant complex (**rc^{B}**) is the ground state, whereas the double state lies below the quartet state in the transition state (**ts^{B}**), the intermediate (**im^{B}**). Therefore, spin inversion is likely to occur in **Ru^{V}OSi** or **rc^{B}**. The spin inversion in **Ru^{V}OSi** requires only 7.5 kcal/mol. The first step is initiated by the formation of **rc^{B}**, where the distance between the proximal C in benzene and the O in Ru^{V}=O species is 3.31 Å in the doublet state. Due to the entropic effect, the formation of **rc^{B}** is endothermic reaction of 3.0 and 1.8 kcal/mol in the quartet and doublet states, respectively. Mulliken spin population of Ru^{V}=O species in **$^{2}rc^{B}$** is 1.01 $e^{-}/Å^{3}$. The C–O bond formation between the benzene and **Ru^{V}OSi** moieties occurs with activation free energies of 13.5 kcal/mol in the doublet state and 24.3 kcal/mol in the quartet state. Based on Mulliken spin population analysis, we found that Mulliken spin population of Ru^{V}=O species and C_6H_6 moiety is respectively 1.31 and –0.51 $e^{-}/Å^{3}$, indicating the electron transfer from benzene to Ru^{V}=O species. Therefore, we can assign the reaction mechanism of C–O bond formation to electrophilic aromatic substitution, where a benzene π orbital interacts with a π* unoccupied orbital (LUMO) in Ru^{V}=O species. Following C–O bond formation, H atom migration is responsible for the formation of phenolate ($C_6H_5O^{-}$) coordinated to the Ru atom. Because the proton transfer from the O_b to the O atom phenolate requires rather high activation free energy, phenol is produced by the proton adsorption from solvent, with the exothermic reaction of 2.3 kcal/mol. Finally, **pch^{B}** undergoes ligand exchange to form **aq** and phenol with a deprotonation of O_b, where the final step requires only 8.2 kcal/mol. Consequently, benzene hydroxylation by **Ru^{V}OSi** is computed to be an exergonic reaction by 30.6 kcal/mol.

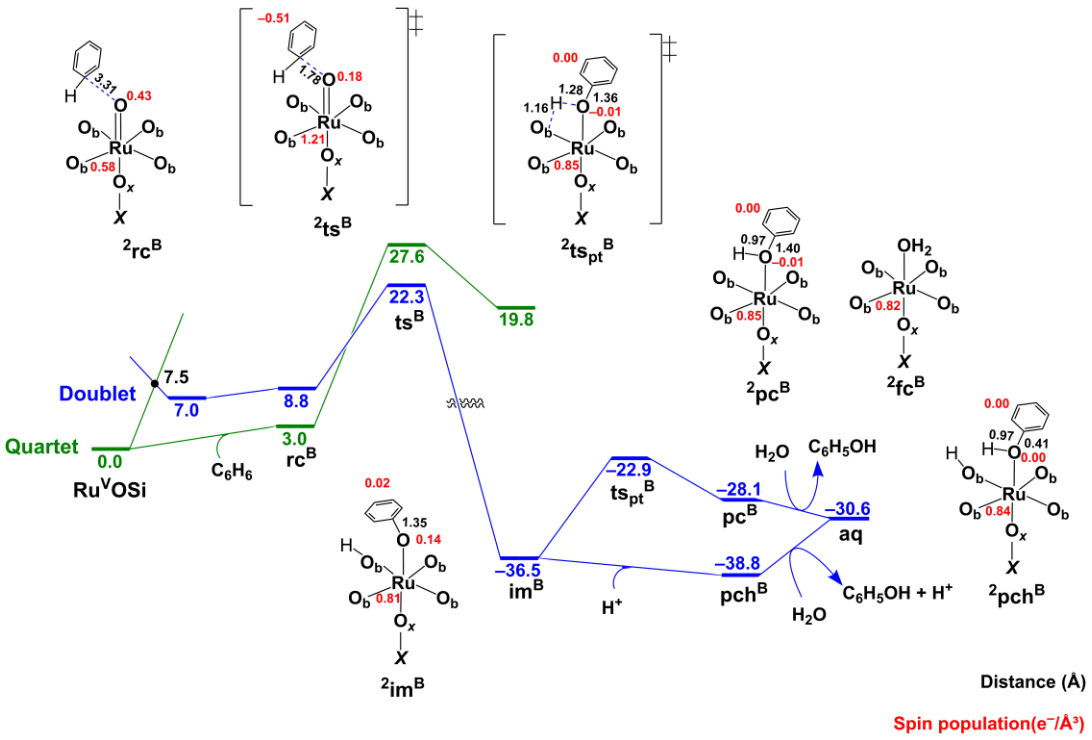

Figure 5-5. Computed free energy diagrams for benzene hydroxylation by **Ru^{V}OSi** in the doublet and quartet states. All energies are measured from the dissociation limit between the initial complex (**Ru^{V}OSi**) and an isolated benzene molecule in the quartet state and are reported in kcal/mol. Black and red characters indicate the bond length and the spin populations in Ru and O atoms, respectively.

We next focus on the heteroatom effects for benzene hydroxylation by **Ru^{V}O*X***. Eda and coworkers have reported[20-22] a heteroatom effect for the electron redox potential on the Keggin-type polyoxometalate $[XO_4W_{12}O_{36}]^{n-}$ (X = B, Al, Ga, Si, Ge, P, As), who demonstrated a correlation between the orbital energy levels and the bond length in μ_4O–X. On the basis of their previous studies, a heteroatom effect in benzene hydroxylation by **Ru^{V}O*X*** (X = Al, Ga, Si, Ge, P, As, S) can be expect because the reactivity for the electrophilic reaction depends on the energy level of the LUMO in the catalyst. The replacement of Si by X induces changes in the bond length in μ_4O–X. Note that the geometry of the tungsten oxide framework remains unchanged. It is expected that the bond length of Ru–O_x would be controlled by changes of the μ_4O–X bond. To explain the heteroatom effect, the Ru–O_x distance of 2.28 Å in **Ru^{V}OSi** as a standard reference are used. As a result of the replacement of Si by X (see Table 5-1), the distance in Ru–O_x bond is decreased to 2.22 Å in **Ru^{V}OGe**, 2.14 Å in **Ru^{V}OGa**, and 2.18 Å in **Ru^{V}OAl**, whereas the Ru–O_x distances in the case of the other three hetero atoms increased

(2.29 Å in **Ru^{V}OAs**, 2.34 Å in **Ru^{V}OP**, and 2.46 Å in **Ru^{V}OS**). Additionally, there is a good linear correlation (R^2 = 0.87) exists between the distance in Ru–O_x and the LUMO energy (Figure 5-6(a)). This is because the σ, π, σ*, and π* orbitals are stabilized as the elongation of Ru–O_x distance, whereas that orbitals are destabilized due to the shorten of Ru–O_x distance (see Figure 5-6(b)).

Given such discussions, the activation free energy of benzene hydroxylation by **Ru^{V}O*X*** are investigated. Note that the reaction mechanism in the replacement of other heteroatoms is the same as in **Ru^{V}OSi**. The activation free energy for **ts^{B}** also exhibits a substantial substituent dependence. In the lengthened Ru–O_x bond group the activation free energies increase from 13.5 kcal/mol to 15.2 kcal/mol in **Ru^{V}OAl** and 14.8 kcal/mol in **Ru^{V}OGa**; the activation free energy of 13.0 kcal/mol in **Ru^{V}OGe** is approximately the same (see Table 5-1). In the shortened Ru–O_x bond group, on the other hand, the activation free energies decrease to 10.7 kcal/mol in **Ru^{V}OP**, 10.7 kcal/mol in **Ru^{V}OAs**, and 10.3 kcal/mol in **Ru^{V}OS** (see Table 5-1). These results can be explained by the qualitative fact that the replacement of *X* (shortened Ru–O_x bond group) increases the orbital interaction between the highest occupied molecular orbital (HOMO) of the benzene moiety (occupied π orbital) and the LUMO of the Ru^{V}=O species.

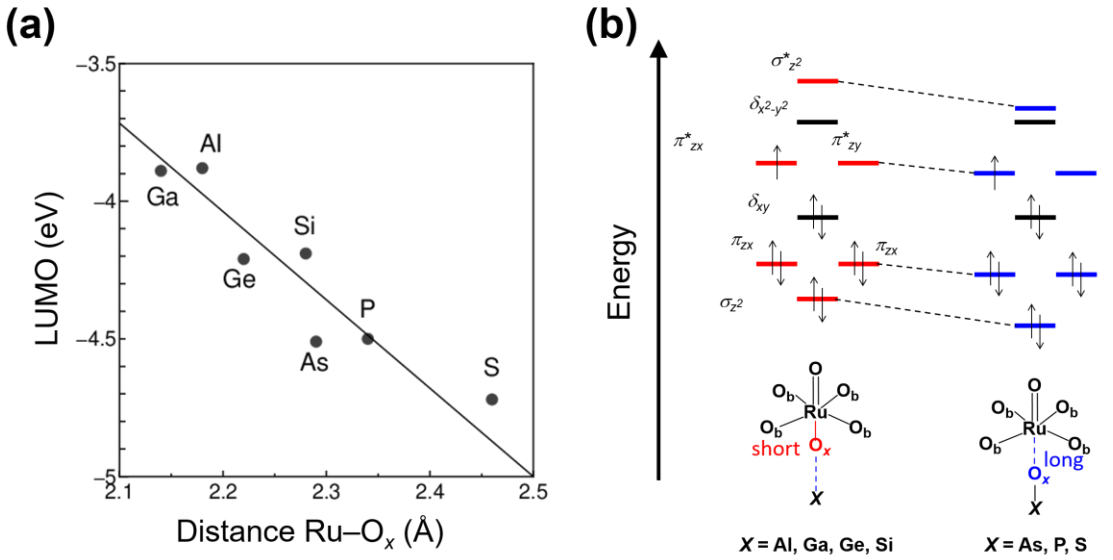

Figure 5-6. Distance in Ru–O_x versus the unoccupied π* orbital energy (R^2 = 0.87) and (b) Energy levels of molecular orbitals show dependencies on the *X* atom through the interaction with the O_x atom.

5.3.3 O–O bond formation reaction by reacting $Ru^{V}O\mathit{X}$ with H_2O

Having established the reaction mechanism and heteroatom effect of benzene hydroxylation, we next discuss about the O–O bond formation, which is the rate-determining step of water oxidation reaction. Figure 5-7 shows the computed energy diagrams for the O–O bond formation by reaction **$Ru^{V}OSi$** with a H_2O molecule as the case of X = Si. Since the O–O bond formation tales place in the doublet state, the spin inversion is first occurred similar to the benzene hydroxylation reaction. The adsorption of a H_2O molecules for **$Ru^{V}OSi$** give rise to **rc^{w}**, where the distances in O···O and O···H are 3.23 and 2.21 Å, respectively. Contrary to the formation of **rc^{B}**, the formation of **rc^{W}** is exothermic reaction of 2.8 kcal/mol due to the Coulomb interaction between H atom in H_2O and O_b. The activation free energy is calculated to be 26.7 kcal/mol, which is consistent with previous study by Su and coworkers.[28] In **ts^{W}** the spin population of O atom in H_2O moiety and in Ru^{V}=O species is respectively –0.42 and 0.33 $e^{-}/Å^{3}$, indicating that the O–O bond formation does not undergo water nucleophilic attack (WNA) mechanism but radical coupling mechanism.[57,58]

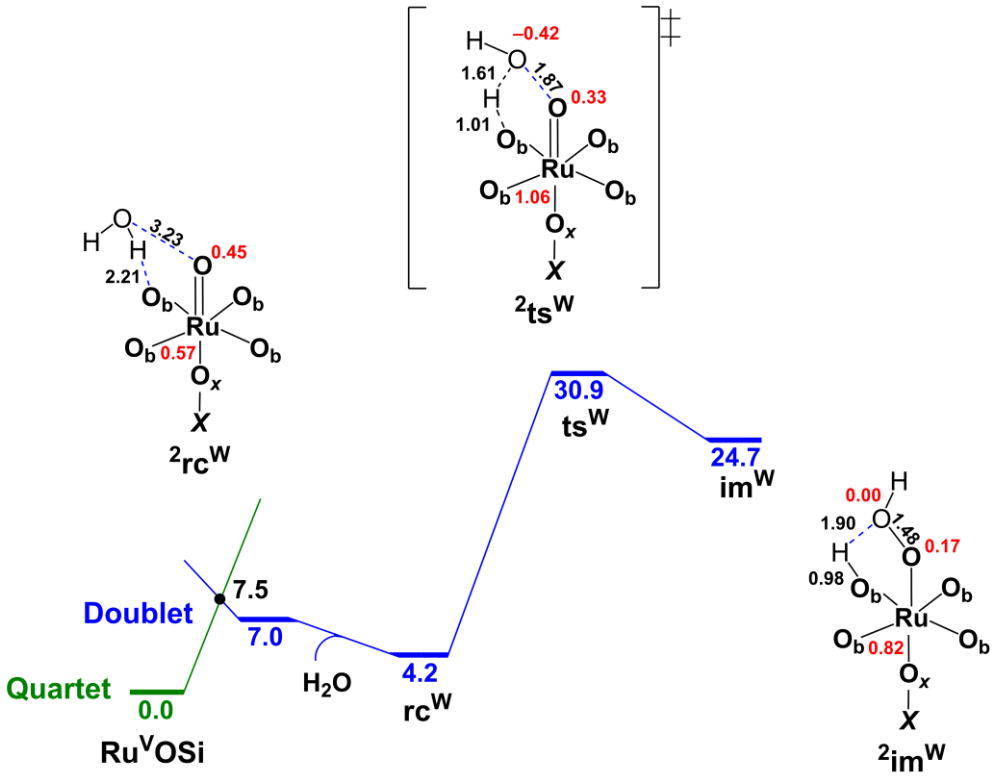

Figure 5-7. Computed free energy diagrams for water oxidation undergoing O–O bond formation in the doublet state. All energies are measured from **$Ru^{V}OSi$** in the quartet state and in kcal/mol. Black and red figures indicate bond length of O···O and spin densities in Ru and O atoms, respectively.

In order to clarify the O–O bond formation mechanism, partial optimization is performed with a fixed of O–O distance between H_2O and Ru^V=O species (O atom in H_2O describe O_w later) Figure 5-8 shows the plot of spin densities of Ru^V=O species (black line) and O_w (clue line) against horizontal axis O–O_w distance. This calculation shows that spin population in Ru^V=O species (O_w) is significantly increased (decreased) at 2.075 Å of O–O_w distance. Here, the H atom in H_2O moiety migrate to O_b at the same time (Figure 5-8). These electronic and geometrical changes show the proton-coupled electron transfer (PCET),[59-60] where the proton and electron transfer from H_2O moiety to O_b and Ru^V=O species in **Ru^VOSi**, respectively.

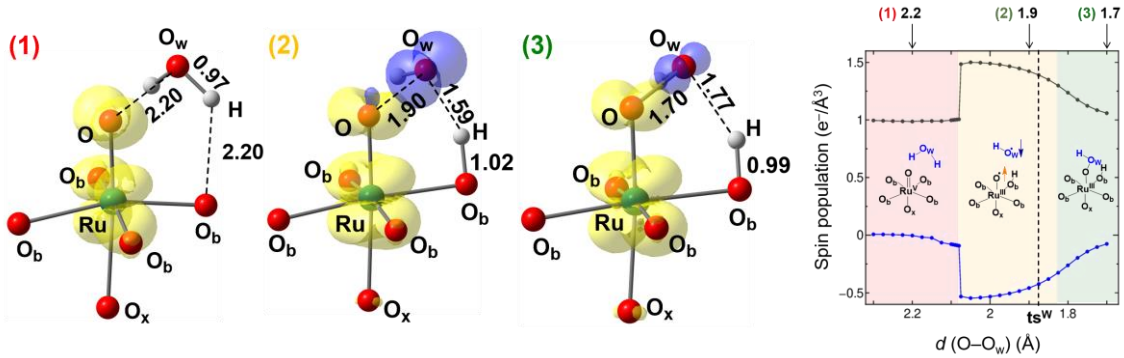

Figure 5-8. (Top) Isosurface of spin densities ($\rho_\alpha - \rho_\beta$) at d = 2.200 Å, 1.900 Å, and 1.700 Å, where d denotes the O–O_w distance. Yellow and blue isosurfaces (isovalue = 0.0075) indicate positive and negative regions, respectively. (Bottom) Spin densities of the Ru^V=O moiety (black) and the O atom in the H_2O moiety (blue) plotted as a function of d (Å).

We can reasonably expect that the effect of heteroatoms in water oxidation is similar to that in benzene hydroxylation. In fact, the replacement of Si by *X* changes the electronic structures of the O_b site in the tungsten oxide framework. Fukuzumi and coworkers proposed[27] that an electron-withdrawing effect improves the reactivity of the water oxidation reaction, which can be paraphrased as an "electronic push–pull effect." Their experimental observations are consistent with the present DFT calculation results. Indeed, the activation free energies for the water oxidation reaction were calculated to be 26.4 kcal/mol for **Ru^VOGe** and 26.7 kcal/mol for **Ru^VOSi**. This result is also consistent with the previous study reported by su and coworkers.[28] However, the energy difference in this study is only 0.3 kcal/mol. Although we cannot ignore the substituent dependence on the basis of the heteroatom effect in water

oxidation, present systematic calculations suggest that the activation free energies for the rate-determining step in water oxidation by $\mathbf{Ru^{V}O}\boldsymbol{X}$ do not substantially differ from those for the rate-determining step in benzene hydroxylation by $\mathbf{Ru^{V}O}\boldsymbol{X}$ (see Table 5-1). Indeed, Meyer and coworkers have also pointed out the possibility that a decrease in the activation free energy for the water oxidation reaction through PCET mechanism is enhanced more by the addition of a base with a higher $p\mathrm{K_a}$ than by a change in the electronic structure of the axial ligand.[61] Herein $\mathrm{O_b}$ act as a proton acceptor, but the electronic structure of $\mathrm{O_b}$ insignificantly change by the replacement of *X*. These DFT calculations lead us to the conclusions that the replacement of *X* does not affect the activation free energy for O–O bond formation reaction in $\mathbf{Ru^{V}O}\boldsymbol{X}$.

5.3.4 Reaction rate ratio based on the transition state theory

Finally, we consider the reaction rate ratio between the benzene hydroxylation and water oxidation reactions ($r^{\mathrm{B}}/r^{\mathrm{W}}$). This value can be regarded as the branching ratio of the reaction with benzene in aqueous solution. We can expect with above discussions about both reaction mechanism and heteroatom substituent effect in mind discussion that the activation free energy difference ΔG_{a} (= $G_{\mathrm{a}}^{\mathrm{B}} - G_{\mathrm{a}}^{\mathrm{W}}$) between benzene hydroxylation ($G_{\mathrm{a}}^{\mathrm{B}}$) and water oxidation ($G_{\mathrm{a}}^{\mathrm{W}}$) reactions is varied as the replacement of *X*. Thus, to estimate values of $r^{\mathrm{B}}/r^{\mathrm{W}}$ can help us predict the high-performance catalyst performing benzene hydroxylation reaction in aqueous solution even low concentration of benzene in aqueous solution. The reaction rate ratio is obtained using the Arrhenius-like equation Eq.5–4, the free energy difference $\Delta G^{\mathrm{ts}} = G(\mathbf{ts^{W}}) - G(\mathbf{ts^{B}})$, and the molar concentration of benzene [B] and water [W] in aqueous solutions, where $G(\mathbf{ts^{W}})$ and $G(\mathbf{ts^{B}})$ are relative energies of the transition states for the benzene hydroxylation reaction and water oxidation reaction, respectively (see **5.2 Computational method**). A large ΔG^{ts} gives a large $r^{\mathrm{B}}/r^{\mathrm{W}}$ corresponding to a high-performance catalyst toward benzene hydroxylation in aqueous solution. Interestingly, there is a good linear correlation ($R^2 = 0.91$) between $\log(r^{\mathrm{B}}/r^{\mathrm{W}})$ and the Ru–O_x distance in Figure 5-9. The calculated $r^{\mathrm{B}}/r^{\mathrm{W}}$ values lead to the conclusion that $\mathbf{Ru^{V}OS}$ ($[\mathrm{Ru^{V}(O)SW_{11}O_{39}}]^{3-}$) is a candidate catalyst for the benzene hydroxylation reaction in aqueous solution. Addtionally, these computed results indicate that the $\mathrm{Ru^{V}{=}O}$ species can be extended to other metal–oxo species such as the benzene hydroxylation reaction involving a Co-substituted Keggin-type polyoxometalate catalyst reported by Shimomura et al.[62]

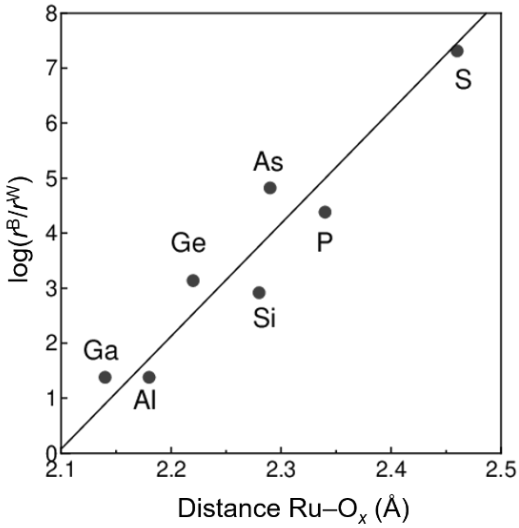

Figure 5-9. Correlation of the Ru–Ox distance and the reaction rate ratio between benzene hydroxylation and water oxidation (r^B/r^W).

5.4 Conclusions

In this chapter the benzene hydroxylation catalyst (**Ru^{V}O*X***) in aqueous solution are proposed. The benzene hydroxylation reaction proceeds through an oxygen insertion mechanism (i.e., an electrophilic aromatic substitution reaction), whereas the water oxidation reaction involving O–O bond formation proceeds through a proton-coupled electron transfer mechanism. The activation free energy for benzene oxidation strongly depends on the energy level of the LUMO in the Ru^V=O species. In contrast to the activation free energy for the benzene hydroxylation reaction, that for the water oxidation reaction shows no substantial heteroatom effect. Calculated reaction rate ration between benzene hydroxylation and O–O bond formation obtained using the Arrhenius-like equation shows that the benzene hydroxylation selectivity in aqueous solution increased with lengthening of bond distance in Ru–O_x, which controls the energy levels of the LUMO in Ru^V=O species. This effect is not driven by an "electronic push–pull effect" but by a "geometrical push–pull effect" through the interaction between the heteroatom and the O_x atom. DFT calculations suggest that $[Ru^V(O)SW_{11}O_{39}]^{3-}$ is a high-performance benzene hydroxylation catalyst with high reactivity and high chemoselectivity in aqueous solution.

Reference

1. Weiss, J. M.; Downs, C. R. Catalytic Oxidation of Benezene to Maleic Acid. *J. Chem. Educ*. **1925**, *2*, 1178–1180.
2. Davico, G. E.; Bierbaum, V. M.; DePuy, C. H.; Ellison, G. B.; Squires, R. The C–H bond Energy of Benzene. *J. Am. Chem. Soc.* **1995**, *117*, 2590–2599.
3. He, C.; Li, J.; Cheng, J.; Li, L.; Li, P.; Hao, Z.; Xu, Z. P. Comparative Studies on Porous Material-Supported Pd Catalysts for Catalytic Oxidation of Benzene, Toluene, and Ethyl Acetate. *Ind. Eng. Chem. Res.* **2009**, *48*, 6930–6936.
4. Hock, H., Lang, S. Autoxydation von Kohlenwassertoffen, IX, Mitteil.: Über Peroyde von Benzol-Derivaten. *Ber. Dtsch. Chem. Ges.* **1944**, *77*, 257–264.
5. Turton, R.; Bailie, R. C.; Whiting, W. B.; Shaelwitz, J. A. *Analysus, Synthesis and Design of Chemical Processes*, "2nd Ed.; Prentice Hall: Upper Saddle River, NJ, 2003.
6. Sono, M.; Roach, M. P.; Coulter, E. D.; Dawsin, J. H. Heme-Containing Oxygenase. *Chem. Rev.* **1996**, *96*, 2841–2888.
7. Solomon, E. I.; Sundaram, U. M.; Machonkin, T. E. Multicopper Oxidases and Oxygenases. *Chem. Rev.* **1996**, *96*, 2563–2606.
8. Liang, Y.; Wei, J.; Qiu, X.; Jiao, N. Homogeneous Oxygenase Catalysis *Chem. Rev.* **2018**, *118*, 4912–4945.
9. Gunay, A.; Theopold, K. H. C–H Bond Activations by Metal Oxo Compounds. *Chem. Rev.* **2010**, *110*, 1060–1081.
10. Morimoto, Y.; Bunno, S.; Fujieda, N.; Sugimoto, H. Itoh, S. Direct Hydroxylation of Benzene to Phenol Using Hydrogen Peroxode Catalyzed by Nickel Complexes Supported by Pyridylalkylamine Ligands. *J. Am. Chem. Soc.* **2020**, *137*, 5867–5870.
11. Tsuji, T.; Zaoputra, A. A.; Hitomi, Y.; Mieda, K.; Ogura, T.; Shiota, Y.; Yoshizawa, K.; Sato, H.; Kodera, S. Specific Enhancement of Catalytic Activity by a Dicopper Core: Selective Hydroxylation of Benzene to Phenol with Hydrogen Peroxide. *Angew. Chem. Int. Ed.*, **2017**, *56*, 7779–7782.
12. Shimoyama, Y.; Ishizuka, T.; Kotani, H.; Kojima, T. Catalytic Oxidation Cracking of Benzene Rings in Water. *ACS Catal*. **2019**, *9*, 671−678.

13. Shimoyama, Y.; Tamura, S.; Kitagawa, Y.; Hong, D.; Kon, Y. A Cobalt-Substituted Keggin-Type Polyoxometalate for Catalysis of Oxidative Aromatic Cracking Reactions in Water. *Catal*. *Sci*. *Technol.* **2020**, *10*, 8042−8048.

14. Farahmand, S.; Ghiaci, M.; Vatanparast, M.; Razavizadeh, J. S. One-Step Hydroxylation of Benzene to Phenol Over Schiff Base Complexes Incorporated onto Mesoporous Organosilica in the Presence of Different Axial Ligands. *New J. Chem.* **2020**, *44*, 7517–7527.

15. Anandababu, K.; Muthuramalingam, S. Velusamy, M.; Mayilmurugan, R. Single-Step Benzene Hydroxylation by Cobalt(II) Catalysts *via* a Cobalt(III)-Hydroperoxo Intermediate. *Catal. Sci. Technol.* **2020**, *10*, 2540–2548.

16. Coronado, E.; Gomez-Garcia. Polyoxometalate-Based Molecular Materials. *Chem. Rev.* **1998**, *98*, 273–296.

17. Gouzerh, P.; Proust, A. Main-Grpup Element, Organic, and Organometallic Derivatives of Polyoxometalates. *Chem. Rev.* **1998**. *98*, 77–111.

18. Lȯpez, X.; Carbȯ, J. J.; Bo, C.; Poblet, J. M. Structure, Properties and Reactivity of Polyoxometalates: A Theoretical Perspective. *Chem. So. Rev.* **2012**, *41*, 7537–7571.

19. Himeno, S.; Takamoto, M.; Santo, R.; Ichimura, A. Redox Properties and Basicity of Keggin-Type Polyoxometalate Complexes. *Bull. Chem. Soc. Jpn.* **2005**, *78*, 95–100.

20. Nakajima, K.; Eda, K.; Himeno, S. Effect of the Central Oxoanion Size on the Voltammetric Properties of Keggin-Type $[XW_{12}O_{40}]^{n-}$ (n = 2–6) Complexes. *Inorg. Chem.* **2010**, *49*, 5212–5215.

21. Takazaki, A.; Eda, K.; Osakai, T.; Nakajima, T. Can Electron-Rich Oxygen (O^{2-}) Withdraw Electrons from Metak Centers? A DFT Study on Oxoanion-Caged Polyoxometalates. *J. Phys. Chem. C* **2017**, *121*, 7684–7689.

22. Takazaki, A.; Eda, K.; Osakai, T.; Nakajima, T. Quantum Chemical Study on the Multi-Electron Transfer of Keggin-type Polyoxotungstate Anions: The Relation of Redox Potential to the Bond Valence of μ_4O–W. *J. Comput. Chem. Jpn.* **2017**, *16*, 93–95.

23. Azuma, S.; Kadoguchi, T.; Eguchi, Y.; Hirabaru, H.; Ota, H.; Sadakane, M.; Yanagisawa, K.; Hasegawa, K.; Ueda T. Metal-Substituted Tungstosulfates with Keggin Structure: Synthesis and Characterization. *Dalton Trans.* **2020**, *49*, 2766–2770.

24. Geletii, Y. V.; Botar, B.; Kögerler, P.; Hillesheim, D. A.; Musaev, D. G.; Hill, C. L. An All-Inorganic, Stable, and Highly Active Tetraruthenium Homogeneous Catalyst for Water Oxidation *Angew. Chem. Int. Ed.* **2008**, *47*, 3896–3899.

25. Sartorel, A.; Carraro, M.; Scorrano, G.; Zorzi, R. D.; Geremia, S.; MaDaniel, N. D.; Bernhard, S.; Bonchio, M. Polyoxometalate Embedding of a Tetraruthenium(IV)-oxo-core by Template-Directed Metalation of [□-$SiW_{10}O_{36}$]$^{8-}$: A Totally Inorganic Oxygen-Evolving Catalyst. *J. Am. Chem. Soc.* **2008**, *130*, 5006–5007.

26. Geletii, Y. V.; Besson, C.; Hou, Y.; Yin, Q.; Musaev, D. G.; Quiñonero, D.; Cao, R.; Hardcastle, K. I.; Proust, A.; Kögerler, P.; Hill, C. L, Structural, Physicochemical, and Reactivity Properties of an All-Inorganic, Highly Active Tetraruthenium Homogeneous Catalyst for Water Oxidation. *J. Am. Chem. Soc.* **2009**, *131*, 17360–17370.

27. Murakami, M.; Hong, D.; Suenobu, T.; Yamaguchi, S.; Ogura, T.; Fukuzumi, S. Catalytic Mechanism of Water Oxidation with Single-Site Ruthenium–Heteropolytungstate Complexes. *J. Am. Chem. Soc.* **2011**, *133*, 11605–11613.

28. Lang, Z.-L.; Yang, G.- C.; Ma, N.-N. When, S.-Z.; Yan, L.-K.; Guan, W.; Su, Z.-M. DFT Characterization on the Mechanism of Water Splitting Catalyzed by Single-Ru-Substituted Polyoxometalates. *Dalton Trans.* **2013**, *42*, 10617– 10625.

29. Berats-Damatov, D.; Shimon, L. J. W.; Weiner, L.; Schreiber, R. E.; Jiménez-Lozano, P.; Poblet, J. M.; de Graaf, C.; Neumann, R. Dicobalt-□-oxo Polyoxometalate Compound, [(α_2-$P_2W_{17}O_{61}Co)_2O$]$^{14-}$: A potent Species for Water Oxidation, C–H Bond Activation, and Oxygen Transfer. *Inorg. Chem.* **2014**, *53*, 1779–1787.

30. Liang, M.-X.; Liu, C.-G. Reduction of NO to N_2O Catalyzed by a Mn-Substituted Keggin-Type Polyoxometalate: A Density Functional Theory Study. *J. Phys. Chem. C* **2017**, *121*, 12735–12744.

31. Chu, Y.-J.; Chen, X.-M.; Liu, C.-G. Computational Study on Epoxidation of Propylene by Dioxygen Using the Silanol-Functionalized Polyoxometalate-Supported Osmium Oxide Catalyst. *Inorg. Chem. Front.* **2019**, *6*, 3482–3492.

32. Su, X.-F.; Yan, L.-K.; Su, Z.-M. Theoretical Insight into the Performance of $Mn^{II/III}$-Monosubstituted Heteropolytungstates as Water Oxidation Catalysts. *Inorg. Chem.* **2019**, *58*, 15751–15757.

33. Becke, A. D. Density-Functional Exchange-Energy Approximation with Correct Asymptotic Behavior. *Phys. Rev. A*, **1988**, *38* 3098−3100.

34. Lee, C.; Yang, W.; Parr. R. G. Development of the Colle-Salvetti Correlation-Energy Formula into a Functional of the Electron Density. *Phys. Rev. B*, **1988**, *37*, 785−789.

35. Becke, A. D. Density-Functional Thermochemistry. III. The Role of Exact Exchange. *J. Chem. Phys.*, **1993**, *98*, 1372−1377.

36. Grimme, S.; Antony, J.; Ehrlich S.; Krieg H. A Consistent and Accurate *ab initio* Parametrization of Density Functional Dispersion Correction (DFT-D) for the 94 Elements H-Pu. *J. Chem. Phys.*, **2010**, *132*, 154104.

37. Frisch, M. J.; Trucks, G. W.; Schlegel, H. B.; Scuseria, G. E.; Robb, M. A.; Cheeseman, J. R.; Scalmani, G.; Barone, V.; Petersson, G. A.; Nakatsuji, H.; Li, X.; Caricato, M.; Marenich, A. V.; Bloino, J.; Janesko, B. G.; Gomperts, R.; Mennucci, B.; Hratchian, H. P.; Ortiz, J. V.; Izmaylov, A. F.; Sonnenberg, J. L.; Williams-Young, D.; Ding, F.; Lipparini, F.; Egidi, F.; Goings, J.; Peng, B.; Petrone, A.; Henderson, T.; Ranasinghe, D.; Zakrzewski, V. G.; Gao, J.; Rega, N.; Zheng, G.; Liang, W.; Hada, M.; Ehara, M.; Toyota, K.; Fukuda, R.; Hasegawa, J.; Ishida, M.; Nakajima, T.; Honda, Y.; Kitao, O.; Nakai, H.; Vreven, T.; Throssell, K.; Montgomery, J. A., Jr.; Peralta, J. E.; Ogliaro, F.; Bearpark, M. J.; Heyd, J. J.; Brothers, E. N.; Kudin, K. N.; Staroverov, V. N.; Keith, T. A.; Kobayashi, R.; Normand, J.; Raghavachari, K.; Rendell, A. P.; Burant, J. C.; Iyengar, S. S.; Tomasi, J.; Cossi, M.; Millam, J. M.; Klene, M.; Adamo, C.; Cammi, R.; Ochterski, J. W.; Martin, R. L.; Morokuma, K.; Farkas, O.; Foresman, J. B.; Fox, D. J. *Gaussian 16*, Revision A. 03; Gaussian, Inc.: Wallingford ,CT, 2016.

38. Hay P. J.; Wadt, W. R. Ab initio effective core potentials for molecular calculations – potentials for the transition–metal atoms Sc to Hg. *J. Chem. Phys.* **1985**, *82*, 270−283.

39. Francl, M. M.; Pietro, W. J.; Hehre, W. J.; Binkley, J. S.; Gordon, M. S.; Defrees D. J.; Pople, J. A. Self-Consistent Molecular Orbital Methods. 23. A polarization-type basis set for 2nd-row elements *J. Chem. Phys.* **1982**, *77*, 3654−3655.

40. Hariharan, P. C.: Pople, J. A. Influence of polarization functions on molecular-orbital hydrogenation energies *Theor. Chim. Acta.*, **1973**, *28*, 213−222.

41. Petersson, G. A.; Al-Laham, M. A. A complete basis set model chemistry. II. Open-shell systems and the total energies of the first-row atoms *J. Chem. Phys.* **1991**, *94*, 6081−6090.

42. Tomasi, J.; Mennucci, B.; Cammi, R. Quantum Mechanical Continuum Solvation Models. *Chem. Rev.*, **2005** *105*, 2999−3093.

43. Cossi, M.; Barone, V.; Cammi, R.; Tomasi, J. Ab initio Study of Solvated Molecules: A New Implementation of the Polarizable Continuum Model. *Chem. Phys. Lett.*, **1996**, *255*, 327−335.

44. Cances, E.; Mennucci, B.; Tomasi, J. A New Integral Equation Formalism for the Polarizable Continuum Model: Theoretical Background and Applications to Isotropic and Anisotropic Dielectrics. *J. Chem. Phys.* **1997**, *107*, 3032−3041.

45. Barone, V.; Cossi, M. Quantum Calculation of Molecular Energies and Energy Gradients in Solution by a Conductor Solvent Model. *J. Phys. Chem. A* **1998,** *102*, 1995−2001.

46. Palascak, M. W.; Shields, G. C. Accurate Experimental Values for the Free Energies of Hydration oh H^+. OH^-, and H_3O^+. *J. Phys. Chem. A* **2005**, *108*, 3692−3694.

47. Frost, A. A.; Pearson, R. G. *Kinetics and Mechanism*; Wiley: New York, 1961.

48. Arrnold, D.; Plank, C.; Erickson, E.; Pike, F. Solubility of Benzene in Water. *Ind. Eng. Chem. Chem. Eng. Data Series.* **1958**, *3*, 253−256.

49. Holm, R. H.; Metal-Centered Oxygen Atom Transfer Reactions. *Chem. Rev*. **1987** *87*, 1401−1449.

50. Carter, E. A.; Goddard, W. A. III Early- versus Late-Transition–Metal–Oxo Bonds: The Electronic Structure of VO^+ and RuO^+. *J. Phys. Chem.* **1988**, *92*, 2109–2115.

51. Shiota, Y.; Yoshizawa, K. Methane-to Methanol Conversion by First-Row Transition–Metal Oxide Ions: ScO^+, TiO^+, VO^+, CrO^+, MnO^+, FeO^+, CoO^+, NiO^+, and CuO^+. *J. Am. Chem. Soc.* **2000**, *122*, 12317–12326.

52. Winlker, J. R.; Gray. H. B. Electronic Structures of Oxo—Metal Ions. Struc. Bond. Structure and Bonding. **2012**. *142*, 17–28.

53. Huda, M. N.; Yan, Y.; Moon, C.-Y.; Wei, S.-H.; Al-Jassim, M. M. Density-Functional Theory of the Effects of Atomic Impurity on the Band Edge of Monoclinic WO_3. *Phys. Rev. B* **2008**, *77*, 195102.

54. Yoshizawa K.; Shiota Y.; Yamabe, T. Reaction Pathway for the Direct Benzene Hydroxylation by Iron−Oxo Species. *J. Am. Chem. Soc.* **1999,** *121*, 147–153.

55. Shiota Y.; Suzuki, K.; Yoshizawa, K. Mechanism for the Direct Oxidation of Benzene to Phenol by FeO^+. *Organometallics* **2005,** *24*, 3532–3538.

56. Li, J.-L.; Zhang, X.; Huang, X.-R. Mechanism of Benzene Hydroxylation by High-Valent Bare $Fe^{IV}=O^{2+}$: Explicit Electronic Structure Analysis. *Phys. Chem. Chem. Phys.* **2012**, *14*, 246–256.

57. Clark, A. E.; Hurst, J. K. In *Mechanisms of Water Oxidation Catalyzed by Ruthenium Coordination Complexes, in Progress in Inorganic Chemistry*; Karlin, K. D., Ed.; John Wiley & Sons, Inc.: Hoboken, NJ, 2011; Vol. *57*.

58. Kärkäs, M. D.; Johnston, E. V.; Verho, O.; Åkermark, B. Artificial Photosynthesis: From Nanosecond Electron Transfer to Catalytic Water Oxidation. *Acc. Chem. Res.* **2014**, *47*, 100−111.

59. Acuña-Parés, F.; Codolà, Z.; Costas, M.; Luis, J. M.; Lloret-Fillol, J. Unraveling the Mechanism of Water Oxidation Catalyzed by Nonheme Iron Complexes. *Chem. Eur. J.* **2014**, *20*, 5696–5707.

60. Liao, R.-Z.; Siegbahn, E. M. Quantum Chemical Modeling of Homogeneous Water Oxidation Catalysis. *ChemSusChem* **2017**, *10*, 4236–4263.

61. Chen, Z.; Concepcion, J. J.; Hu, X.; Yang, W.; Hoertz, P. G.; Meyer, T. J. Concerted O Atom-Proton Transfer in the O–O bond forming Step in Water Oxidation. *Proc. Natl. Acad. Sci. U. S. A.* **2010**, *107*, 7225–7229.

62. Shimoyama, Y.; Tamura, S.; Kitagawa, Y.; Hong, D.; Kon, Y. A Cobalt-Substituted Keggin-Type Polyoxometalate for Catalysis of Oxidative Aromatic Cracking Reactions in Water. *Catal. Sci. Technol.* **2020**, *10*, 8042−8048.

Table 5-1. Effect of Changing Heteroatoms for Bond Length (Ru–O$_x$), Orbital Energy, and Free Energies for Benzene Hydroxylation and Water Oxidation Reactions.

X	[a]Ru–O$_x$	[b]LUMO in Ru^V=O	[c]G_a^B	[c]G_a^W	[d]G(**rc^B**)	[d]G(**rc^W**)	[e]G(**ts^B**)	[e]G(**ts^W**)
Al	2.18	–3.88	15.2	27.4	9.2	3.5	24.4	30.9
Ga	2.14	–3.89	14.8	27.3	5.4	–0.7	20.2	26.7
Si	2.28	–4.19	13.5	26.7	8.8	4.2	22.3	30.9
Ge	2.22	–4.21	13.0	26.4	8.2	3.7	21.2	30.1
P	2.34	–4.51	10.7	24.8	6.7	3.3	17.5	28.1
As	2.29	–4.50	10.7	25.2	6.6	3.3	17.3	28.5
S	2.46	–4.72	10.3	26.6	4.3	2.6	14.6	29.2

[a]Units in (Å). [b]Units in (eV). [c]G_a^B and G_a^W indicate the activation free energies for benzene hydroxylation and water oxidation reactions (kcal/mol). [d]G(**rc^B**) and G(**rc^W**) indicate the free energies for **rc^B** and **rc^W** (kcal/mol). [e]G(**ts^B**) and G(**ts^W**) indicate the free energies for **ts^B** and **ts^W** (kcal/mol).

Chapter 6

General conclusions

Oxidation of hydrocarbons having inert C–H bond such as methane and benzene is an important chemical and catalytic process in the modern industrial chemistry. In contrast to the industrial process of methane and benzene hydroxylation requiring high temperature and involving multi-step, metalloenzyme directly convert methane and benzene into methanol and phenol, respectively, by using O_2. However, it is difficult to apply these enzymes to large-scall chemical reactions because of their unstable, expensive of electron source for the formation of transition metal–oxo active site from O_2, and so on. On the other hand, some metalloenzymes produce transition metal–oxo active site that can catalyze the oxidation of substrate by using H_2O molecule as an oxygen source. To mimic of function of these enzymes help us to develop new catalysts performing the oxidation of substrates without sacrificial agent and harmful solvent at mild condition.

Herein the author proposes new catalysts performing the oxidation of substrates in the coexistence of H_2O molecules by using density functional theory (DFT) calculations, where H_2O is used not only for the oxygen source of the formation of transition metal–oxo active species but also the proton source. Herein Iridium (Chapter2-4) and Ruthenium (Chapter 5) complex is proposed.

In Chapter 2-4 a light-driven methane fuels cell has been proposed. This is the fuel cell that convert methane into methanol driven by the visible light irradiation for anode consists of an iridum-aqua complex $[Ir^{III}(\eta^5\text{-}C_5Me_5)\{bpy(COOH)_2\}(H_2O)]^{2+}$ (bpy($COOH_2$) = 2,2'-bipyridine-4,4'-dicarboxylic acid) over WO_3. This anode electrode was developed by Ogo and coworker for the light-driven fuels cell catalyzing water splitting via an iridium–oxo complex $[Ir^{V}(\eta^5\text{-}C_5Me_5)\{bpy(COOH)_2\}(O)]^{2+}$. In Chapter2 the catalytic cycle of H_2O oxidation has been clarified that the formation of the iridium–oxo complex reacting with H_2O to form O–O bond is an important step for the H_2O oxidation. The detail reaction mechanism of the formation of the iridium–oxo complex has been investigated by using a cluster model that

iridium complex is over a $(WO_3)_{40}$ cluster with the coordination of carboxylate group to W atom in Chapter 3. This investigation has been performed by using time-dependent DFT (TD-DFT) and DFT calculations. These calculations strongly have suggested that deprotonation reactions from aqua and hydroxyl ligand, leading to the activation of Ir 5*d* orbitals, play an essential role for visible-light irradiation. The iridium–oxo complex can react with not only H_2O to form O_2 but also CH_4 to form CH_3OH, proposed in Chapter 4. In the methane hydroxylation C–H bond activation is undergone to form radical intermediate involving methyl radical ($^{\bullet}CH_3$) in the triplet ground state, and subsequent C–O radical coupling reaction leads to the formation of CH_3OH with the spin inversion in the radical intermediate. Although the activation energy of C–H bond activation in the closed-shell singlet is higher than other spin states, it has a potential that $^{\bullet}CH_3$ is not produced along the reaction. By performing intrinsic bond orbital (IBO) analysis, it has been revealed that electrophilicity of Ir^{V}=O species induces the H atom abstraction in CH_4 to CH_3OH, where H atom migrate from CH_4 to Ir^{V}=O species as a hydride (H^-). To summarize, the author has proposed the methane hydroxylation by the iridium–oxo complex immobilized over WO_3 surface in anode electrode, where the iridium–oxo complex is generated by the visible-light irradiation for the iridium–aqua complex.

The author has also proposed a catalyst performing benzene hydroxylation in aqueous solution in Chapter 5. Ru-substituted Keggin-type polyoxometalate $[Ru^{V}(O)XW_{11}O_{39}]^{n-}$ ($3 \leq n \leq 6$) (*X* = Al, Ga, Si, Ge, P, As, and S; heteroatoms) is used for a model catalyst. The benzene hydroxylation by $[Ru^{V}(O)XW_{11}O_{39}]^{n-}$ proceeds through the aromatic electrophilic substituted reaction. The activation free energy of this reaction is decreased as the shorten of bond length in μO_x–*X*. This is because the shorten bond length in μO_x–*X* stabilizes the LUMO in Ru^{V}=O, leading to the increasing the orbital interaction between LUMO in Ru^{V}=O and HOMO in benzene moiety. On the contrary, the heteroatom effect for the reacting Ru^{V}=O with H_2O has not been observed. The reaction rate ratio between benzene hydroxylation and water oxidation reaction is calculated by using the Arrhenius-like equation. A good liner correlation between the reaction rate ratio and bond distance in μO_x–*X* has been observed. The calculated values lead to the conclusion that $[Ru^{V}(O)SW_{11}O_{39}]^{3-}$ is a candidate high-performance benzene hydroxylation catalyst even low concentration of benzene in aqueous solution.

In this thesis the development of methane and benzene hydroxylation catalysts by performing DFT and TD-DFT calculations has been presented. Both catalysts are performed in the coexistence of H_2O, where H_2O act as not only oxygen source for transition metal–oxo active species but also solvation of proton. The chemical thinking and consideration done in

this thesis should provide important chemical information to help design of new catalyst performing without sacrifice agents and harmful solvent. The author provides an excellent milestone for chemistry of catalyst from the viewpoint of theoretical chemistry. Also, the author contributes to further understanding or the catalytic fashion of hydrocarbon hydroxylation in the coexistence of water. The author, Kei Ikeda, definitely believe my important, wonderful, great, and excellent research significantly useful for future design guidelines for hydrocarbon hydroxylation in the coexistence of water even if some experimentalists and theoreticians are bored reading this thesis.

Acknowledgement

This thesis is a summary of the author's studies from 2017 to 2019 as a membered of Ogo laboratory and 2019 to 2021 as a membered of Yoshizawa laboratory at the Department of Chemistry and Biochemistry, Kyushu University.

The writing of this dissertation would not have been possible without the help and encouragement of many teachers, colleagues, and friends. It is my great pleasure to thank these people.

At first, the author is indeed happy to express his cordial gratitude to Professor Kazunari Yoshizawa, Associate Professor Yoshihito Shiota for leading me to theoretical chemistry. He also would like to express his sincere appreciation to Associate Professor Aleksandar Staykov and Assistant Professor Yuta Tsuji for their helpful advice and suggestions. Special acknowledgments should be made to Assistant Professor Muhammad Haris Mahyuddin at Institut Teknologi Bandung for his kind advice, discussions, and helpful support.

It is a great pleasure to express his gratitude to Professor Seiji Ogo at Kyushu University for welcoming his to his lab for the supporting his during Master course at the Department of Chemistry and Biochemistry, Kyushu University. He also would like to thank Associate Professor Takahiro Matsumoto for his enthusiastic guidance. He is deeply grateful to Ki-Seok Yoon for cordial gratitude.

The author should be happy to express his cordial gratitude to Associate Professor Shugo Suzuki at University of Tsukuba for his helpful teaching me to theoretical fields during Bachelor course at the College of Engineering Science, University of Tsukuba.

The author would like to acknowledge Program for Department of Chemistry and Biochemistry, Kyushu University. He is thankful to Dr. Yuta Hori for his great help. He also thanks Dr. Tsukasa Abe, Dr. Masataka Yoshida, Dr. Yosuke Sumiya, Dr. Takuo Minato, Ms. Yoko Nishi, Mrs. Mayuko Miyanishi, and Mrs. Asuka Konomi for their support. And he should be thankful to Dr. Yu Nakano for her support.

The author expresses my appreciation to all other members of the Yoshizawa laboratory and the Shugo-Suzuki laboratory for their direct and indirect support. I thank all my friends for their encouragement and understanding.

I would like to dedicate this thesis to Kanae Haruta, will be my wife Kanae Ikeda, with my gratitude to her mother, Haruko Haruta, and her father, Toichi Haruta, and fall their help and encouragement. In the end, I would like to dedicate this thesis to my mother, Hiromi Ikeda

and my father, Masaaki Ikeda, with my gratitude to my old sister, Kana Ikeda and younger sister, Rei Ikeda and fall their help and encouragement.

Fukuoka, December 2021

Kei Ikeda

List of Publications

Chapter 2

"Dual Catalytic Cycle of H_2 and H_2O Oxidations by a Half-Sandwich Iridium Complex: A Theoretical Study."

Kei Ikeda, Yuta Hori, Muhammad Haris Mahyuddin, Yoshihito Shiota, Aleksandar Staykov, Takahiro Matsumoto, Kazunari Yoshizawa, and Seiji Ogo.

Inorganic Chemistry, **58**, 7274–7284, (2019).

Chapter 3

"Computational Study on the Light-Induced Oxidation of Iridium–Aqua Complex to Iridium–Oxo Complex over WO_3(001) Surface."

Kei Ikeda, Muhammad Haris Mahyuddin, Yoshihito Shiota, Aleksandar Staykov, Takahiro Matsumoto, Seiji Ogo, and Kazunari Yoshizawa.

Inorganic Chemistry, **59**, 415–422, (2020).

Chapter 4

"Active Catalyst for Methane Hydroxylation by an Iridium–Oxo Complex."

Kei Ikeda, Muhammad Haris Mahyuddin, Yoshihito Shiota, and Kazunari Yoshizawa.

ACS Catalysis, **10**, 8254–8262, (2020).

Chapter 5

"Theoretical Investigation into Selective Benzene Hydroxylation by Ru-Substituted Keggin-Type Polyoxometalates."

Kei Ikeda, Kazunari Yoshizawa, and Yoshihito Shiota.

In press. DOI: 10.1021/acs.inorgchem.1c02605

The following papers are not included in this thesis

"Real-space observation of far-and near-field-induced photolysis of molecular oxygen on an Ag (110) surface by visible light."
Chenfang Lin, **Kei Ikeda**, Yoshihito Shiota, Kazunari Yoshizawa, and Takashi Kumagai.
The Journal of Chemical Physics, **151**, 144705, (2019).

"Molecular functionalization of all-inorganic perovskite $CsPbBr_3$ thin films."
Arramel, Pan Hu, Aozhen Xie, Xinmao Yin, Chi Sin Tang, **Kei Ikeda**, Muhammad Haris Mahyuddin, Muhammad Fauzi Sahdan, Dingguan Wang, Kazunari Yoshizawa, Hong Wang, Muhammad Danang Birowosuto, Cuong Dang, Andrivo Rusydi, Andrew Thye Shen Wee, and Jishan Wu.
Journal of Materials Chemistry C, **8**, 12587–12598, (2020).

"Mechanistic Insight into Concerted Proton−Electron Transfer of a Ru(IV)-Oxo Complex: A Possible Oxidative Asynchronicity."
Hiroki Kotani, Hinatsu Shimomura **Kei Ikeda**, Tomoya Ishizuka, Yoshihito Shiota, Kazunari Yoshizawa, and Takahiko Kojima.
Journal of the American Chemical Society, **2020**, 16982–16989, (2020).

"計算化学を用いた新規メタン水酸化触媒の提案."
池田 京, 塩田 淑仁, 吉澤 一成.
Journal of Computer Chemistry, Japan, **19**, 133–135, (2020).